Charmonium Production in $p\bar{p}$ Collisions at $\sqrt{s} = 1.8$ TeV

by

Troy Daniels

B.A. Mathematics and Physics
Lehigh University

Submitted to the Department of Physics
in partial fulfillment of the requirements for the degree of

Doctor of Philosophy

at the

MASSACHUSETTS INSTITUTE OF TECHNOLOGY

June 1997

© Troy Daniels, MCMXCVII. All rights reserved.

The author hereby grants to MIT permission to reproduce and distribute publicly paper and electronic copies of this thesis document in whole or in part, and to grant others the right to do so.

Author . . . . . .
Department of Physics
April 4, 1997

Certified by . . . . . .
Paris Sphicas
Professor
Thesis Supervisor

Accepted by . . . . . .
Prof. George Koster
Chairman of the Physics Department Committee on Graduate Students

Charmonium Production in $p\bar{p}$ Collisions at $\sqrt{s} = 1.8$ TeV

by

Troy Daniels

Submitted to the Department of Physics
on April 4, 1997, in partial fulfillment of the
requirements for the degree of
Doctor of Philosophy

Abstract

Charmonium production in $p\bar{p}$ collisions is studied using data taken at a center of mass energy of 1.8 TeV with the CDF detector. The differential cross sections for the production of J/ψ and ψ' mesons are measured.

Charmonium production is expected to proceed via two mechanisms. One method of production is the decay of B mesons and baryons. The other is direct production, via parton-parton fusion and gluon and charm fragmentation. The two production mechanisms are separated and compared with theoretical predictions.

Thesis Supervisor: Paris Sphicas
Title: Professor

Acknowledgments

Above all, I would like to thank my advisor, Paris Sphicas, for the direction he has provided me throughout my graduate career. His support was essential for my completion of this work. I would also like to thank John Cunningham and Vaia Papadimitriou for their assistance in various parts of the analysis.

Slawomir Tkaczyk, Jonathan Lewis and Tom LeCompte deserve thanks for their interest in my analysis. Tom was especially helpful and understanding as I learned about the CDF muon system. I would also like the thank the MIT group, especially Ken, Petar, Wasiq and Tushar. We had many interesting discussions, and, when the stress of life at Fermilab became too much, they were around to help all of us relax. Carol, Steve and Eddie were each helpful and entertaining in their own ways.

The support team at Fermilab were also excellent. Carol Picciolo was always willing to help me with whatever problems I had. Special thanks to Peggy Berkovitz at MIT for doing so much for me, especially those tasks which required someone to be in Massachusetts.

The professors at Lehigh and MIT were all helpful in getting to this point. Jerry King was especially inspiring. The members of the extra-curricular groups provided useful stress relief, whenever college became too tense. Everyone in Marching Band was great.

Thanks to Izzy, Elke, Mary, Jodeen, Christian, Honor, Andrew, David, Baber, Mary, Amy and David, Jamie and Gwyneth for being friends. Audra and Paula were always available and fun to be around. Sue, Stephane and Miriam – I'll always remember those late–night study sessions. Highest thanks to my family – Mom, Dad, Helen, Earl and Katie – I couldn't have done it without you.

This thesis is dedicated to my grandparents, Helen and Earl.

Contents

1 Introduction **13**

1.1 History 14

1.2 Symmetries 18

1.3 Running Coupling Constants 20

1.4 Structure Functions 23

1.5 Fragmentation 23

1.5.1 Petersen Fragmentation 24

1.6 Charmonium Masses And Decay Modes 27

1.7 Charmonium Production 29

1.7.1 Direct Production 29

1.7.2 Fragmentation Production 31

1.7.3 Color Octet Production 32

1.7.4 B Production 33

1.7.5 Production Summary 35

2 Experimental Apparatus **36**

2.1 Coordinate System 36

2.2 The Accelerator 37

2.3 CDF 41

2.3.1 Solenoid 41

2.3.2 Central Tracking Chamber 41

2.3.3 Silicon Micro-vertex Detector 45

2.3.4 Vertex Time Projection Chambers 50
2.3.5 Calorimeters 51
2.3.6 Muon Chambers 53
2.3.7 Beam Beam Counters 56
2.3.8 Trigger System 56
2.3.9 Data Acquisition 59

3 Inclusive ψ Cross Section 64

3.1 Event Selection 64
3.1.1 Basic Requirements 64
3.1.2 Background Contributions 66
3.1.3 Background Suppression 68
3.2 Mass Fit 72
3.2.1 Resolution determination 76
3.2.2 Quality of Mass Fits 79
3.2.3 Trigger Efficiency 86
3.3 Acceptance 88
3.4 Efficiencies 90
3.5 Cross Section 93

4 Production Fractions 97

4.1 B Fraction 98
4.1.1 Decay Length Measurement 98
4.1.2 L_{xy} Distribution 102
4.1.3 Fitting the Lifetime Distribution 110
4.1.4 Quality of the B fraction fits 113
4.2 $\chi_c \to J/\psi\gamma$ Fraction 120

5 Comparison with Theoretical Predictions 125

5.1 Monte Carlo Simulation 126

5.1.1 Event Generation 126
5.1.2 Particle Decay Simulation 129
5.1.3 Detector Simulation 132
5.2 B Production 133
5.3 Direct Production 137
5.3.1 Color Singlet Model 137
5.3.2 Color Octet Model 139
5.4 Cross Section Ratios 147

6 Conclusions And Outlook **152**
6.1 Summary of Results 152
6.2 Future Prospects 154

A Statistical Methods **157**
A.1 Fitting Methods 157
A.2 Toy Monte Carlos 160

List of Figures

1-1 Diagrams associated flavor changing neutral currents. 16

1-2 Annihilation of $c\overline{c}$ into gluons. 19

1-3 An electron propagating through the vacuum 20

1-4 Feynman diagrams for proton–anti-proton collisions. 21

1-5 Tube of color flux connecting two quarks 22

1-6 Feynman diagram of b quark fragmentation. 25

1-7 The Petersen fragmentation function. 26

1-8 Charmonium mass spectrum 27

1-9 Leading order diagram for J/ψ and $\psi(2S)$ production and χ_c production 29

1-10 Leading order Feynman diagram for the decay $\psi \rightarrow \ell^+\ell^-$ 29

1-11 Gluon and charm fragmentation production of ψ in the color singlet model. 31

1-12 Gluon fragmentation production of ψ in the color octet model. 33

1-13 Feynman diagrams for b production from gluon fusion (left), gluon splitting(center) and flavor excitation (right). 33

1-14 Typical B meson decay diagram for charmonium production. 34

2-1 Elements in the generation and acceleration of protons and anti-protons at Fermilab. 38

2-2 Schematic diagram of the particle accelerators at Fermilab. 40

2-3 Cut-away view of one half of CDF. The detector is forward-backward symmetric. 42

2-4 End-view of the CTC. 44
2-5 One ladder of the SVX detector. The three crystals, the readout electronics and the mounting equipment are shown. 46
2-6 Cut-away isometric view of one SVX barrel. 47
2-7 Beam profiles as measured by the SVX 49
2-8 One tower of the CMU 53
2-9 Schematic of the path traversed by a muon through the CDF detector. 55
2-10 Schematic diagram of flow in the CDF data acquisition and trigger systems in the 1992-1993 run. 60
2-11 Data acquisition system in the 1993-1995 run. 62

3-1 Efficiencies of the Level 1 and Level 2 muon triggers, as a function of muon P_T. 65
3-2 Mass distribution of the J/ψ(a) and $\psi(2S)$(b) candidates, after all requirements have been applied. 70
3-3 Width of the J/ψ mass peak as a function of ψ P_T. 72
3-4 Mass and pull distribution of the J/ψ sample, overlaid with fit to Gaussian plus background 73
3-5 Mass template creation 75
3-6 The definition of curvature 76
3-7 Generated dimuon mass distributions and mass templates after being smeared by the fast detector simulator. 78
3-8 J/ψ mass distributions at low P_T, with radiative fit results overlaid. . 80
3-9 J/ψ mass distributions at high P_T, with radiative fit results overlaid. 81
3-10 $\psi(2S)$ mass distributions, with radiative fit results overlaid. 82
3-11 Results of fitting the J/ψ mass distribution to a Gaussian plus linear background and using the radiative fit. 83
3-12 Confidence level of the mass fits, based on the χ^2 distribution. 84
3-13 Distribution of $\sum$R values for Monte Carlo (histogram) and data (arrow) in the first two P_T regions. 85

3-14 Average trigger efficiency for the $J/\psi$and the $\psi(2S)$. 86
3-15 Detector acceptance for the J/ψ (left) and $\psi(2S)$ (right) as a function of P_T. 89
3-16 $J/\psi$and $\psi(2S)$differential cross sections. 93

4-1 Possible decay configurations 99
4-2 The variables used to define L_{xy}. 101
4-3 The Monte Carlo correction factor $F_{\rm corr}$ for the J/ψ and the $\psi(2S)$. . 103
4-4 J/ψ $c\tau$ distributions, with fit results overlaid. 106
4-5 J/ψ $c\tau$ distributions, with fit results overlaid at high P_T. 107
4-6 $\psi(2S)$ $c\tau$ distributions, with fit results overlaid. 108
4-7 $\psi(2S)$ $c\tau$ distributions at high P_T, with fit results overlaid. 109
4-8 The J/ψ(left) and $\psi(2S)$(right) B fraction as a function of $P_T(\psi)$ from fitting the data. The vertical error bars indicate the statistical uncertainty; the horizontal error bars denote the bin width. 111
4-9 χ^2 per degree of freedom for the J/ψ (left) and the $\psi(2S)$ (right) B fraction fits. 114
4-10 Mean of the pull distribution of the J/ψ and the $\psi(2S)$ B fraction fits. 114
4-11 RMS of the pull distribution of the J/ψ (left) and the $\psi(2S)$ (right) B fraction fits. 115
4-12 Confidence level of the J/ψ and $\psi(2S)$ B fraction fits from the toy Monte Carlo. 116
4-13 Variation in the J/ψ B fraction as a function of P_T for the different fitting methods. 118
4-14 Average value of $\sum P_T$ for J/ψ candidates in the SVX, and in B-enriched and B-depleted samples. 119
4-15 Average value of $\sum P_T$ for J/ψ candidates with both muons in the SVX, and for the entire sample. 120
4-16 Mass difference $m(\mu^+\mu^-\gamma) - m(\mu^+\mu^-)$ for χ_c candidates. 121
4-17 $F^{J/\psi}_{\chi_c,\text{no B}}$ as a function of P_T 123

5-1 Transverse momentum versus rapidity of the b quark for BGENERATOR events with successful fragmentation. 128
5-2 The (a) J/ψ and (b) $\psi(2S)$ momentum distributions in the CLEO lab frame. 129
5-3 J/ψ differential cross sections from B production. 133
5-4 $\psi(2S)$ differential cross sections from B production. 135
5-5 Direct J/ψ and $\psi(2S)$ cross sections, compared with the Color Singlet Model. 138
5-6 J/ψ color octet fit results, for separate fits 140
5-7 $\psi(2S)$ color octet fit results, for separate fits 141
5-8 J/ψ color octet fit results, for combined fit 145
5-9 $\psi(2S)$ color octet fit results, for combined fit 146
5-10 Ratio of J/ψ and $\psi(2S)$ cross sections for production from B decays. 149
5-11 Ratio of cross sections from B production, divided by theory. 150

A-1 Difference between χ^2 and log-likelihood fits. 159

List of Tables

1.1 G-parity of particles associated with charmonium production. 20

2.1 Tevatron Collider parameters for the 1992-1993 run. 40

2.2 CTC mechanical characteristics and nominal resolutions 45

2.3 SVX layer characteristics 48

3.1 Event selection criteria 68

3.2 Variations in the J/ψ trigger efficiency correction from different techniques for performing the correction. 87

3.3 Variations in the $\psi(2S)$ from different techniques for performing the trigger correction. 87

3.4 Summary of requirements and efficiencies for J/ψ and $\psi(2S)$ reconstruction. 92

3.5 The differential J/ψ cross section. 94

3.6 The differential $\psi(2S)$ cross sections. 94

3.7 Fractional systematic uncertainties in the cross section measurements. 95

4.1 The B fraction in the J/ψ sample. 112

4.2 The B fraction in the $\psi(2S)$ sample. 113

4.3 Change in B fraction as the fitting technique is changed. 116

4.4 Systematic uncertainties in the B fraction measurements. All uncertainties are independent of P_T. 117

5.1 The differential J/ψ cross section from B production. 134

5.2 The differential $\psi(2S)$ cross sections from B production. 134
5.3 Fitted color octet matrix elements, using separate fits. 143
5.4 The differential J/ψ cross section from prompt production. 143
5.5 The differential J/ψ cross section from direct production. 144
5.6 The differential $\psi(2S)$ cross sections from prompt production. 144
5.7 Fitted color octet matrix elements, fitting both distributions simultaneously. 147
5.8 Theoretical systematic uncertainties in the B cross section ratio measurements. All uncertainties are independent of P_T. 148

6.1 Fitted color octet matrix elements, using separate fits. 153
6.2 Fitted color octet matrix elements, fitting both distributions simultaneously. 154

Chapter 1

Introduction

Taking something apart is an excellent way to learn how it works. Of course, sometimes this merely reveals seemingly incomprehensible internal components, so it may be necessary to further take apart some of these pieces. If we still don't understand what is inside, we can continue to look at smaller and smaller parts, until we encounter components that are simple enough to be understood. In one sense, particle physics is nothing more than this process, taken to the ultimate extreme. We "take apart" matter and look at what is inside it, but at a scale of about 10^{-16} cm.

While this sounds like an extremely small distance, there is actually a large number of probes which can be used. One powerful probe is charmonium, the bound state of a charm (c) quark and an anti-charm($\overline{c}$) quark, which is the method employed in this thesis. Interpretation of charmonium data and other experimental studies has led to the development of the "Standard Model," the leading theory of particle interactions. Many of the predictions of the Standard Model have been verified, in some cases with extremely high accuracy. Indeed, some physicists complain that the Standard Model works too well. Great advances in science often occur when the current theoretical model is unable to explain a new experimental result. The Standard Model has provided few such opportunities, despite numerous experimental tests.

In this thesis, the first chapter provides a summary of the Standard Model, with an emphasis on the production of charmonium. Chapter 2 describes the experimental

apparatus used for the analysis. The measurement of the cross section is described in Chapter 3, while Chapter 4 explains how the cross section is broken down into its various components. The resulting measurements are compared to the theoretical predictions in Chapter 5, and the results are summarized in Chapter 6.

1.1 History

The first component of the Standard Model was developed by P.A.M. Dirac, when he presented his relativistic quantum theory of electromagnetism, Quantum Electrodynamics (QED).[1, 2] QED forces are mediated by a single massless particle, the photon(γ). The strength of the electromagnetic force on a particle is proportional to the particle's "electric charge." While exact calculations are generally not possible, a perturbation series in the QED coupling constant, $\alpha \equiv e^2/4\pi\hbar c \approx 1/137$, converges rapidly. When calculating a matrix element with perturbation theory, each photon which is emitted or absorbed contributes one power of α to the square of the matrix element, so processes requiring a larger number of photons are suppressed relative to those with fewer photons. QED has been extended by Glashow, Weinberg and Salam[3, 4, 5] to include the weak force, which is responsible for nuclear beta decays. The weak force is mediated by three particles, the W^+, W^- and the Z^0. One difference between electromagnetism and the weak force is that all three particles are massive, which has the effect of limiting the range of the force when the energy transfer is smaller than the $W^\pm$ or Z^0 mass. However, if the energy transfer is larger than the mass, the weak force behaves similarly to the electromagnetic force. The two forces are said to "unify" into a single force, the electroweak force, with a single coupling constant related to α.

The final force in the Standard Model which is incorporated at the quantum level is the strong force, which binds quarks into "hadrons:" "baryons" and "mesons." A baryon consists of three quarks, while a meson is the bound state of a quark and an anti-quark. The strong force is mediated by eight gluons, whose coupling is

proportional to the "color charge." This color is unrelated to the color that people see, although there are similarities in behavior. The properties of gluons are described by Quantum Chromodynamics (QCD). QCD and the electroweak force are not unified within the context of the Standard Model, so there is a second coupling constant, α_S, describing the strength of the QCD force, which is unrelated to α. As α_S is substantially larger than α, the QCD force is often called the "strong force," and α_S the "strong coupling constant."

One early objection to electroweak theory was the experimental absence of "flavor–changing neutral currents." The electroweak quark eigenstates are linear combinations of the QCD quark eigenstates, so the amplitude for a process such as $\nu_\ell d \rightarrow \nu_\ell d$ is actually the weighted sum of the amplitudes for the processes $\nu_\ell d' \rightarrow \nu_\ell d'$ and $\nu_\ell s' \rightarrow \nu_\ell s'$ shown in Figure 1-1, where

$$d' = d\cos\theta_C + s\sin\theta_C \tag{1.1}$$

$$s' = s\cos\theta_C - d\sin\theta_C \tag{1.2}$$

At the time electroweak theory was first proposed, there were only three known quarks, u, d and s. The u and d quarks formed a doublet, but the s quark could only be put into a singlet. However, the Z^0 couples with different strengths to singlets and doublets, so the $d \rightarrow s$ components do not cancel completely. Thus, the theory predicts interactions where no charge is exchanged, but the quark flavor is changed, with a cross section similar to that of $\nu_\ell d \rightarrow \nu_\ell d$. Experimentally, these reactions are nearly absent,[6] which presented a serious problem for the theory.

Glashow, Iliopoulos and Maiani[7] noted that this can be resolved by adding a fourth quark. The s quark and the fourth quark now form a doublet, and the couplings in the two diagrams are the same. The $d \rightarrow s$ transitions cancel, and the flavor–changing neutral currents are no longer allowed.[1] Thus, the fourth quark is the

[1]The cancelation is complete only when the up and charm quarks have the same mass. If the masses are different, the process is allowed, but greatly suppressed.

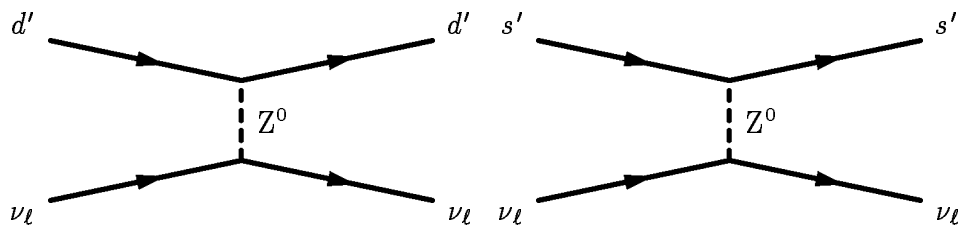

Figure 1-1: Diagrams associated flavor changing neutral currents. Since the d' and s' are both mixtures of d and s quarks, both diagrams include d and s quarks in the initial and final states.

"charm" that eliminates the unwanted prediction, yielding the quark's name. However, there was no experimental evidence for the charm quark. From a theoretical perspective, it seemed to be an *ad hoc* addition, whose usefulness was limited to one specific problem in a model which, at that time, was not generally accepted. As a result, this possibility received little attention.

This changed with the "November Revolution" in 1974. Experiments using an e^+e^- collider at SLAC [8] and a proton beam on a beryllium target at Brookhaven[9] found evidence of a narrow resonance with a mass of about 3.1 GeV/c^2 . The particle was named the ψ by the SLAC group, and the J by the Brookhaven group. Noting the simultaneous discovery, the particle is now called the J/ψ. It was clear from the beginning that a new type of quark was involved, for if the resonance was an excited state formed from a combination of up, down and strange quarks, it should decay strongly, with a much larger width. By scanning the cross section near the J/ψ mass, the SLAC group was able to observe J/ψ-γ interference. This, combined with the fact that it is produced directly in e^+e^- collisions, leads to the conclusion that the J/ψ has the same quantum numbers as the photon. A few months later, the Brookhaven group reported a second resonance at 3.7 GeV/c^2 [10]. This was later determined to be a radial excitation, now called the ψ' or $\psi(2S)$. These states and other $c\overline{c}$ bound states are referred to using the generic name charmonium.

Charmonium production is an excellent probe of QCD at the lowest possible transverse momentum in a high energy collider. Whereas jet analyses at CDF are typically

limited to $P_T > 15$ GeV/c, the decay of the ψ[2] to two muons provides a clean, easily triggered signal which allows us to look as low as 5 GeV/c. We will see later that charmonium also provides insights into fragmentation processes.

Similarly, ψ production from B decays combined with the large B cross section provides a valuable sample to study B production and other aspects of B physics. Again, the $B \rightarrow \psi X \rightarrow \mu^+\mu^- X$ decay chain allows us to study B production in momentum regions not experimentally accessible by other techniques. Furthermore, next–to–leading order predictions for B production exist, allowing QCD to be tested beyond leading order.

Understanding charmonium production in hadron–hadron collisions is also important for the search for a "quark–gluon plasma." It is expected that, at large enough densities, a phase transition occurs in quark matter.[11] Color confinement[3] will fail, and quarks and gluons will exist as free particles within the plasma, a condition which has not existed since the earliest moments of the universe. Experimental attempts at creating this plasma consist of colliding nuclei with a large number of nucleons at high energy. One signature of such a transition is the suppression of charmonium production.[12] $c\bar{c}$ pairs formed deep within the plasma need to penetrate the plasma, without being knocked apart by the constituent quarks and gluons, decreasing the probability of charmonium formation. If charmonium production in the relatively clean environment of a proton–anti-proton collider is not understood, this method of searching for or confirming the discovery of a quark–gluon plasma becomes much more difficult. Instead of comparing the observed rate with the predictions of an established model, the expected rate must be extrapolated from other experimental measurements. This extrapolation will depend in part on the same theory which is unable to predict charmonium production in the first place.

[2] In this thesis, ψ denotes either the J/ψ or the $\psi(2S)$.

[3] Color confinement is the observation that quarks (and other colored particles) do not exist as free particles, but only in bound states with no net color. See Section 1.3 for a further discussion.

1.2 Symmetries

Knowledge of the symmetries in a system can greatly simplify the study of that system, either by removing extraneous variables, or by eliminating from consideration processes which are forbidden by the symmetry. Symmetries are ubiquitous in quantum mechanics. One of the first symmetries found in quantum mechanics is that the phase of the wave function is arbitrary. Similarly, in classical electrodynamics, the potentials are not fully determined by Maxwell's equations, so one can make gauge transformations without affecting any observable quantities. This symmetry carries over into QED. There are other symmetries in particle physics, some of which do not have macroscopic analogues. Two important symmetries are parity and charge conjugation. Parity inverts the coordinate system, so that $\vec{r} \Rightarrow -\vec{r}$. Physical particles are eigenstates of parity, so that

$$\hat{P}|\xi\rangle = P|\xi\rangle \tag{1.3}$$

where P is the parity of the state. Since $\hat{P}^2 = 1$, this requires that $P^2 = 1$, or $P = \pm 1$. Particles with $P = +1(-1)$ are said to have even (odd) parity. Charge conjugation is the act of replacing every particle with its anti-particle. Particles that are their own anti-particles are eigenstates of charge conjugation, with

$$\hat{C}|\xi\rangle = \pm|\xi\rangle \tag{1.4}$$

The electromagnetic and strong forces are invariant under both parity and charge conjugation operations, while the weak interaction is invariant under neither operation.

Since charge conjugation changes the sign of a particle's electric charge, *e.g.*, $\hat{C}|\pi^+\rangle \propto |\pi^-\rangle$, only neutral particles can be eigenstates of charge conjugation. This symmetry can be extended to charged particles by including isospin symmetry. Isospin symmetry reflects that the strong interaction treats d and u quarks identically,

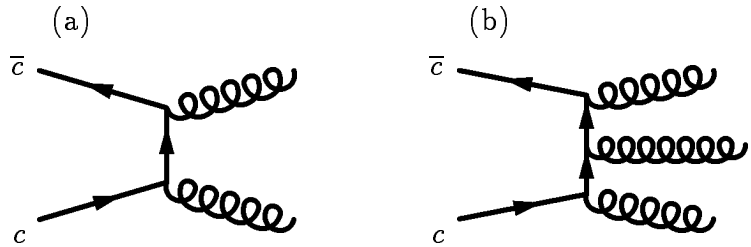

Figure 1-2: Annihilation of $c\overline{c}$ into gluons. States with $G = 1$ can only produce an even number of gluons, as in (a), while states with $G = -1$ yield an odd number of gluons, as in (b).

neglecting small effects due to the different masses of the two quarks. Combining charge conjugation with a reflection in isospin space (which replaces all $d(u)$ quarks with $u(d)$ quarks) produces a new symmetry, called G-parity. Charged particles made of u and d quarks are eigenstates of G-parity:

$$\hat{G}|\pi^+\rangle = -|\pi^+\rangle \tag{1.5}$$

Mesons with heavier quarks are also eigenstates of G-parity if the quark and anti-quark are the same flavor, that is, if they consist of $s\overline{s}$, $c\overline{c}$, $b\overline{b}$ or $t\overline{t}$. In this case, the G-parity eigenvalue is the same as the charge conjugation eigenvalue. G-parity is a symmetry of only the strong interaction. Table 1.1 lists the G-parity of several particles relevant to this thesis.

Symmetries lead to conservation laws in interactions possessing the symmetry. For instance, if the initial state of a process has odd G-parity, the final state will also have odd G-parity if it is reached by a strong interaction. A $c\overline{c}$ meson with $G = +1$ can decay into two gluons (each with $G = -1$) since the final state has $G = (-1)^2 = +1$, as in Figure 1-2a. Figure 1-2b is forbidden for a such a meson. Likewise, the J/ψ, when it decays into gluons, can only decay into an odd number of gluons, so only Figure 1-2b is allowed. Similar statements can be made about the production mechanisms: when producing a $c\overline{c}$ pair which forms a meson, the diagram must contain an even number of gluons coupling to the charm quark loop if the meson

Particle	G-parity
$\pi^{\pm}$,π^0	-1
gluon	-1
J/ψ,$\psi(2S)$	-1
χ_c	$+1$

Table 1.1: G-parity of particles associated with charmonium production.

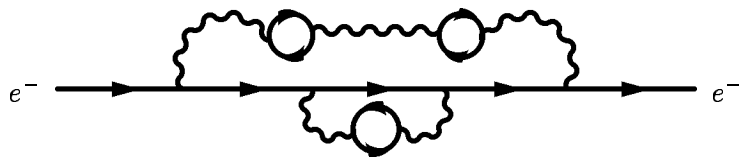

Figure 1-3: An electron propagating through the vacuum

has $G = +1$, or an odd number of gluons when the meson has $G = -1$. This will have important effects on the relative rates of production for different charmonium states.

1.3 Running Coupling Constants

While symmetries can be used to simplify calculations and analyses, one prediction of both electroweak theory and QCD complicates calculations: the strength of the interaction, given by α or α_S, is not constant, but varies with the energy of the interaction. The reason is as follows. As a particle travels through spacetime, it can emit and reabsorb particles, as in Figure 1-3, so that a "bare" particle is surrounded by a cloud of virtual particles. In QED, this cloud of virtual particles surrounding the bare particle shields the charge of the bare particle. A low energy probe will only see a fraction of the actual charge, while a higher energy probe will penetrate further into the cloud, and see a larger charge. Thus, the strength of the interaction depends on the energy of the interaction, with $\alpha(m_e) \approx \frac{1}{137}$ and $\alpha(m_{Z^0}) \approx \frac{1}{128}$. The phrase "running coupling constant" is used to describe this, because the value runs with

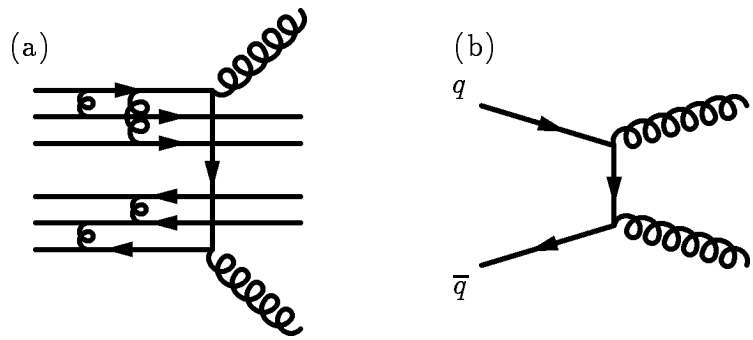

Figure 1-4: Feynman diagrams for proton–anti-proton collisions. (a) includes all the quarks, while (b) is the simplified version normally used in theoretical calculations.

the energy. As $\alpha \ll 1$ at all energies, perturbation theory in powers of α is a very powerful tool in QED and electroweak theory at all energies, providing extremely accurate predictions, even at low order.

In QED, the photons in the cloud surrounding a particle are electrically neutral, and the virtual fermion–anti-fermion pairs align themselves so as to shield the bare charge. However, the gluons of QCD carry color and enhance the charge, while the virtual quarks decrease the charge. The net effect is to enhance the charge of the bare particle. At high energies, particles penetrate deeply into the cloud, ignoring most of the charge, and the QCD coupling constant, α_S, approaches zero. This is called "asymptotic freedom," and greatly simplifies the calculation of high energy processes. In high–energy hadron collisions, typically only one parton from each hadron is scattered at large angles by the "hard scattering" process, as is shown in Figure 1-4a. The remaining partons form hadrons moving nearly parallel to the initial direction, becoming part of the "underlying event." Because of asymptotic freedom, when considering a high energy proton–anti-proton collision, the two partons involved in the hard scattering can be treated as free particles, and the effects of the remaining partons can be ignored. While a proton–anti-proton collision involves three quarks, three anti-quarks, and all the associated virtual particles, the much simpler Feynman diagram in Figure 1-4b is the type of process typically studied by theorists.

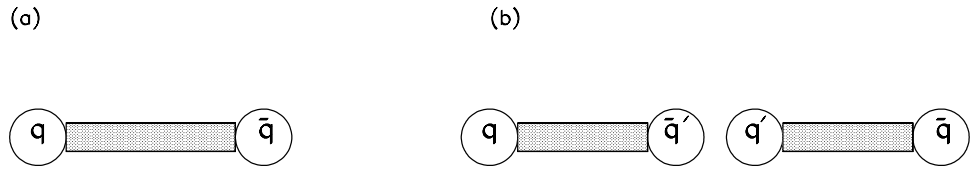

Figure 1-5: When trying to separate two quarks, the quarks act as if they are held together by a tube of color flux (a). If the tube is stretched too far (b), it breaks and forms a new quark–anti-quark pair.

Moving toward the opposite end of the energy spectrum, as the energy decreases, the cloud becomes increasingly important, and α_S increases, until $\alpha_S(1 \text{ GeV}) \sim 1$! Perturbation theory, which is so successful in QED, can no longer be used, as the importance of higher order terms is not decreased by a small coupling constant. At even lower energies, $\alpha_S > 1$, and higher order terms become *more* important than the leading order terms.

One result of the increase of α_S at low energies is that the strong force does not vanish at large distances. In the case of two electrically charged particles, α approaches a small constant as they are separated by an large distance, requiring only a finite amount of energy to separate the particles by an arbitrarily large distance. As the separation increases, ever smaller amounts of energy are needed to separate them further. In contrast, it appears that separating two colored particles requires a fixed amount of energy per distance, even at very large separations. Eventually, enough energy is added to the system to create a new particle–anti-particle pair, as in Figure 1-5. So if one tries to isolate a colored particle, the result is not an isolated particle, but new particles. This leads to "color confinement," which simply means that all observable particles are colorless. This is in agreement with experimental results, as every search for free quarks to date has failed to provide conclusive evidence.[13]

1.4 Structure Functions

While asymptotic freedom makes it possible to calculate the amplitude for a process using the simpler diagram in Figure 1-4b, rather than the more complicated diagram in Figure 1-4a, the momentum of the incoming hadrons is not specified in Figure 1-4b. In order to relate the hadron momentum to the momentum of the parton, one defines the "structure functions" of a hadron, $F_p^H(x)$. These give the probability of the hadron H containing a parton p with momentum fraction $x \equiv P_p/P_H$. P_H is the momentum of the hadron H, and P_p is the momentum of the parton in the direction of the hadron momentum. H and p can be any particle, although in this thesis, we will only be concerned with the cases where H is a proton or an anti-proton, and p is either a gluon or an up or down quark or anti-quark.

The cross section is calculated by

$$\frac{d^2\sigma}{dP_T^c dy_c}(\mathrm{p\overline{p}}\rightarrow c\mathrm{X}) = \sum_{a,b}\int dx_a dx_b F_a^{\mathrm{p}}(x_a) F_b^{\overline{\mathrm{p}}}(x_b) \cdot \frac{d^2\hat{\sigma}}{dP_T^c dy_c}(ab\rightarrow c\mathrm{X}) \tag{1.6}$$

where $F_{a,b}^{\mathrm{p},\overline{\mathrm{p}}}$ are the proton and anti-proton structure functions, and a and b are all the partons which can form a c, and $\frac{d^2\hat{\sigma}}{dP_T^c dy_c}(ab\rightarrow c\mathrm{X})$ is the parton level cross section for the process $ab\rightarrow c\mathrm{X}$.

1.5 Fragmentation

Just as Figure 1-4b does not explicitly relate the incoming hadron momenta to the incoming parton momenta, neither is the relationship between the outgoing partons and hadrons included in the diagram. As the colored particles in the final state begin to separate, additional quarks pop out of the vacuum. These combine to form colorless hadrons in a process known as "fragmentation."

Fragmentation is a low energy process, and as such cannot be calculated using perturbative QCD. One important aspect of fragmentation is that it takes place on a much longer time scale than the hard scattering. This means that the two

processes are "factorizable," *i.e.*, one can calculate the two separately, using different methods, and then combine the two results. For instance, one often calculates the hard scattering using perturbation theory, and then simulates the fragmentation using a phenomenological model that has been tuned to agree with experimental results.

Different problems require different amounts of knowledge of the fragmentation process. A common case, and the one needed in this thesis, is when only one particle produced by the fragmentation is of interest. In this case, only the "fragmentation function," $\mathcal{D}_p^H(z,Q)$, is needed. This is the probability for a parton p to form a hadron H with momentum fraction $z \equiv P_H^{\parallel}/P_p$. $P_H^{\parallel}$ is the momentum of H parallel to the parton direction, P_p is the momentum of p and Q is the energy scale of the process. Other definitions of z are possible, such as the energy fraction (E_H/E_p) or the light–cone variable $\left(\frac{E_H+P_H}{E_p+P_p}\right)$. Also, some momentum must be given to H perpendicular to the parton momentum, which is often assumed to have a Gaussian distribution.

The full formula for calculating inclusive cross sections in proton–anti-proton collisions is

$$\frac{d^2\sigma}{dP_T dy}(\mathrm{p}\overline{\mathrm{p}}\rightarrow H\mathrm{X}) = \sum_{a,b}\int dx_a dx_b F_a^{\mathrm{p}}(x_a)F_b^{\overline{\mathrm{p}}}(x_b)\cdot \sum_{c,d}\int dz_c d^3P_d \frac{d^5\hat{\sigma}(ab\rightarrow cd)}{dP_{T\,c}dy_c d^3P_d}(P_c/z_c)\mathcal{D}_c^H(z_c,Q) \tag{1.7}$$

where a and b run over quarks, anti-quarks and gluons, $F_{a,b}^{\mathrm{p},\overline{\mathrm{p}}}$ are the various structure functions, c is any particle that can form an H, and d is any particle that can be produced in association with c.

1.5.1 Petersen Fragmentation

One important source of charmonium at a high–energy collider is the decay of B hadrons. Thus, an understanding of the fragmentation of the b quark is important to this thesis. Heavy quark fragmentation is assumed to follow the model of Petersen *et al.*[14] Figure 1-6 shows the leading order diagram for b quark fragmentation. As

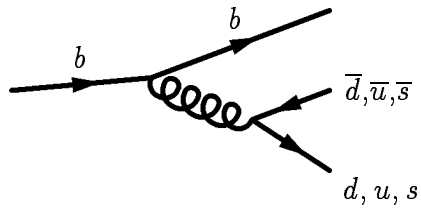

Figure 1-6: Feynman diagram of b quark fragmentation. The b quark and the light anti-quark form a hadron, and the other light quark fragments into other hadrons.

shown, this process violates conservation of energy, as $m_b < m_{\mathrm{B}}$. In practice, this is ignored, and it is assumed that soft gluons are exchanged with other fragmenting particles, which restores energy conservation without affecting the dynamics of the fragmentation.

Petersen fragmentation assumes that the kinematics of the fragmentation is completely dominated by the $1/Q^2$ dependence of the gluon propagator. The Q^2 of the gluon is

$$Q^2 = (E_b - E_{\mathrm{B}} - E_q)^2 - (\vec{P}_b - \vec{P}_{\mathrm{B}} - \vec{P}_q)^2 \tag{1.8}$$

where E_i and $\vec{P}_i$ are the energy and momentum of the b quark (b), B hadron (B) and the light quark (q), respectively.

The propagator is evaluated in a reference frame where $P_i \gg m_i$ for all the particles, also known as the infinite momentum frame. Conservation of momentum dictates that the momentum term in Equation 1.8 will be zero. The energy can be approximated by

$$E = P + \frac{1}{2}\frac{m^2}{P} + \mathcal{O}\left(\frac{m^4}{P^3}\right) \tag{1.9}$$

The momentum of the B hadron and the light quark transverse to the b quark direction are small, and are often neglected. Alternatively, m can be redefined to include the effects of the transverse momentum. Using Equation 1.9 for the energy and noting that $P_b = P_{\mathrm{B}} + P_q$ yields

$$Q^2 = \frac{1}{2}\left(\frac{m_b^2}{P_b} - \frac{m_{\mathrm{B}}^2}{P_{\mathrm{B}}} - \frac{m_q^2}{P_b - P_{\mathrm{B}}}\right) \tag{1.10}$$

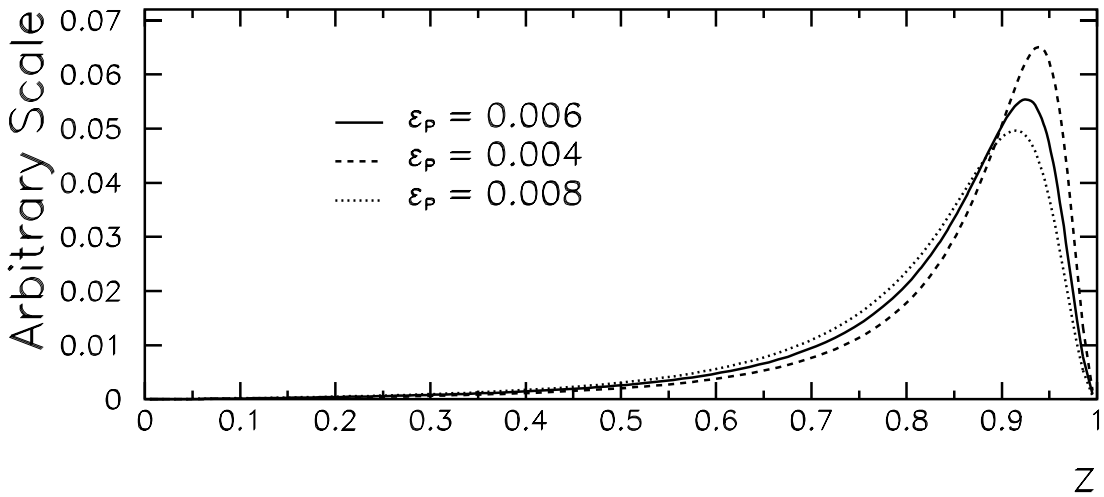

Figure 1-7: The Petersen fragmentation function, showing the central value and the variations used in this thesis. The three curves are normalized to the same area.

Using the fragmentation parameter

$$z \equiv \frac{P_{\mathrm{B}}}{P_b} \tag{1.11}$$

and assuming $m_b \approx m_{\mathrm{B}}$ leads to

$$Q^2 \propto 1 - \frac{1}{z} - \frac{\epsilon_P}{1-z} \tag{1.12}$$

where $\epsilon_P \equiv m_q^2/m_b^2$. The fragmentation function is then the square of the matrix element, taken to be $1/(Q^2)^2$, multiplied by the phase space factor $1/z$. The resulting fragmentation function is

$$\mathcal{D}_b^{\mathrm{B}}(z) = \frac{N}{z\left(1 - \frac{1}{z} - \frac{\epsilon_P}{1-z}\right)^2} \tag{1.13}$$

where N is a normalization factor. ϵ_P for B mesons has been measured to be $\epsilon_P = 0.006 \pm 0.001 \pm 0.002$. [15, 16, 17] The resulting function is shown in Figure 1-7.

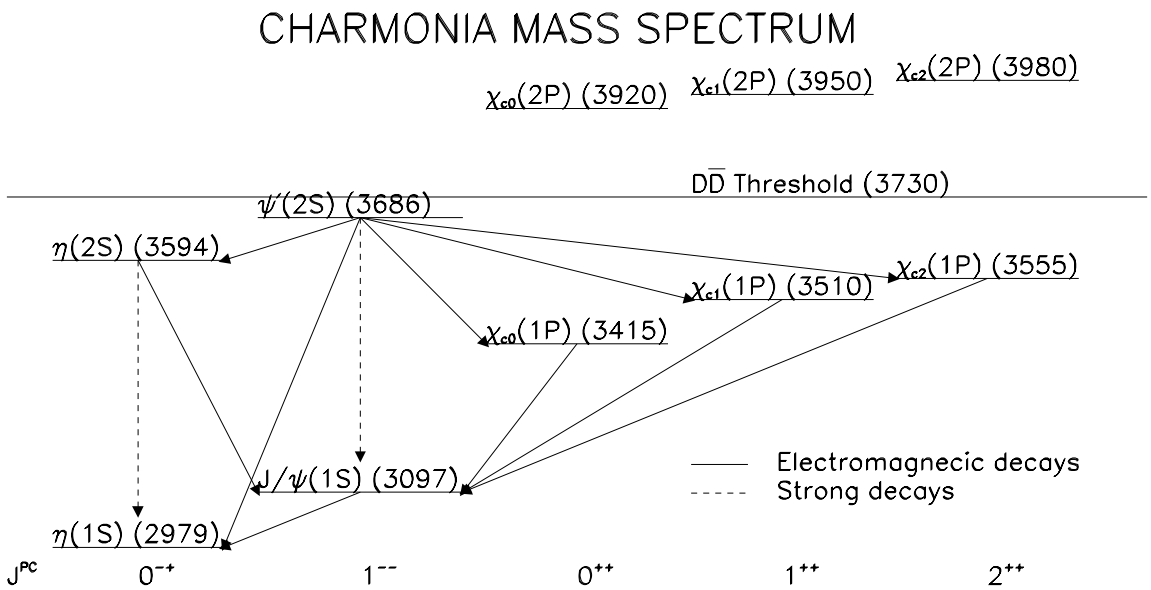

Figure 1-8: Charmonium mass spectrum. States with masses above the $D\overline{D}$ threshold decay almost exclusively into charmed mesons.

1.6 Charmonium Masses And Decay Modes

Naively, one would expect that charmonium would decay quickly, with the $c\overline{c}$ pair annihilating into gluons, producing a broad resonance. While this does happen, it occurs at a lower rate than other strong decays. After the $c\overline{c}$ pair annihilate into gluons, one or more of the resulting gluons must carry most of the energy, about 3 GeV. As we will see in the next section, at this energy α_S is fairly small, which reduces the rate. This is known as the Zweig rule.[18] Color conservation requires that at least two gluons be emitted. For ψ production, G-parity prohibits the decay into two gluons, so three gluons are required. As a result, the decay is a higher order process than most other strong decays, where only one soft gluon is exchanged. Electromagnetic decays, where either the pair annihilate into a virtual photon or a real photon is emitted, form a significant fraction of the decays of many charmonium states. This is important, as the decay of the ψ into two muons through a virtual photon is the decay mode which is reconstructed by this thesis and by many other analyses. One exception is states with masses larger than twice the D mass, which

decay almost exclusively into $D\overline{D}$. Since such decays proceed by the exchange of one soft gluon, the rate for these decays is much higher than the rate of radiative decays to other charmonium states.

The internal dynamics of the charmonium system is similar to the hydrogen atom or the positronium system. One difference is that, while positronium is bound together by exchanges of soft photons, charmonium is bound by exchanges of soft gluons. So while accurate calculations are possible for the energy levels of positronium, similar calculations of the masses of charmonium states are much more difficult. However, the quantum numbers that are used to describe positronium can also be applied to charmonium. The rotational quantum numbers in positronium result from the rotational invariance of the potential, while the radial quantum number is related to the time–independence of the potential. All of these properties are also true[4] for the QCD quark–quark potential, so similar quantum numbers exist, although the dependence of the energy levels is different.

The η_c is the lightest charmonium state. The $c\overline{c}$ pair is in an S-wave state[5], with the quark spins anti-parallel. The next higher state is the J/ψ. This is the S-wave state with parallel spins. The excited states are sometimes denoted by $\psi(n\mathrm{S})$ or by $\psi', \psi'', \ldots$ The P-wave states with parallel spins are denoted as χ_{cJ}, where $J = 0, 1, 2$ is the total angular momentum of the state. χ_c is a generic term that refers to any of the χ_{cJ}. Figure 1-8 shows the charmonium mass spectra and decay modes to other charmonium states. The $\eta_c(2S)$ is not well determined experimentally, and the shown decay modes, while expected, have not been observed. Other states, such as the P-wave spin singlet, and D-wave states, are expected to exist but are not expected to have significant contributions to ψ production. The decay of a D-wave state to a ψ

[4]The spin–orbit coupling breaks the rotational symmetry, just as it does in positronium. While the effect is larger than in positronium, it can still be treated as a small perturbation.

[5]S, P and D waves refer to the spatial portion of the wave function, *e.g.*, an S wave state has $L = 0$ and $J = 0$ or 1, depending on the configuration of the spins. One deviation from standard spectroscopic notation is that, for orbitally excited states, the radial quantum numbers start from 1 for each value of L. Thus, while the lowest lying $L = 1$ states are typically denoted by $2^S\mathrm{P}_J$ by atomic physicists, the particle physics designation is $1^S\mathrm{P}_J$

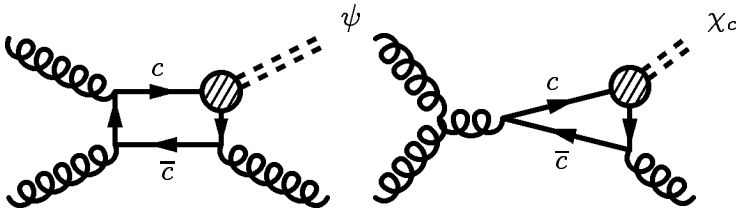

Figure 1-9: Leading order diagram for (left) J/ψ and $\psi(2S)$ production and (right) χ_c production with non-zero transverse momentum in the α_S expansion.

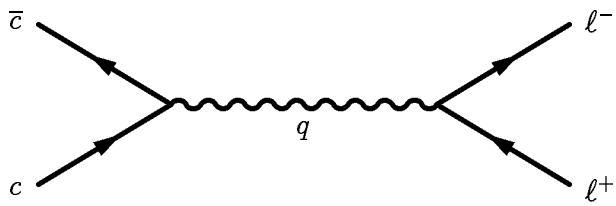

Figure 1-10: Leading order Feynman diagram for the decay $\psi \to \ell^+\ell^-$

requires $\Delta L = 2$, which is suppressed by an additional power of α. Feeddown from the P-wave singlet is also suppressed because of the need to flip the spin of one of the quarks.

1.7 Charmonium Production

There are two processes that dominate the production of charmonium in $p\overline{p}$ collisions. The first of these is the production of a $c\overline{c}$ pair, which combine to produce a colorless bound state. The other process is the production of a b or $\overline{b}$ quark, which fragments into a B hadron. This hadron can subsequently decay into a ψ and other hadrons, as in Figure 1-14.

1.7.1 Direct Production

The leading order diagrams for direct ψ and χ_c production with significant transverse momentum in $p\overline{p}$ collisions are shown in Figure 1-9. The $c\overline{c}$ quarks are produced in a color–singlet state, and the entire diagram can be calculated, except for the "blob" representing the hadronization of the quarks into a ψ or χ_c meson. The ψ diagram

can be calculated up to a factor related to the value of the ψ wave function at the origin,$|\psi(0)|^2$. This value can be determined from the ψ leptonic decay width. The partial width for the decay $\psi \rightarrow \ell^+\ell^-$ is given by[19]

$$, _{\ell^+\ell^-} = \frac{16\pi\alpha^2 Q^2}{M_\psi^2}|\psi(0)|^2 \tag{1.14}$$

where $\ell = e, \mu, \tau$ and $Q = \frac{2}{3}$ is the charm quark charge. This formula is derived from the Figure 1-10. The photon propagator contributes a factor of $1/q^2 = 1/M_\psi^2$. The $\ell^+\ell^-\gamma$ vertex contributes a factor of $\sqrt{4\pi\alpha}$ and the $c\bar{c}\gamma$ vertex contributes a factor of $Q\sqrt{4\pi\alpha}$, yielding

$$|\mathcal{M}|^2 \propto \frac{\alpha^2 Q^2}{M_\psi^4} \tag{1.15}$$

The integral over the lepton phase space is proportional to $q^2|\psi(0)|^2$, leaving the $1/M_\psi^2$ dependence. All of the quantities on the right hand side of Equation 1.14 are known except the wave function. Thus, a measurement of $, _{\ell^+\ell^-}$ provides a measurement of the ψ wave function at the origin.

There is a similar production mechanism which only contributes to J/ψ production. The $c\bar{c}$ pair can form a χ_c state, which decays to a J/ψ through an electromagnetic transition ($\chi_c \rightarrow J/\psi\gamma$). As all the known χ_c states are either below the $\psi(2S)$ mass, or above the threshold for decay to charmed mesons, this mechanism does not contribute to $\psi(2S)$ production.

χ_c production diagrams contain charm quark loops which are connected to two gluons, while the charm quark loops in the ψ production diagrams are connected to three, which is a result of G parity conservation. Since the gluon has negative G parity, a state consisting on N gluons has $G = (-1)^N$. Thus, the χ_c, with even G-parity, can only couple to states with an even number of gluons, while the ψ, with odd G-parity, only couples to states with an odd number of gluons.

Calculating the leading order diagram for $\psi(2S)$ production in Figure 1-9,[20, 21, 22] one finds that the cross section is expected to be negligible compared to that resulting from B decays. However, in the analysis that is described in this

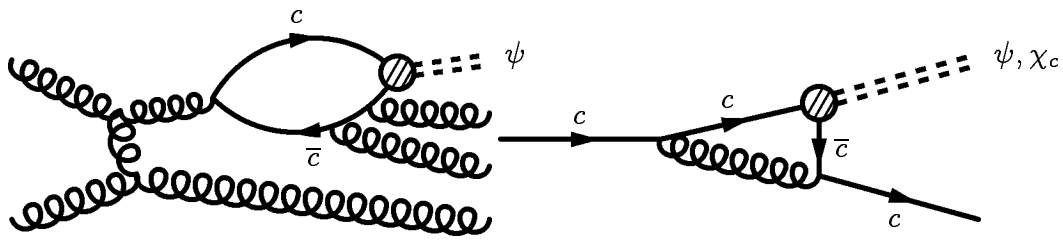

Figure 1-11: Gluon (left) and charm (right) fragmentation production of ψ in the color singlet model. The production of the initial charm quark has been suppressed for clarity.

thesis, we find that direct production of $\psi(2S)$ is *larger* than that from B production! Direct $\psi(2S)$ production exceeds the predicted rates by factors of 60-90. The "CDF $\psi(2S)$ anomaly," as this has come to be called, is the most striking disagreement between particle physics theory and experimental results in recent years. After the χ_c contribution to the J/ψ cross section is removed, it also exhibits a similar discrepancy. Since these results were initially seen, there have been several proposed mechanisms to explain this excess.

The excess could be explained if there is a state with a mass above the $\psi(2S)$ mass that had a significant branching ratio to the $\psi(2S)$, and a large production cross section. One possibility is the ${}^3D_2$ state. The predicted mass is above the threshold for decay in $\mathrm{D}\overline{\mathrm{D}}$. However, that decay is not allowed by the quantum numbers. The first allowed decay is into $\mathrm{D}\overline{\mathrm{D}}^*$, but the predicted mass is just below the threshold for that decay. So this state may have a large branching ratio to $\psi(2S)$.

1.7.2 Fragmentation Production

Two other effects can enhance the predicted cross section for directly producing a $\psi(2S)$. One is the fragmentation contribution.[57] Figure 1-11 shows a Feynman diagram involved in ψ production which is $\mathcal{O}({\alpha_S}^5)$. Since the leading order diagram is $\mathcal{O}({\alpha_S}^3)$, this diagram should have a small contribution to the total cross section. However, if the ψ has a large transverse momentum $P_T \gg m_\psi$, then the diagram will be dominated by configurations where the gluon has $Q^2 \sim m_\psi^2 \ll E^2_{\mathrm{gluon}}$. In this

case the gluon is nearly real, and the diagram is enhanced by a factor of $(P_T/m_\psi)^2$. When P_T becomes large enough, this diagram dominates the leading order diagrams. Because this process produces a (nearly) on-shell gluon which fragments into a ψ, it is referred to as gluon fragmentation production. This mechanism also produces χ_c mesons; in fact, for the χ_c, one less gluon needs to be radiated, so the process is of order ${\alpha_S}^4$. A ψ can also be produced by similar diagrams where a charm quark fragments, as shown in Figure 1-11, although this is not as important, because the cross section to produce a charm quark is significantly smaller than the cross section to produce a gluon.

1.7.3 Color Octet Production

So far, all the perturbative processes have produced a color–singlet $c\bar{c}$ pair which hadronizes into a ψ or χ_c, which is described as the Color Singlet Model (CSM). The radiated gluons cannot be too soft, or perturbation theory will fail. A few years ago, Bodwin, Braaten and Lepage devised a method for calculating the fragmentation function for a color octet $c\bar{c}$ pair into charmonium. It uses non-relativistic QCD (NRQCD)[23], which is an effective potential model, inspired by Heavy Quark Effective Theory (HQET).[24, 25, 26] It is based on the realization that, inside a charmonium state, the two quarks will be moving fairly slowly, with $v_c^2 \approx 0.25$. Thus, a double expansion, in powers of α_S and v_c, is possible. The terms that are of lowest order in α_S may be of higher order in v_c, while terms of higher order in α_S may be of lower order in v_c, so that which terms dominate the cross section depends upon the power of both α_S and v_c. Since the $c\bar{c}$ pair is often produced a color octet state in this model, the model is named the Color Octet Model (COM).

As before, the entire process cannot be calculated using perturbation theory. However, a non-perturbative part can be factored out. This part is a well–defined matrix element, which could be calculated using lattice QCD, or extracted from experimental measurements. It can be argued that the matrix element is independent of the kinematics in the perturbative part, which results in an unknown normalization, but

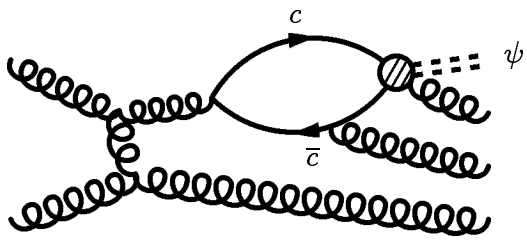

Figure 1-12: Gluon fragmentation production of ψ in the color octet model. In this case, one gluon is radiated during the non-perturbative process.

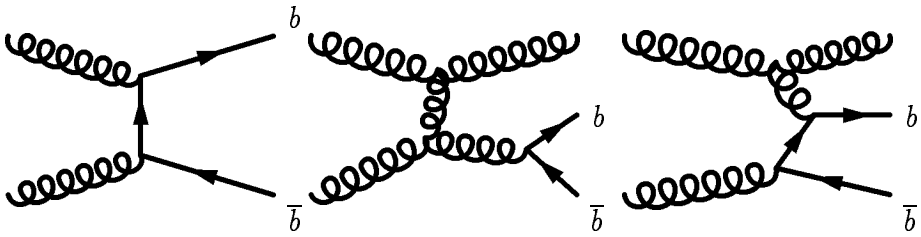

Figure 1-13: Feynman diagrams for b production from gluon fusion (left), gluon splitting(center) and flavor excitation (right).

does not affect the shape. Furthermore, the matrix elements are "universal," so a matrix element measured at one experiment can be used to make predictions for another experiment, or compared with the matrix element measured at that experiment. Lastly, naive power counting provides an order of magnitude estimate for the matrix element.

In terms of Feynman graphs, what happens is that one or more of the gluons radiated from the $c\bar{c}$ pair is removed from the perturbative portion, and added to the non-perturbative portion, as shown in Figure 1-12. As the gluon is now being treated in a non-perturbative manner, it can become extremely soft, greatly enhancing the contribution of the diagram. In fact, a typical approximation is to assume that the gluon carries no energy, only the excess color.

1.7.4 B Production

The other mechanism for ψ production is from B decays: QCD processes produce a b quark, which fragments into a B hadron and subsequently decays into a ψ and other particles. At next–to–leading order, the diagrams for b quark production can

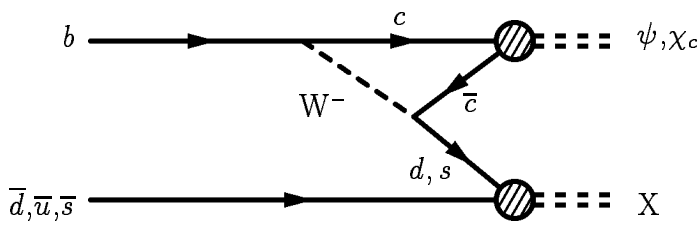

Figure 1-14: Typical B meson decay diagram for charmonium production.

be grouped into three classes, shown in Figure 1-13, each of which have distinct characteristics. The two b quarks produced by gluon fusion are separated by π radians in azimuthal angle, and produce two well separated jets. Gluon splitting tends to produce b quarks which are closer together, as the mass of the virtual gluon tends to be small. As a result, the decay products of the two quarks may appear to come from a single parent, especially after fragmentation effects and experimental resolution are included. Flavor excitation is often the result of the gluon scattering off of one of the virtual b quarks that form the cloud around the valence quarks. In this case, the other b proceeds close to the initial proton or anti-proton direction.

After the b quark fragments into a B hadron, it can decay to a ψ or χ_c through diagrams such as Figure 1-14. This decay is suppressed relative to the decay B$\rightarrow$DXfor several reasons. First, the W must decay into $\overline{c}s$, whereas for the B$\rightarrow$DX decay, all of the possible W decay modes are allowed. This reduces the rate by about a factor of three. Furthermore, the $\overline{c}$ must have the same color as the c quark, as the fragmentation of the color octet $c\overline{c}$ state into charmonium is suppressed. This introduces another factor of three. Lastly, the c and $\overline{c}$ quarks must have similar momenta, so that they can form a bound state. This results in the relatively small branching ratios of $\mathcal{B}(\mathrm{B}\rightarrow J/\psi\mathrm{X}) = 1.13 \pm 0.07\%$[27] and $\mathcal{B}(\mathrm{B}\rightarrow\psi(2S)\mathrm{X}) = 0.34 \pm 0.05\%$[27]. While these branching ratios are small, it is an experimental fact that the two muons from the ψ decay provide an excellent signature for an experimental trigger, so the process B$\rightarrow\psi$X is tremendously useful from a practical standpoint.

1.7.5 Production Summary

Charmonium can be produced in proton–anti-proton collisions through three mechanisms:

1. The hard scattering can create a $c\overline{c}$ pair, which form a bound state, directly producing a ψ.

2. When the $c\overline{c}$ pair bind together, the resulting bound state can be a χ_c meson, which may decay to $J/\psi\gamma$.

3. A $b\overline{b}$ pair may be produced in the interaction. After fragmentation forms a B hadron, the hadron can decay to ψX or χ_cX, with the χ_c decaying to $J/\psi\gamma$.

At high P_T, fragmentation will be the dominant method of producing the $c\overline{c}$ pair for the first two processes, even if it is a higher–order process. As all the χ_c states have masses which are either less than the $\psi(2S)$ mass or larger than the threshold for the decay into open charm, the second mechanism does not contribute to $\psi(2S)$ production. Direct production of ψ mesons without an intermediate B or χ_c state is expected to be small within the Color Singlet Model, so that nearly all $\psi(2S)$ mesons should be B daughters, while χ_c decays may be responsible for a significant portion of the J/ψ production.

Chapter 2

Experimental Apparatus

The data for this analysis comes from $p\overline{p}$ collisions in the Tevatron, at the Fermi National Accelerator Laboratory (FNAL or Fermilab). The Tevatron is currently the highest energy collider, colliding protons and anti-protons at a center-of-mass energy of 1.8 TeV. The data was collected by the Collider Detector at Fermilab (CDF). CDF is a general purpose detector, built to study the $p\overline{p}$ interactions with large transverse momentum (P_T).

2.1 Coordinate System

The only preferred direction at a proton–anti-proton collider with unpolarized beams is the beam axis, which is defined as the z axis. Physical processes are invariant under rotations about this axis, so a cylindrical coordinate system is an obvious choice. R indicates the radial distance from the beam line, and ϕ denotes the azimuthal angle. θ is defined as the angle relative to the z axis.

Interactions at hadron colliders often have a large boost along the beam direction, so a form of the cross section that is invariant under such boosts is useful. We start from the invariant cross section, $E\frac{d^3\sigma}{(dp)^3}$. If the cross section is independent of ϕ, this can be written as

$$E\frac{d^3\sigma}{(dp)^3} = E\frac{d^2\sigma}{\pi P_T dP_T dP_z} \tag{2.1}$$

where P_T denotes the momentum transverse to the beam direction. While this form as a whole is invariant, it contains two variables which do change when boosted in the z direction. These can be removed by a change of variable. The new variable, y, must satisfy

$$E\frac{dy}{dP_z} = 1 \tag{2.2}$$

Solving this equation yields

$$y = \frac{1}{2}\ln\left(\frac{E+P_Z}{E-P_Z}\right) \tag{2.3}$$

which is called the rapidity of the particle. Substituting this into Equation 2.1 yields

$$E\frac{d^3\sigma}{(dp)^3} = \frac{d^2\sigma}{\pi P_T dP_T dy} \tag{2.4}$$

The rapidity is often approximated by the pseudo-rapidity

$$\eta \equiv \frac{1}{2}\ln\left(\frac{P+P_Z}{P-P_Z}\right) = -\ln\left(\tan\frac{\theta}{2}\right) \tag{2.5}$$

which has the experimental advantage of being independent of the mass of the particle. The rapidity and the pseudo-rapidity are identical for massless particles, and nearly the same for massive particles when ${P_T}^2 \gg m^2$.

2.2 The Accelerator

Figure 2-1 shows the steps involved in setting up the collider for a store. The first step in creating the proton beam involves the Cockcroft-Walton hydrogen gas bottles. In these bottles, electrons are added to hydrogen atoms, creating negatively charged H^- ions. These are extracted from the gas bottles using a voltage source which accelerates the ions to an energy of about 750 keV. The ions are then inserted into a linear accelerator called the Linac. The Linac accelerates the ions to an energy of 400 MeV. As the ions leave the Linac, they pass through a carbon foil, which strips the electrons away from the ions, leaving a beam of positively charged protons, which

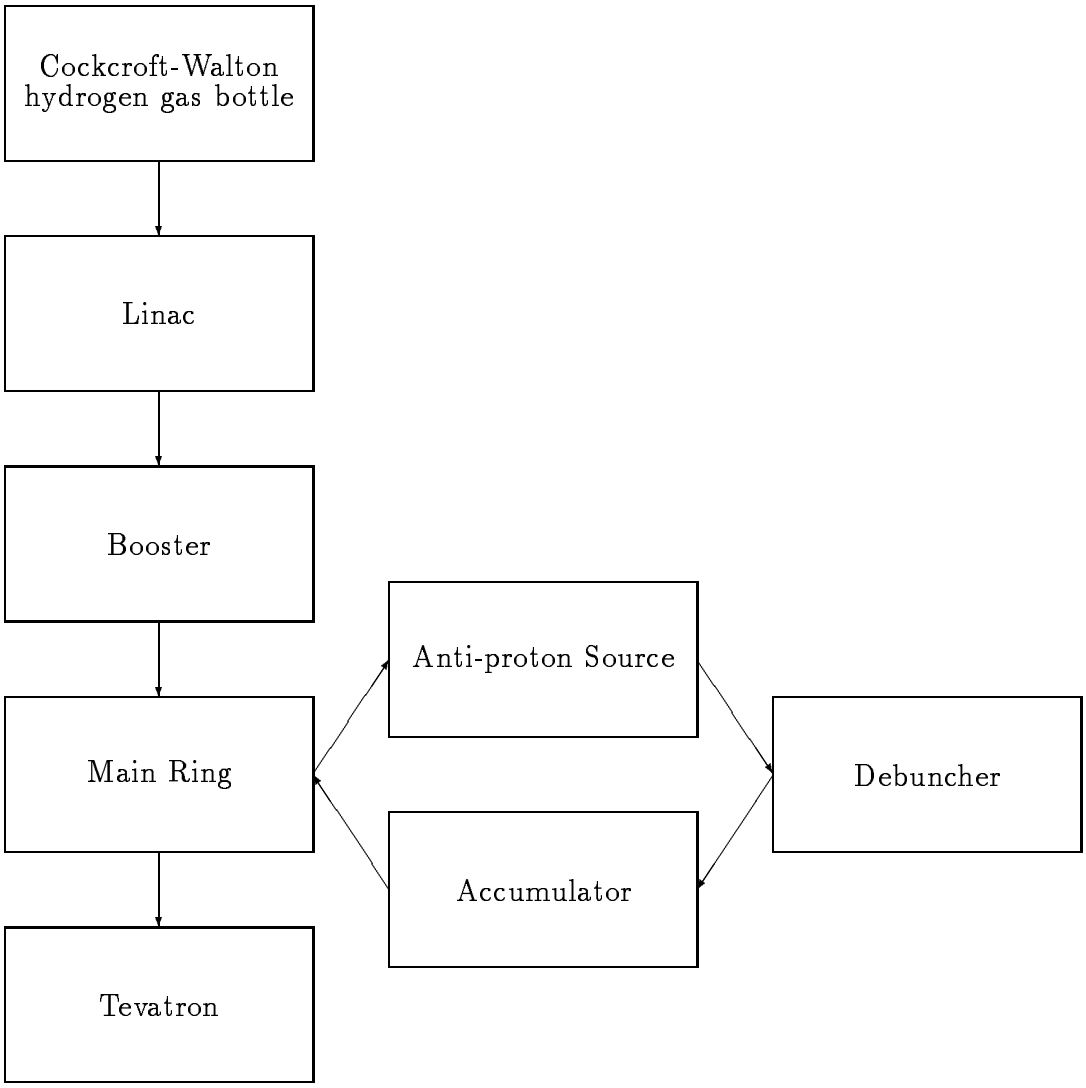

Figure 2-1: Elements in the generation and acceleration of protons and anti-protons at Fermilab.

enter the Booster. The Booster is a 500 foot diameter synchrotron. The protons circle approximately 20,000 times inside the Booster while being accelerated to an energy of 8 GeV, before being injected into the Main Ring. The Main Ring is another synchrotron, with a radius of 1 mile. It contains about 1000 copper-coiled magnets, and accelerates the proton beam to an energy of 150 GeV, after which it is injected into the Tevatron. The Tevatron is yet another synchrotron, located just below the Main Ring. It is similar to the Main Ring, except that it uses superconducting magnets. Cooled by liquid helium, the Tevatron operates at a temperature of $-450°$ F ($-268°$ C), a mere 5K above absolute zero. The Tevatron is capable of accelerating protons to an energy of 1 TeV. The data used in this analysis was collected with proton and anti-proton beams at 900 GeV.

The initial stages of the anti-proton beam creation are the same as for the proton beam. Once the proton beam enters the Main Ring, it is only accelerated to 120 GeV. The beam is then extracted from the Main Ring and collided with a tungsten target. This produces a large variety of particles, including anti-protons. The anti-protons are selected and transported to the Debuncher. Stochastic cooling[28] is used to collimate the anti-protons into a narrow beam of mono-energetic particles. They are then inserted into the accumulator. While the proton beams can be generated almost instantly, it takes several hours to build up a large store of anti-protons. Once a sufficient number of anti-protons have been accumulated, they are inserted into the Main Ring and the Tevatron, moving in the opposite direction as the proton beam. Figure 2-2 shows the relations between the accelerators.

When operating as a proton–anti-proton collider, the Tevatron is filled with six bunches of protons, and six bunches of anti-protons. A pair of bunches pass through an interaction region every 3.5 μs, which requires detectors that can detect signals, be read out and reset for the next measurement at a very high rate. Other accelerator parameters are shown in Table 2.1.

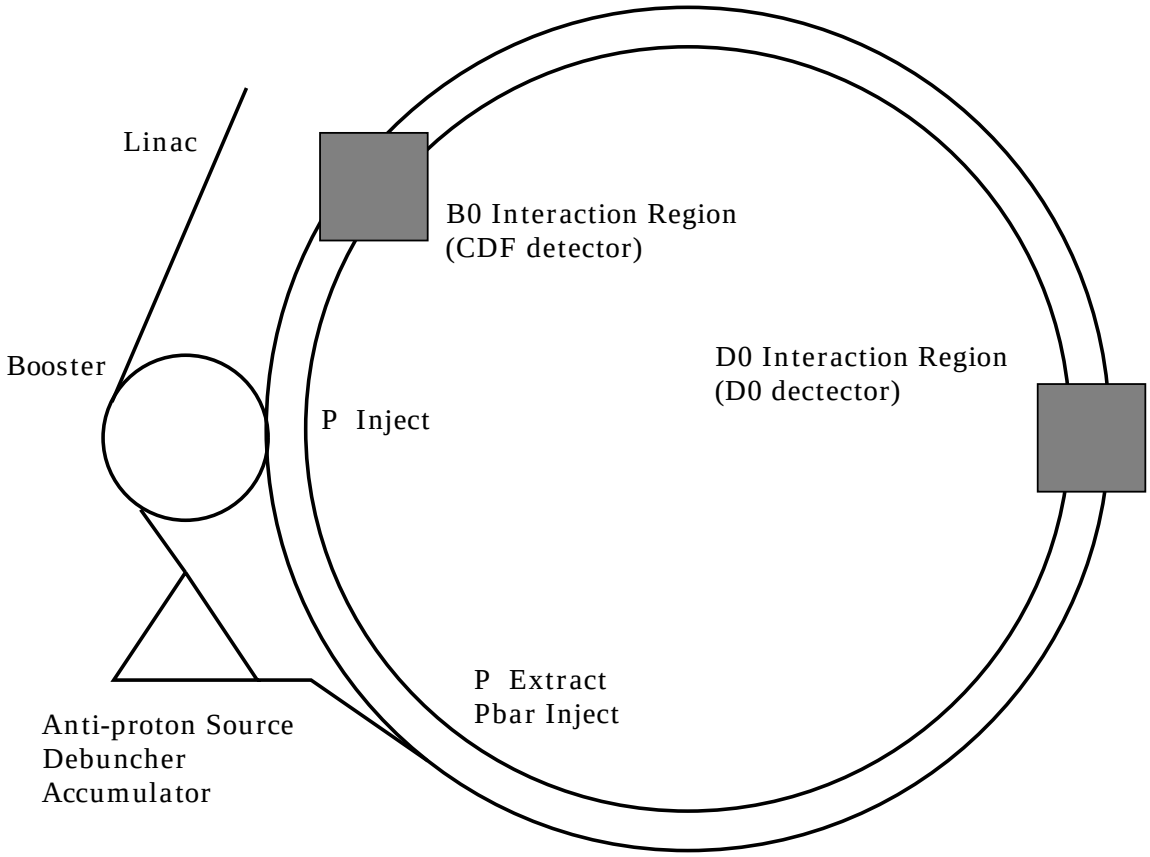

Figure 2-2: Schematic diagram of the particle accelerators at Fermilab.

Beam Energy	900 GeV/c/ beam
Luminosity	$1-10\times10^{30}\mathrm{cm}^{-2}/\mathrm{s}$
Bunches/Beam	6
Bunch Spacing	3.5μs
Protons/Bunch	1×10^{11}
Anti-protons/Bunch	3×10^{10}
Collision Region (RMS)	30 cm
Beam Size	$\sim 40\mu$m
Beam Pipe	1.5 in. diameter beryllium

Table 2.1: Tevatron Collider parameters for the 1992-1993 run.

2.3 CDF

There are six interaction regions at the Tevatron where the proton and anti-proton beams can collide, the second of which is surrounded by the Collider Detector at Fermilab (CDF). The D0 detector is located at the fourth interaction point, and the remaining four are vacant. An overview of the components of the detector used in this analysis are described below. A full description of the detector can be found in [29].

2.3.1 Solenoid

The tracking chambers used at CDF are surrounded by a NbTi/Cu superconducting solenoid. This solenoid produces a 1.412 T magnetic field which permeates a cylindrical region 4.8 m in length and 3 m in diameter. A steel yoke returns the magnetic flux, in addition to supporting the calorimeters described below. A precise map of the field exists, and is used to perform offline corrections, including corrections for non-uniformities in the magnetic field.

2.3.2 Central Tracking Chamber

The Central Tracking Chamber (CTC) is a cylindrical drift chamber surrounding the beam line. As a charged particle passes through the chamber, it ionizes the gas. The ionization electrons drift towards high voltage wires, where the charge is collected. While the electron drift direction can be determined from the geometry and the field strengths, a single wire cannot determine whether the "hit" originated on the left or the right of the wire.

The chamber is logically divided into regions called cells. Since there is no physical division between the cells, this is called an open cell geometry. Each wire is capable of measuring the arrival time of multiple hits, so a particle passing near the wire and a particle passing farther away are distinguished by two separate pulses arriving at the wire at distinct times. Although chambers can be designed where each cell has only

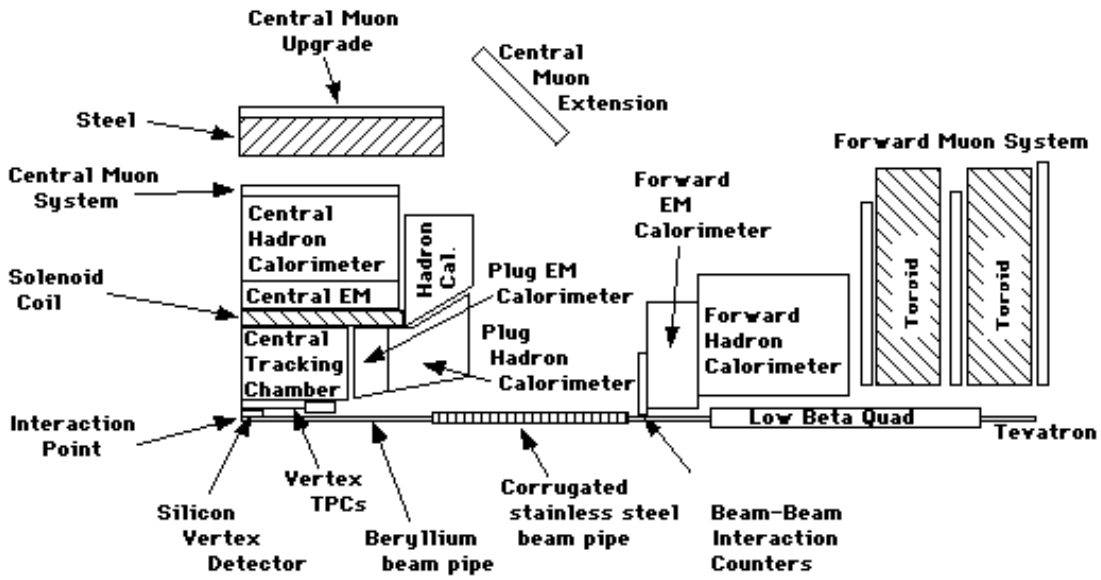

Figure 2-3: Cut-away view of one half of CDF. The detector is forward-backward symmetric.

one wire, the CTC has multiple wires per cell. There are several reasons for having multiple wires in each cell. If one of the wires fails, the other wires enable the cell to still be used. Further, by looking at the correlations between the hits on nearby wires, corrupted hits can be eliminated. The left-right ambiguity inherent in drift chambers can be removed by reconstructed track stubs within a cell, and extrapolating back to the beam line.

The CTC consists of 9 superlayers alternately providing $R-\phi$ and $R-z$ measurements. Five superlayers provide 12 radial $(R-\phi)$ measurements each, while the other four superlayers each provide 6 stereo $(R-z)$ measurements of the track for a total of 84 wires. It covers a pseudorapidity range of $|\eta| < 1.1$.

Within the radial superlayers, the wires are positioned at a 45° angle relative to the radial direction. There are several reasons for this. Neighboring cells in each superlayer are close enough that they overlap in the azimuthal directions. This means that every high momentum track will pass close to at least one wire in each superlayer. This fact is exploited by the Central Track Processor (CFT), which finds tracks for the

trigger. Tilting drift cells also improves the electron drift characteristics. Electrons drifting in a gas with crossed electric and magnetic fields move at an angle β relative the electric field, where β is approximately given by

$$\tan\beta = \frac{v(E, B = 0)B}{kE} \tag{2.6}$$

where $v(E, B = 0)$ is the drift velocity without a magnetic field, B is the magnetic field strength and k is a parameter which depends on the type of gas and E. $k \approx 0.7$ for the normal operating conditions in the CTC. The strong magnetic field at CDF and the desire to operate the chamber at the lowest reasonable voltage indicate that β will be large. By having a large tilt, the electron drift direction becomes almost azimuthal. This decreases the amount of dead space near the edge of the cells, and makes the distance-to-time relationship more linear. A third advantage comes in resolving the left-right ambiguity. In each superlayer, two stubs can be reconstructed from each real track. The real stub uses the correct assignment of all the hits, and the "ghost" stub uses the incorrect assignment on every hit. The ghost stub is rotated by $\Delta = \tan^{-1}(2\tan\beta)$ relative to the true track direction. This large rotation makes it simple to reject the ghost stub.

Track reconstruction begins by searching for groups of hits within each superlayer that are consistent with a track. In the radial superlayers, these hits are fit to a circle, while the stereo hits are fit to a line. After finding track "segments" in each superlayer, two algorithms independently attempt to combine the radial segments into a two dimensional track. In most cases, both algorithms will find the same track with the same hits, or one algorithm will fail to find the track. In these cases, merging the results of the two algorithms is trivial. Some of the time, the algorithms reconstruct two similar tracks, which share a significant fraction, but not all, of their hits. In this case, the track that used the largest number of hits is chosen, and the other is discarded. If both have the same number of hits, one is chosen at random. This track is then merged with the stereo segments to form a three-dimensional track.

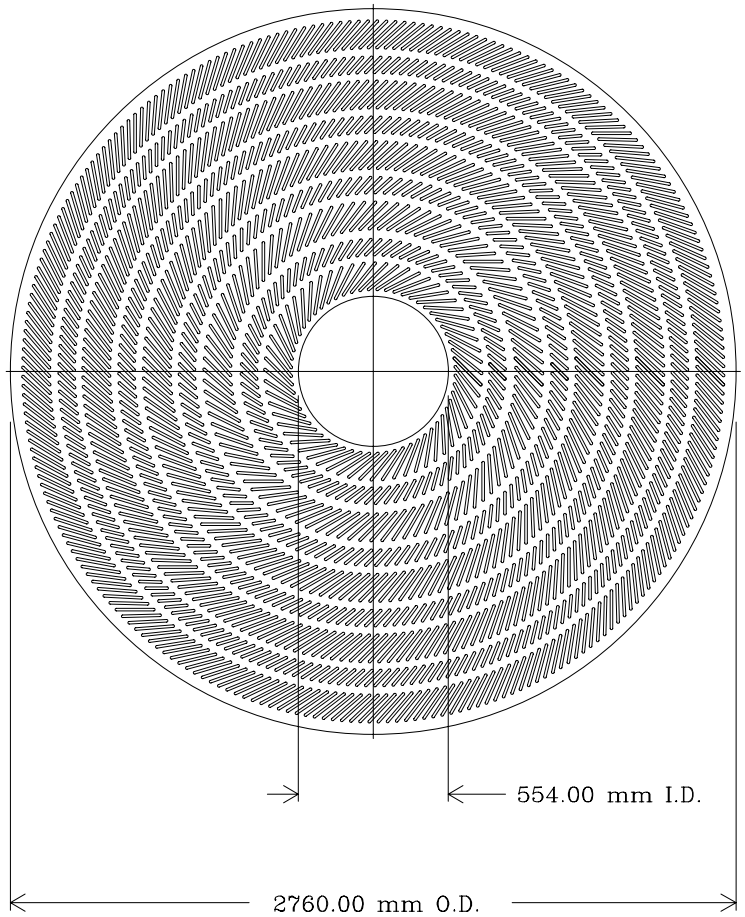

Figure 2-4: End-view of the CTC. The boxes represent superlayers, each of which contain 6 or 12 wires.

Number of layers	84
Number of superlayers	9
Stereo angle of stereo superlayers	3°
Number of super cells per layer	30, 42, 48, 60, 72, 84, 96, 108, 120
Sense wire spacing	0.1 cm
Tilt angle	45°
Radius at innermost sense wire	30.9 cm
Radius at outermost sense wire	132 cm
Inner Diameter	0.55 m
Outer Diameter	2.76 m
Wire length	321.4 cm
Electric Field	1350 V/cm
Magnetic Field	1.412 T
Nominal $R-\phi$ resolution	200 μm
Nominal $R-z$ resolution	4 mm
Nominal $\delta P_T/P_T$	$0.002 \cdot P_T$(GeV/c)

Table 2.2: CTC mechanical characteristics and nominal resolutions

2.3.3 Silicon Micro-vertex Detector

A key component of this analysis is the separation of B events from other production mechanisms. This requires that the ψ decay vertex be measured with an accuracy better than the B lifetime of $c\tau_{\mathrm{B}} \approx 450\mu$m. This is accomplished using the Silicon Micro-vertex Detector (SVX). The SVX is constructed from "ladders" of single sided, DC-coupled silicon. Each ladder is 25.5 cm long and covers approximately 30° of azimuthal angle. A "wedge" is four ladders covering the same azimuthal region at different radii, numbered from 0 to 3. The innermost ladder is 3.0 cm from the beam line, and the outermost is at 7.9 cm. The entire detector consists of 24 wedges, which are divided into two "barrels." There is one barrel on the east side, and one barrel on the west side of the detector, with a gap of 2.15 cm in the middle. The ladders in each wedge are rotated by 3°, which allows ladders in neighboring wedges to overlap slightly, although there is no overlap in layer 0. The strip pitch of the first three layers is 60 μm, while the outermost layer has a pitch of 55 μm. Each ladder is read out from electronics on one end of the ladder, and only provides $R-\phi$

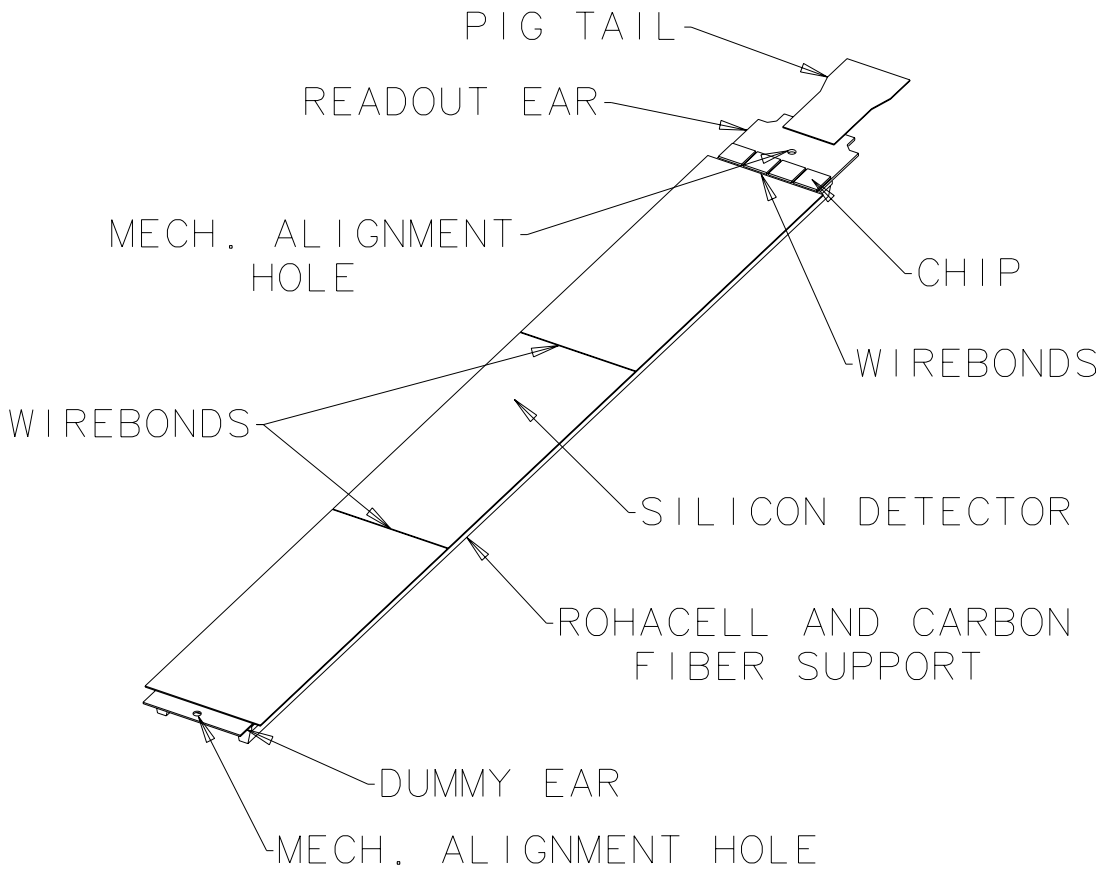

Figure 2-5: One ladder of the SVX detector. The three crystals, the readout electronics and the mounting equipment are shown.

information.

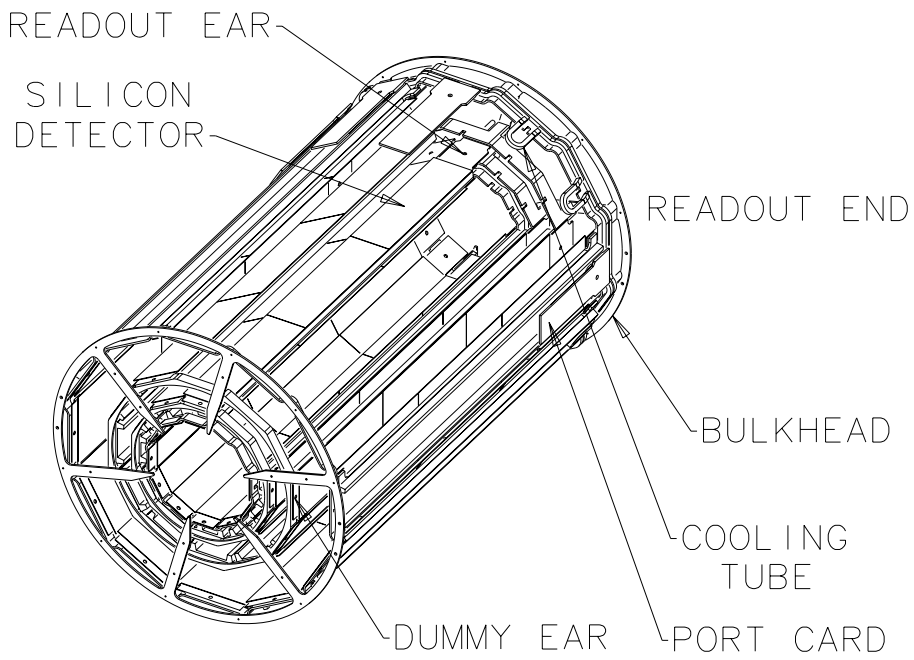

Figure 2-6: Cut-away isometric view of one SVX barrel.

Alignment

Charged particles passing through the SVX typically deposit charge in several strips. Thus, although the strips are separated by 60 μm, by clustering several strips together, and considering the amount of charge in each strip, an accuracy of about 15 μm can be achieved. To make use of this accuracy, the location of the SVX must be known to a similar accuracy. The SVX alignment is measured with two distinct methods.

As the detector was constructed and installed, measurements were made to provide an initial alignment. After the Tevatron began operating, reconstructed tracks were used to increase the accuracy of the alignment. The location of the three inner layers

Layer	Face	Radius (cm)	Total Width (cm)	Active Width (cm)	Pitch (μm)	Num. of Strips	Num. of Chips
0	IN	2.99	1.60	1.54	60	256	2
1	OUT	4.27	2.37	2.30	60	384	3
2	OUT	5.70	3.14	3.07	60	512	4
3	IN	7.85	4.29	4.22	55	768	6

Table 2.3: SVX layer characteristics

relative to the outermost layer in each wedge was measured using the residuals of track measurements. Misalignments in the outermost layer then became misalignments between wedges. This was corrected using electrons from W decays, where the track is nearly straight, and originates from the beam position.

The alignment of the SVX relative to the beam line was performed by using the SVX to measure the beam position. For each run, an offline job would reconstruct high momentum tracks, and use these tracks to measure the position of the beam. This required that an accurate measure of the location of the SVX relative to the rest of the CDF detector be made. Figure 2-7 shows the beam position, as measured by the SVX.

Offline Reconstruction

Track reconstruction begins by grouping strips with excess charge into clusters. After subtracting pedestals, contiguous strips above a threshold are grouped into a cluster. The threshold is based on the measured noise in each strip, and becomes less stringent as more strips are added to the cluster. The charge-weighted centroid of the cluster is used as the position of the cluster. For clusters with $n \geq 4$ strips which had sufficient charge deposition, the error on the cluster position is $np/\sqrt{12}$, where p is the strip pitch. For smaller clusters, a value derived from track residuals is assigned.

These clusters are then converted into tracks by extrapolating CTC tracks. The CTC fit is extrapolated to the outermost SVX layer. A road is defined, using the

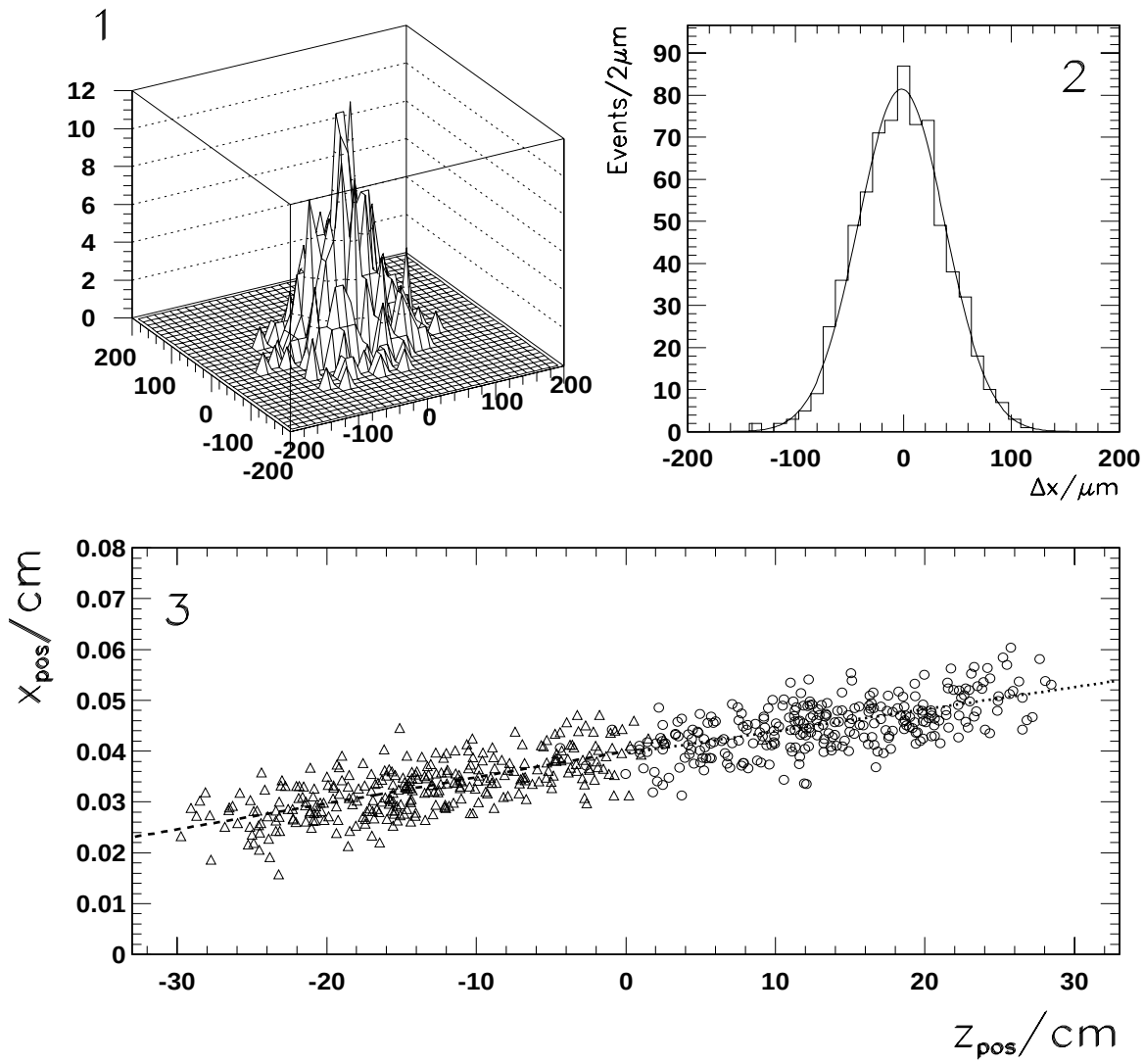

Figure 2-7: Beam profiles as measured by the SVX. (1) shows the distribution of vertices in the $x - y$ plane, after correcting for the z position. (2) shows the x projection. (3) shows the movement of the beam in the x direction as z changes.

extrapolated intersection, and the track parameter error matrix. For each cluster that lies inside the road, a candidate track is created by refitting the CTC track, including the new cluster. This procedure is then iterated over the three remaining layers. Track candidates with only one cluster are eliminated, and the χ^2 must be less than a maximum value. The candidate with the largest number of hits is selected, and all others are rejected. If more than one track has the same (maximum) number of hits, the candidate with the smallest χ^2 is used.

When combined with a CTC track, the SVX provides an impact parameter resolution of $\delta b = (13 + 40/P_T)\mu$m and a transverse momentum resolution of $\delta P_T/P_T = \sqrt{(0.9P_T)^2 + (6.6)^2} \times 10^{-3}$ where P_T is measured in GeV/c. The impact parameter resolution is excellent for transverse momenta above about 1 GeV/c. For smaller values, multiple scattering quickly degrades the resolution. All the tracks used in this analysis will have transverse momenta larger than 2 GeV/c, so this will not be a problem. Primary vertices have a Gaussian distribution with a width of about 27 cm, while the SVX only reaches to $\pm$25cm, so only about 60% of the CTC tracks can be augmented with SVX information.

2.3.4 Vertex Time Projection Chambers

Both the proton and anti-proton bunches have finite lengths, which causes the location of the vertices to be spread along the beam line. The vertices are approximately Gaussianly distributed, with a width of about 27 cm. While the SVX and the CTC provide excellent resolution in the transverse plane, the $R - z$ reconstruction is not as accurate. To improve the measurement of the location of vertices along the beam line, the Vertex Time Projection Chambers (VTX) are used. The VTX is an upgrade of a similar chamber (VTPC) used in previous runs.

The VTX consists of two projection chambers, covering the region of $|\eta| < 3.25$ out to a radius of 22 cm. Each chamber extends 1.5 m along the beam line beyond the nominal interaction point, and contains 28 octagonal modules, with a 4 cm drift distance between the wires. The 16 innermost modules, those surrounding the SVX,

contain 16 sense wires in the $R - \phi$ plane perpendicular to the radial direction. The last ten modules have 24 wires, allowing measurements closer to the beam. The two chambers are rotated by 11.3° about the beamline to improve attempts at ϕ reconstruction. A 50-50 mixture of argon and ethane is circulated through the chamber to provide an ionization medium. Each sense wire provides an $R - z$ measurement for each particle passing through the octant. Combining the measurements from the wires, the z position of the particle and its slope in the $R - z$ plane can be reconstructed.

The VTX is able to reconstruct many more tracks than the CTC for two reasons. First, it has coverage out to very large values of η. It is able to reconstruct tracks that exit through the side of the CTC before leaving enough hits to be reconstructed, or which don't even enter the CTC. Also, since it is closer to the beam, low momentum tracks which curve back upon themselves can be reconstructed with much higher efficiency in the VTX than in the CTC. These "extra" tracks allow the VTX to locate vertices along the beam line much better than the CTC. Primary vertices are identified by finding the intersection of the reconstructed tracks with an accuracy of 1-2 mm, depending on the multiplicity of the event.

2.3.5 Calorimeters

Most energetic particles, when passing through matter, induce particle showers. Electrons will radiate a photon by bremsstrahlung, which then converts into an electron-positron pair, creating a chain reaction which lasts until the initial electron's energy has been spread amongst enough particles that new particles can no longer be made. Photons create similar electromagnetic showers. Hadrons produce showers by inelastic collisions with the protons and neutrons in the matter.

One exception is muons[1]. The length scale of an electromagnetic shower is propor-

[1]An even more impressive exception is neutrinos. A neutrino can penetrate over a light-year of water without interacting. Fortunately, they interact just as rarely with the muon chambers, so they can be safely ignored in this analysis.

tional to the square of the particles mass. This means that, for a muon, approximately 40,000 radiation lengths (the distance over which an electron loses all but $1/e$ of its energy) is needed for a muon electromagnetic shower. The CDF detector is not even close to being this thick, not to mention the fact that other processes would drain the muon of its energy before it traversed even a small fraction of this distance. The muon does not undergo strong interactions, so the inelastic scattering that produces hadronic showers does not affect it. A muon will normally lose energy only by ionizing the medium through which it is passing, which is a slower process than either electromagnetic or hadronic showers.

The central region of CDF contains two calorimeters designed to measure the energy deposited by these showers. The Central Electromagnetic Calorimeter (CEM) covers the region $|\eta| < 1.1$. It consists of 31 layers of lead interleaved with 31 layers of 5 mm SCSN-38 polystyrene, which functions as a scintillator. The light is wave-shifted and fed into a photomultiplier tube. The CEM has an energy resolution of $\delta E_T/E_T = \sqrt{(.135/\sqrt{E_T})^2 + (.02)^2}$ where E_T is measured in GeV/c.

Hadrons deposit little energy in the CEM. To measure hadronic showers, the Central Hadronic Calorimeter (CHA) is located behind the CEM, covering the region $|\eta| < 0.9$. The CHA is divided into 528 towers, each of which cover 0.1 units of pseudorapidity and 15° of azimuthal angle. Each tower contains 32 layers of steel and PMMA-based scintillator. The light from the scintillator is wave-shifted and doped with a laser dye, which is read out using a high-gain phototube. The resolution of the CHA is $\delta E_T/E_T = \sqrt{(.75/\sqrt{E_T})^2 + (.03)^2}$ where E_T is measured in GeV/c.

When discussing hadronic calorimeters, the typical length scale is the absorption length. This is the average depth after which a hadron retains only $1/e$ of its original energy. When looking for muons, it is good to have a large number of absorption lengths of material before the muon chambers, so that the only particles which reach the chambers are muons. The CEM and the CHA provide at least 5 absorption lengths at 90° incidence. If the particle is traveling at an angle relative to the radial direction, it will pass through even more material.

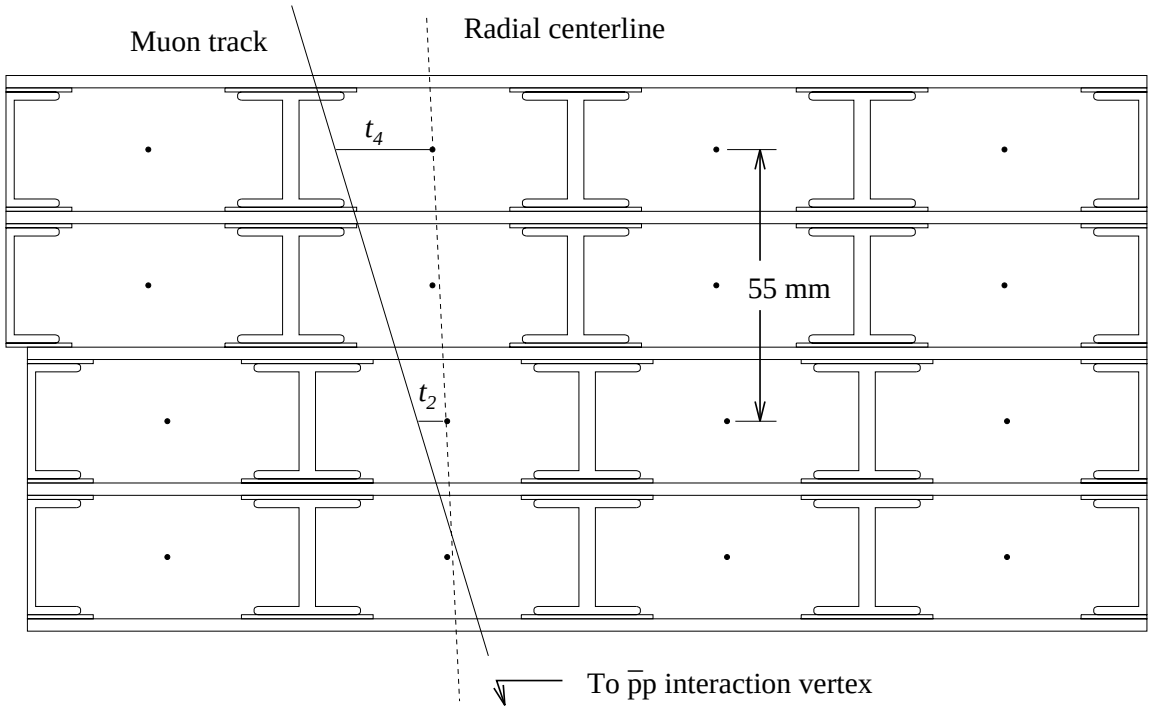

Figure 2-8: One tower of the CMU

2.3.6 Muon Chambers

The Central Muon Chambers (CMU) consist of 48 separate chambers. Half surround the east half of the detector, and half surround the west half. Each wedge covers 12.6° of azimuthal angle, with a gap of 2.4° between each chamber. Each wedge is equally divided into three towers made of four layers, each containing four rectangular drift cells, as shown in Figure 2-8. The cells are operated in limited streamer mode.

Each sense wire is connected to a sense wire in the same layer with one cell in between the two wires at the $\theta = 90°$ end of the chamber. This reduces the electronics needed to read out the chamber, and allows the entire system to be read from one end. Each end of a sense wire is connected to an ADC-TDC card through a 0.1μF capacitor. The TDC measures the time at which the deposited charge arrives on the wire. Charge deposited in the chambers moves with a constant drift velocity, so the time can be converted into a measurement of the position of the charged particle. The ADC measures the amount of charge deposited. The charge is actually divided

between the two ADC's on either end of the wire. Thus, charge division can be used to measure the z location of the particle. The RMS resolution of the chamber is 250 μm in the azimuthal direction, and 1.2mm in the z direction.

Two of the sense wires in alternate layers are on a line which extrapolates to the interaction region. The other two wires are offset by 2mm. The left-right ambiguity inherent in drift chambers is resolved by determining which wires are hit first. Additionally, the chamber is able to provide a rough estimate of the momentum of the particle. Figure 2-9 shows the path of a particle traveling through first a region with a solenoidal field and then a region with no magnetic field. The angle of the particle relative to the radial direction, α, is related to the magnetic deflection angle β by

$$D\sin(\alpha) = L\sin\left(\frac{\beta}{2}\right) \tag{2.7}$$

where L is the radius at which the magnetic field ends, and D is the radius where the muon chambers are located. β is related to the transverse momentum by

$$\sin\left(\frac{\beta}{2}\right) = \frac{eLB}{2P_T} \tag{2.8}$$

where e is the charge of the muon, and B is the magnetic field strength. α can be measured by using either pair of the wires. For small values of α, the difference in drift times for the two wires, Δs, will be

$$\Delta s = H\alpha/v \tag{2.9}$$

where v is the drift velocity, and $H = 55.0$mm is the distance between sense wires. Thus, the transverse momentum of the track is

$$P_T \simeq \frac{eL^2BH}{2Dv\Delta s} \tag{2.10}$$

For the trigger, any chamber with Δs less than a preset value generates a trigger

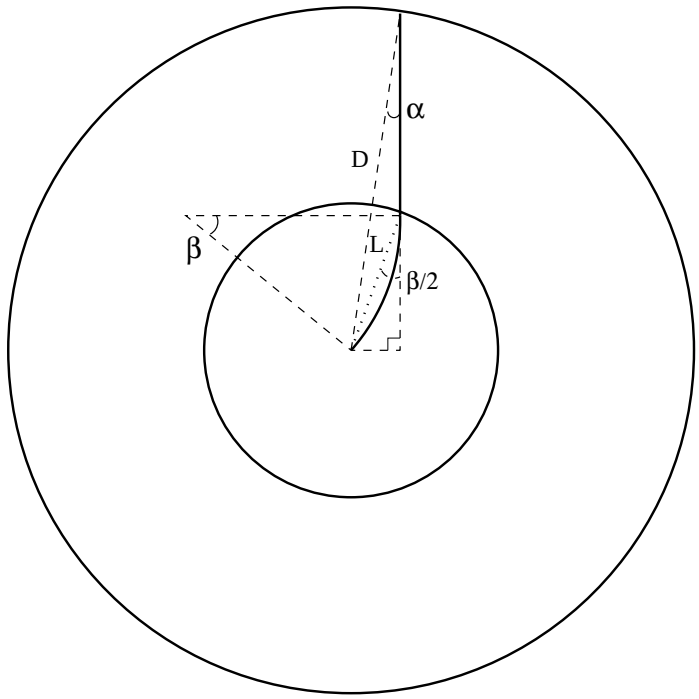

Figure 2-9: Schematic of the path traversed by a muon through the CDF detector.

signal, which corresponds to P_T greater than some minimum threshold.

This measurement is of limited accuracy for two reasons. First, the lever arm used to measure α is fairly short, and α is determined from only two points, so the measurement error will be fairly large. Also, the measurement is performed only after the muon has passed through the central calorimeters, so multiple scattering causes a significant degradation in the accuracy of the measurement.

Reconstruction

Muon reconstruction begins by searching for "stubs" in the muon chambers with 3 or 4 hits, consistent with a straight line. After all the stubs are found, each track in the CTC is extrapolated to the CMU chamber. The CTC track extrapolation errors include the CTC resolution and the effects of multiple scattering. If a track is sufficiently close to the CMU stub, a muon candidate is formed. Using the CMU hit positions and the location of the extrapolated CTC tracks in the $R - \phi$ and $R - z$

planes, two χ^2 are formed for later use in rejecting background.

2.3.7 Beam Beam Counters

The beam beam counters (BBC) are scintillator planes, located 5.8m from the nominal interaction point. They cover the angular region $0.32^\circ < \theta < 4.5^\circ$ ($3.2 < \eta < 5.9$) and the corresponding region on the opposite side of the detector. They provide an accurate measurement of the time of the interaction with a timing resolution which is better than 200 ps. A coincidence in the BBC's is required by the trigger system.

In addition to measuring the time of the interaction, the beam beam counters are also used to measure the luminosity. The rate (number) of coincidences in the east and west BBC's, when divided by the effective BBC cross section, yields the instantaneous (integrated) luminosity. The effective cross section is derived from measurements made at E710[30].

As this is an effective cross section, different experimental conditions between E710 and CDF can change the observed value. The difference in the acceptance between the two experiments has been modeled using Monte Carlo. The effects of using different beam pipes, store to store variations and differing values of instantaneous luminosity have been considered. One run which had only five proton bunches instead of the usual six is used to study the effect of accidental coincidences. After applying all the corrections, the integrated luminosity is known to 3.6%.

2.3.8 Trigger System

The total $p\overline{p}$ cross section at CDF is $\approx$ 75 mb[31, 32], while the cross section for interesting processes is orders of magnitude smaller. In the case of ψ production, the cross section times branching ratio is more than six orders of magnitude smaller than the total cross section. In order to obtain reasonable rates for the processes of interest, an extremely large rate of interactions must be obtained. If every event were to be saved, the resulting data set would be too large to be of practical use. Even worse,

during the time that the approximately 100,000 channels are being read and saved, the detector is unable to record subsequent, possibly more interesting, interactions. It is necessary to implement a real-time system which reduces the data rate to manageable levels by quickly rejecting events without interesting characteristics.

To perform this rejection, CDF implements a three tier trigger system. Each level performs more complex but slower selection algorithms. By employing such a multi-tier system, the amount of deadtime can be minimized while retaining a large fraction of the interesting events. The first level must decide whether or not to accept the event for every crossing, at a rate of about 300 kHz. To avoid large amounts of deadtime, the decision must be completed in less than $3.5\mu s$, when the next crossing occurs. Analog electronics connected to the detector front-end electronics apply simple algorithms to each detector component to determine if the event is accepted, which reduces the rate to 1-2 kHz. Events passing the Level 1 trigger are digitized, and given to the Level 2 trigger. These events incur deadtime, while more complicated algorithms are run in the Level 2 trigger. Correlations between different systems, such as the muon chambers and the tracking system, are considered. The rate out of the Level 2 trigger is 5-15 Hz. The Level 3 trigger is a dedicated farm of Silicon Graphics Power Server computers running FORTRAN algorithms. Events passing Level 2 are consolidated and given to one of the computers. A reduced version of the offline reconstruction is run on the entire event. Level 3 reduces the rate by about a factor of three before the data is written to tape. The reductions eliminate reconstruction of objects that are not used in the trigger, such as very low momentum tracks and SVX information.

In the Level 1 trigger, both muons must be detected in the CMU. The Fastouts in the CMU must register a muon with a slope smaller than a preset value, corresponding to a minimum P_T requirement. Multiple scattering in the calorimeters degrades the resolution for this cut considerably, resulting in a soft turn on. Despite a nominal ~ 3 GeV/c P_T cut, muons with a P_T as low as 1.5 GeV/c will often pass this trigger. Softer muons do not reliably penetrate the calorimeters. The trigger hardware combines neighboring towers with muon stubs into a single muon. Thus, to pass the

dimuon trigger, there must be a tower between the two muons which does not contain a muon stub, or the muons must be in opposite halves of the detector.

The Level 2 trigger requires a Level 1 trigger, and a track pointing to one of the muons. The track is reconstructed using the Central Fast Tracker (CFT). Recall that in the CTC, the wires within a superlayer are laid out at a 45° angle, relative to the radial direction, with cells at different azimuthal angles overlapping. Since high momentum tracks travel almost straight out from the beam line, this means that every high momentum track will pass close to at least one wire in each superlayer. A simple and fast method for reconstructing high P_T tracks is to look for hits in each radial superlayer, which where recorded shortly after the interaction time. These are called "prompt" hits. A high P_T track will appear as a prompt hit in each superlayer, measured at times which correspond to points on a circle. By placing a lower limit on the radius of the circle, tracks with $P_T < P_T(\text{min})$ can be excluded for any desired minimum. In order to resolve the left-right ambiguity and to reduce the background from noise hits, hits are required to be recorded on the neighboring wires as well. As these hits take longer to appear on the wires, they are called "delayed" hits. The CFT allows one delayed hit to be missing, but all the prompt hits must be present. Using this method, high momentum tracks can be efficiently reconstructed with a minimum of background and deadtime.

After the CFT finds a track, the P_T and ϕ of the track are known. A lookup table is then used to determine which regions of the CMU the particle could reach, considering the resolution of the CFT and multiple scattering. This is approximately a five degree matching requirement. If either of the muon chambers containing the Level 1 muon candidate has a CFT track which projects to it, the Level 2 trigger accepts the event. The CFT places a nominal cut at $P_T > 3$ GeV/c, and rapidly becomes inefficient for softer tracks. The Level 2 trigger efficiency plateaus at 94% for $P_T > 3.5$ GeV/c, but is only 50% efficient by $P_T = 2.6$ GeV/c.

For the third level of the trigger, the full CTC track reconstruction is done, in addition to the standard muon reconstruction. Each CTC track is extrapolated to

the muon chambers. If the extrapolation matches a muon stub, a muon candidate is created. Uncertainties in the extrapolation are calculated, considering both the CTC resolution, and multiple scattering through the calorimeters. The position and the slope of the extrapolation is compared with that of the CMU stub in the $R-\phi$ and $R-z$ views. All four quantities must individually agree by better than 4σ, where σ is the uncertainty in CTC track extrapolation, considering both the detector resolution and the multiple scattering effects. (For early runs, this requirement was 6σ, but it was reduced after seeing that the system was stable, and that a 4σ cut is highly efficient.) All events with two muons whose invariant mass is close to the J/ψ mass are kept. During the run, several triggers where used to select $\psi(2S)$ candidates, some of which imposed P_T cuts on the muons. Those triggers are not used in this analysis.

2.3.9 Data Acquisition

Each detector component is connected to a FASTBUS network[33]. The calorimeter and muon drift chambers are connected to RABBIT cards[34] for readout by MX scanners. The tracking system is read out by SLAC Scanner Processors (SSP)[35], which reorganize the data into a rudimentary format. Each scanner is capable of holding four events at a time. This level of the Data Acquisition (DAQ) pipeline is managed by the Trigger Supervisor (TS). The TS combines FASTBUS messages with dedicated control lines to effect efficient use of the front end system.

When the entire event has been loaded from the detector, the TS sends a FASTBUS message to the Buffer Manager (BFM) indicating that the event is ready. The BFM manages the flow of data from the scanner modules to the CPU farm which constitute the Level 3 trigger. After being notified of a new event, the BFM instructs a hardware Event Builder (EVB) to "pull" the event. The EVB is a set of FASTBUS modules which read and format events. When the EVB finishes pulling the event, it notifies the BFM which sends a message to the TS, which in turn notifies the scanners that the buffer is now available to accept a new event. The BFM then instructs

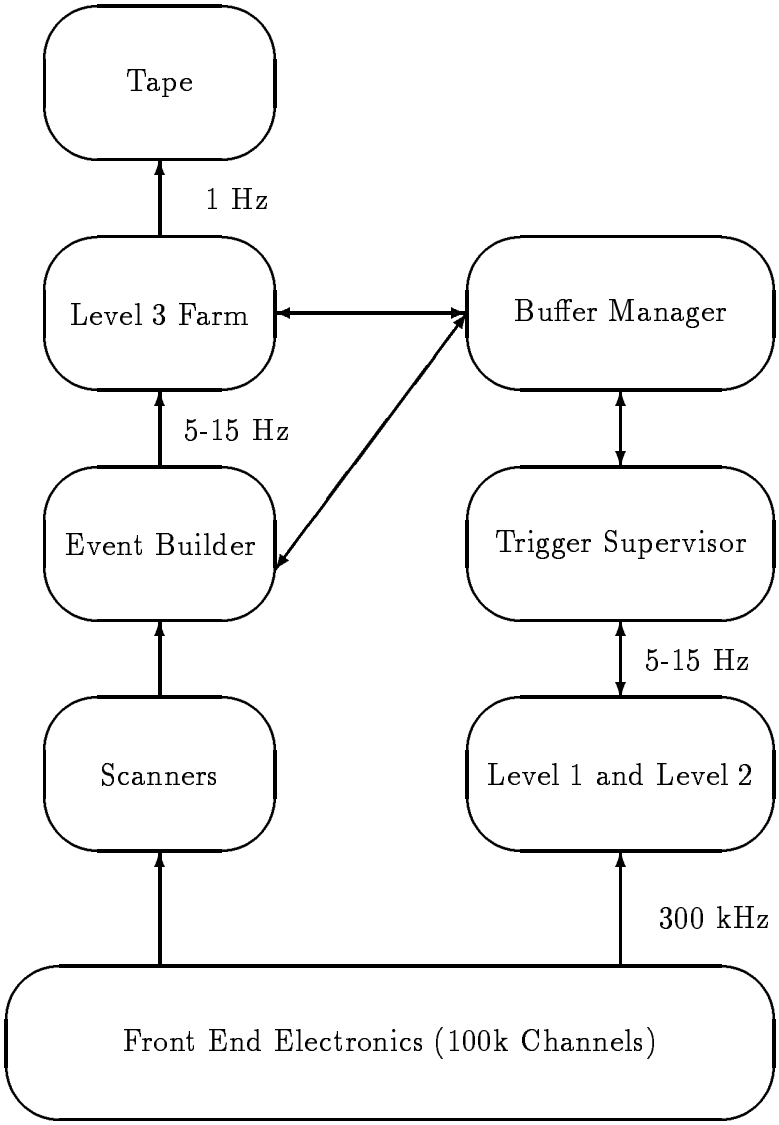

Figure 2-10: Schematic diagram of flow in the CDF data acquisition and trigger systems in the 1992-1993 run.

the EVB that the event should be sent to a specific Level 3 node. Those events passing the Level 3 trigger are written to magnetic tape for further offline analysis. The process is shown in Figure 2-10. A subset of the events would also be passed to several "consumers." These are programs which performed online monitoring of the experiment, and provided an early warning if some component had failed.

For the 1993-1995 run, the data acquisition system was upgraded in order to handle the higher event rates and to increase the reliability of the system. FASTBUS Readout Controllers (FRC's) were installed in every FASTBUS crate to read out the front end electronics. Using a Scanner Bus developed at Fermilab, each FRC is connected to a Scanner CPU (SCPU), a VME module with a 68030 microprocessor. The six SCPU are coordinated by the Scanner Manager (SM). Each SCPU opens a permanent connection with each of the Level 3 Receivers, which act as intelligent buffers, receiving event fragments from the SCPU and forming them into one event for the Level 3 trigger.

During data taking, once the Level 2 trigger accepts an event, the Trigger Supervisor instructs the FRC's to load the event. When an FRC finishes loading an event it notifies the Trigger Supervisor. After all the FRC's finish, the Trigger Supervisor notifies the Trigger Supervisor Interface (TSI), which is an FRC in the Trigger Supervisor crate. The TSI notifies the SM of the event, and the SM broadcasts a Load Event request to the SCPU over the SCRAMNet reflective memory network. After a SCPU has received data from all the FRC's connected to it, it sends a Load Event acknowledgment to the SM. After all the SCPU are finished loading the event, the SM notifies the TSI, which informs the Trigger Supervisor, causing the Trigger Supervisor to free the front end buffers so that another event can be loaded. Additionally, the SM finds an available Receiver, and issues a Send Event command the the SCPU. Each SCPU transmits its event fragment to the Receiver over the ULTRANet network. After the transmission is finished, the SCPU returns a Send Event acknowledgment to the SM. The SM notifies the Receiver when the event is complete. After the Receiver has the data from all of the SCPU's, the event is given

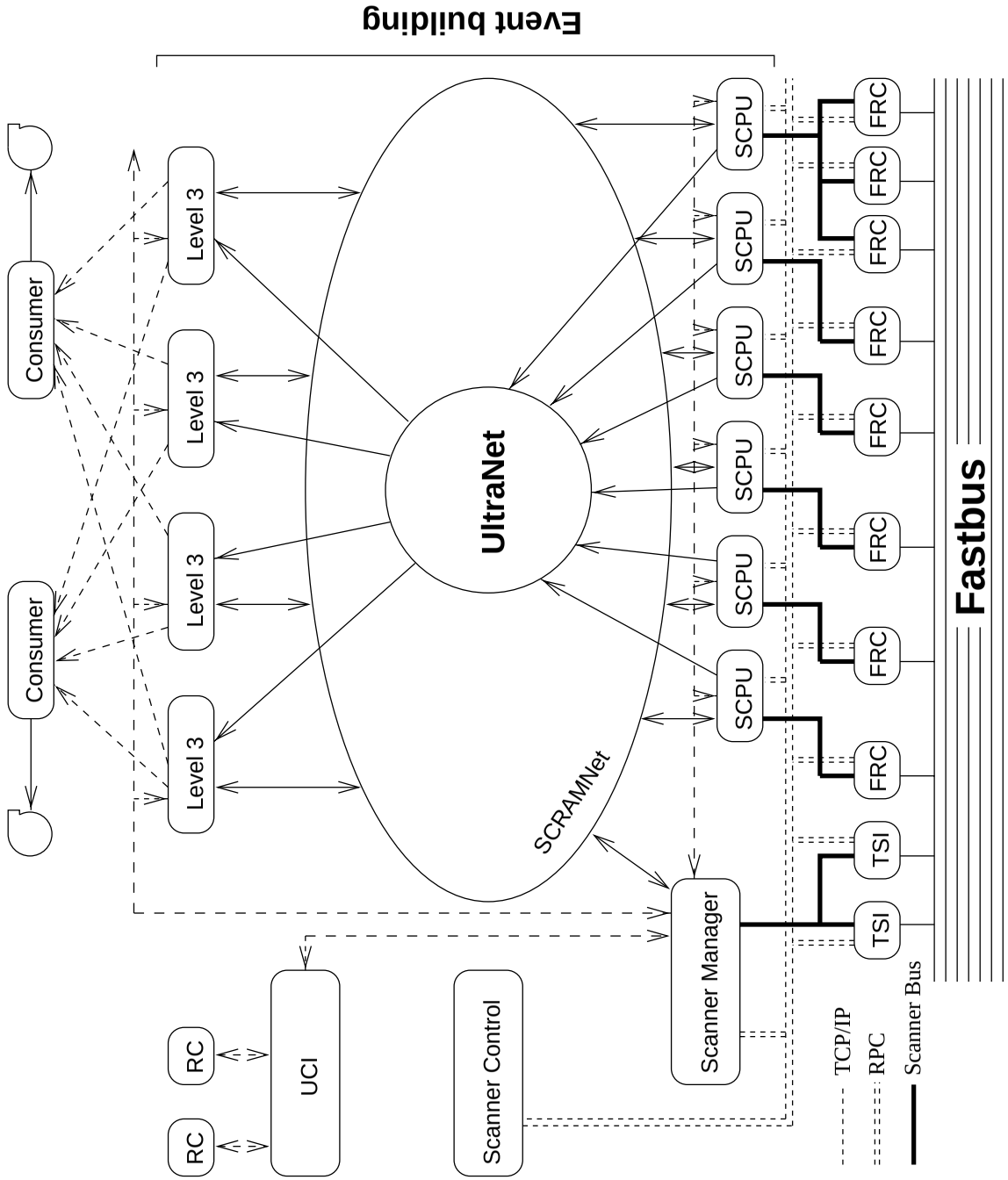

Figure 2-11: Data acquisition system in the 1993-1995 run.

to the Event Builder(EB) running on that node. The EB formats the event, and passes it to the Level 3 trigger software. Events passing the Level 3 trigger are passed to the Consumer Server (CS) via ULTRANet. The CS then passed events to the Consumers using either ULTRANet or Ethernet. In this run, one of the consumers is the Data Logger, which writes accepted events to disk. Events are written to disk because Level 3 accepted events faster than it is possible to write the events to tape. To alleviate this problem, accepted events are written to staging disks. When enough data to fill a tape is on disk, a daemon copies the files onto tape and delete them from the disk.

Chapter 3

Inclusive ψ Cross Section

3.1 Event Selection

The events used in this analysis are selected from a trigger which requires two muon candidates in the CMU. Even with no other requirements, a clear J/ψ peak is visible in the dimuon mass distribution. However, additional requirements can improve the signal in addition to simplifying the measurement. In considering selection criteria, several factors must be considered. To measure the cross section, it must be possible to measure the efficiency on the signal. In fact, some of the requirements imposed are necessary to measure the cross section. Additionally, it is desirable to avoid introducing biases against a particular production mechanism, for, even if the bias can be determined, it complicates the measurement and introduces additional systematic uncertainties.

3.1.1 Basic Requirements

One requirement which must be imposed on the data for a reliable cross section measurement is that the muons which form the ψ candidate pass the dimuon trigger. While additional events could be added to the sample by removing this requirement, without a direct trigger path, it is difficult to understand the trigger efficiency.

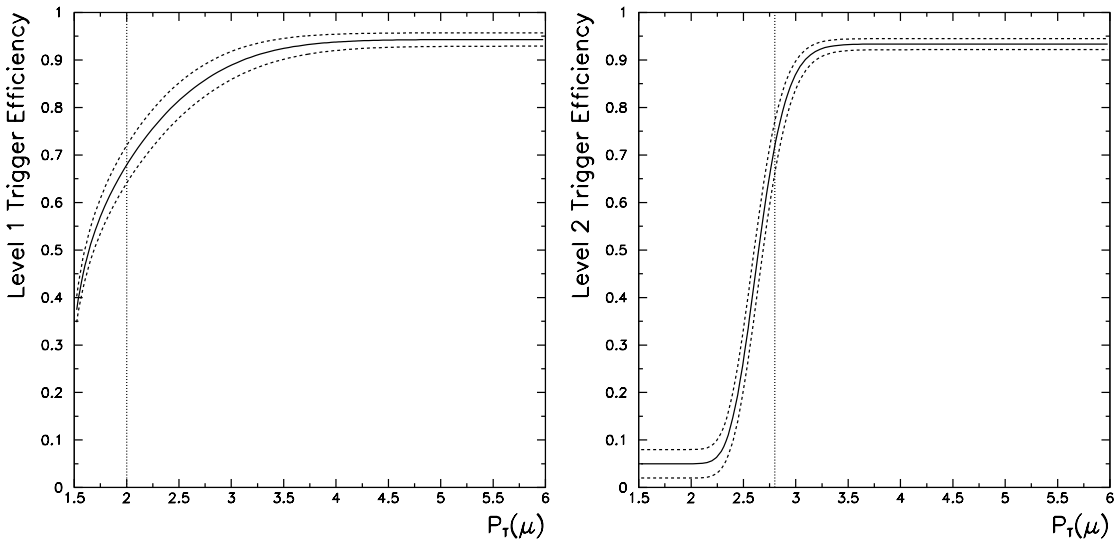

Figure 3-1: Efficiencies of the Level 1 and Level 2 muon triggers, as a function of muon P_T. The solid line is the central values, and the dashed lines indicate the uncertainties. The vertical dotted line shows minimum P_T accepted in this analysis for the soft (left) and hard (right) muons.

A low threshold for the muon P_T will certainly increase the number of events. This, however, must be balanced against the decreasing trigger efficiency and the increasing relative uncertainty in that efficiency. The Level 1 trigger has a slow turn on below its nominal 3.3 GeV/c requirement[36], as shown in Figure 3-1. The measurement of these efficiencies is described in Section 3.1.3. The plateau efficiency is 94% for $P_T > 4$ GeV/c. The trigger is 68% efficient for P_T=2 GeV/c and is still 34% efficient at a P_T of 1.5 GeV/c, below which the muons no longer penetrate the calorimeter. However, the trigger efficiency becomes more poorly measured as one moves to lower momentum. In order to limit the systematic uncertainties, both muons are required to have transverse momentum larger than 2.0 GeV/c.

The Level 2 trigger has a much faster turn-on. Only one muon is required to match with a track found by the CFT, so only the high-P_T muon is required to be in the region where the CFT is efficient. This is implemented by requiring one muon to have $P_T > 2.8$ GeV/c, where the Level 2 trigger is approximately 70% efficient, as

seen in Figure 3-1.

The detector has little acceptance for ψ with $|\eta(\psi)| > 0.6$, so the dimuon is required to have $|\eta(\mu^+\mu^-)| < 0.6$, where $\eta(\mu^+\mu^-)$ is the pseudo-rapidity of the dimuon. The kinematic requirements reject events with a low P_T of the ψ, so, in order to remain in the region where the kinematic acceptance is understood, we impose the requirement $P_T(\mu^+\mu^-) > 5$ GeV/c, where $P_T(\mu^+\mu^-)$ is the dimuon transverse momentum. To reduce the systematic uncertainty on the J/ψ cross section, which has a small statistical uncertainty, about 4 pb^{-1} of data for which the CTC was not correctly calibrated is not used. This data is included in the $\psi(2S)$ analysis, as that analysis has far fewer events, and an appropriate correction is applied to the efficiency. This correction is calculated from the data by measuring the decrease in the J/ψ rate during these runs.

While some of the previous requirements decrease the background level, that is not their main purpose. They are necessary for the events to be in a region where the efficiency of the detector is well understood. Additional requirements are applied for the purpose of reducing the background. Before describing these requirements, the backgrounds that need to be suppressed are described.

3.1.2 Background Contributions

One major source of background is "punch-through," which is usually divided into two types. "Non-interactive" (or "sail-through") punch-through occurs when a charged hadron, typically a kaon or a pion, travels through the entire calorimeter without initiating a hadronic shower. Averaged over the different species, there is a 0.5% probability of a hadron penetrating the calorimeters without initiating a shower.[37, 38] Since that is the specific property of muons which the muon system exploits to identify muons, these particles are misidentified as muons. Beyond increasing the shielding in front of the muon chambers, there is little that can be done to reject this type of background.

"Interactive" punch-through occurs when a particle enters the calorimeter and

initiates a shower, but the shower is not fully contained by the hadronic calorimeter and one or more charged particles exit the calorimeter. If one of these particles leaves a stub in the muon chamber which is consistent with a track reconstructed in the CTC, then a muon candidate is formed. Since these particles are generally traveling at an angle relative to the particle that initiated the shower, the match of the muon stub with the extrapolated CTC track is often much worse than for a real muon.

Another source of background is "decay-in-flight" muons. These are muons produced by the decays $\pi^+, K^+ \rightarrow \mu^+ \nu_\mu$. The differences between decay-in-flight and ψ muons depend on where the decay occurred. If the parent particle has already exited the CTC, the muon direction will be displaced from the direction of the CTC track. This will result in a poorer match between the CMU stub and the CTC track extrapolation. If the parent particle decays inside the CTC, the outcome will be dependent on the CTC reconstruction. It may reconstruct the pre-decay portion, the post-decay portion of the track or a combination of the two. In the first case, again, the CMU-CTC matching will suffer, and in the second case, the CMU-CTC matching will be normal. However, there may be difficulties in attempting to extrapolate the track to the production vertex. If the kink caused by the decay is not too dramatic, both the parent and daughter track segments may be fit to a single track, giving rise to the third case. Here the CMU-CTC matching may suffer a significant distortion. When the parent particle decays before reaching the CTC, the situation is similar to when the post-decay track is reconstructed, although there is less difficulty in extrapolating the track to the production vertex. Since the kink is closer to the production vertex, the error incurred by extrapolating along the trajectory, assuming that there is no kink, accumulates over a shorter distance than when the decay occurs in the CTC. In all cases, the magnitude of any extrapolation discrepancies will depend upon the parent P_T; higher P_T decays will produce smaller kinks and smaller discrepancies.

The final background is heavy flavor decays. Opposite sign muon pairs can be produced by $b\bar{b}$ or $c\bar{c}$ production, when both heavy quarks decay semileptonically by $b\bar{b} \rightarrow c\bar{c}\mu^+\mu^- X$ or $c\bar{c} \rightarrow s\bar{s}\mu^-\mu^+ X$ or by the sequential decay $b \rightarrow c\mu^+\nu_\mu$ followed by

$P_T(\mu^{\pm}) > 2.0$ GeV/c
$\max(P_T(\mu^+), P_T(\mu^-)) > 2.8$ GeV/c
$P_T(\mu^+\mu^-) > 5$ GeV/c
$\lvert\eta(\mu^+\mu^-)\rvert < 0.6$
Muons passed trigger
$\chi^2_{\mathrm{FIT}} < 10$
$\chi^2_{\mathrm{CMU,R-\phi}} < 9$
$\chi^2_{\mathrm{CMU,R-z}} < 9$
$\lvert\Delta z\rvert < 5$ cm
$\lvert z\rvert < 60$ cm
Hadronic Energy in calorimeter
Muon ADC information

Table 3.1: Event selection criteria

$c \to s\mu^-\overline{\nu}_\mu$. Whereas most of the other backgrounds do not contain muons, the muon candidates produced by these decays are real muons. The only differences with ψ events are that the mass does not peak sharply, and the muons do not originate from a common vertex.

3.1.3 Background Suppression

Several of the backgrounds mentioned above create muon candidates for which the matching between the CMU stub and the CTC track is not as good as in the case of muons from ψ decays. To reduce these backgrounds, the matching requirement is tightened to be less than 3σ in both the $R-\phi$ and $R-z$ views, where σ is the error on the the CTC track extrapolation from the multiple scattering in the calorimeters.

If a muon track is associated with three or four hits in the SVX, then the SVX information is used to improve the track measurement. Otherwise, only the CTC information is used. It is possible to improve the quality of the sample by placing tighter requirements on the SVX. However, these requirements reject a larger fraction of non-isolated muons. ψ events that result from direct production, or radiative χ_c decays, are expected to be accompanied by only a few particles from the fragmentation process. For B events, in addition to the fragmentation particles, there will

also be the other B daughters, which will make these events less isolated. This will clearly introduce a bias. As this bias can only be measured by removing the biased requirements, applying these requirements does not improve the measurement.

Since we are looking for muons that came from the decay of a single particle, the tracks are required to be separated by less than 5 cm in the z-direction at their points of closest approach to the center of the detector. The distribution of the z differences has an RMS of 1.2 cm, so this requirement is highly efficient. In order that the muons remain in the central portion of the detector, the muons are also required to have $|z| < 60$ cm.

Each muon chamber covers one calorimetry tower, and the muon will deposit minimum ionizing energy in that tower, so we require energy deposition above the pedestal level in the calorimeter. As other particles may also deposit energy in the same tower, it is not required that the energy be consistent with a minimum ionizing particle, as such a requirement would create a bias against events from B decays. A bias could originate in events where the energy deposition fluctuates below the calorimeter threshold. From the efficiency of this requirement, listed in Table 3.4, this occurs 0.1% of the time or less, too infrequently to cause a significant effect. There is also a class of events in which the charge deposited in the muon chambers is below the threshold for the ADC readout. Background rates are much higher in these events, so they are removed from the sample.

If an event has more than two muon candidates surviving these requirements, all oppositely charged pairs are considered. While this creates a combinatoric background, less than 3×10^{-4} of the events contain more than two candidates. At this level, the additional background is too small to be of concern.

The tracks are fitted to a common vertex, and the χ^2 of this one degree-of-freedom fit is required to be less than 10. There are several advantages in imposing this constraint. The mass calculated using the vertex constrained momenta is more accurate than the unconstrained mass, so there is less background under the mass peak. Also, some of the background sources yield tracks which don't extrapolate to a common

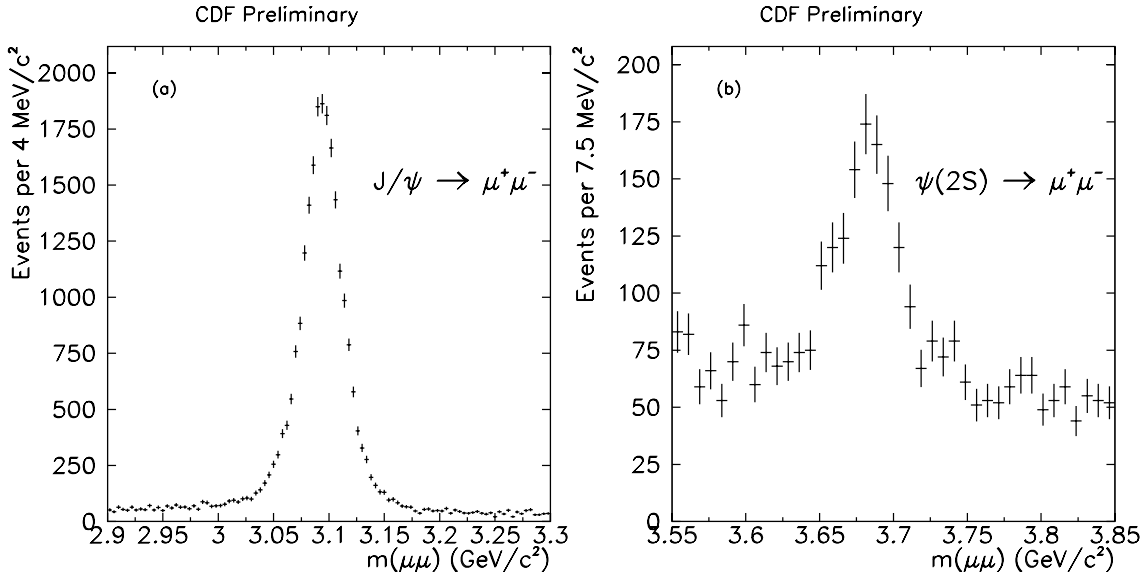

Figure 3-2: Mass distribution of the J/ψ(a) and $\psi(2S)$(b) candidates, after all requirements have been applied.

vertex. Requiring the two tracks to be consistent with a common vertex reduces these backgrounds.

The invariant mass distributions, calculated from the constrained momenta, are shown in Figure 3-2. There are 22120 ± 161 J/ψ events above the background in 15.4 ± 0.6 pb^{-1} and 808 ± 46 $\psi(2S)$ events in 17.8 ± 0.6 pb^{-1}.

Trigger Efficiency

While the trigger system is extremely useful in eliminating unwanted events, it also rejects some of the signal. Thus, the efficiency of the three triggers needs to be evaluated. The efficiency of the Level 1 trigger is determined using events that passed a Level 1 single muon trigger, and which contain a second muon. The second muon represents an unbiased sample for measuring the Level 1 trigger efficiency. The number of muons which passed or failed the trigger is determined by counting the number of events in the J/ψ peak, and subtracting the background using the sidebands. The

efficiency is then

$$\epsilon = \frac{N(\text{Pass})}{N(\text{Pass}) + N(\text{Fail})} \tag{3.1}$$

and is measured as a function of $P_T(\mu)$. As the Level 2 dimuon trigger only required one muon to be matched with a CFT track, the other leg could be used to study the efficiency of that trigger, which greatly increased the available statistics. The efficiency is calculated using the same method with the Level 1.

In order to smooth out the statistical fluctuations in the various P_T bins, the measured efficiencies are fit to a functional model. For the Level 1 efficiency, the function is the difference of two error functions, multiplied by the asymptotic efficiency. The width is dependent on the P_T of the muon, as this affects how much multiple scattering the muon undergoes. The second error function represents the loss in efficiency when the muon is deflected so much that the slope in the muon chamber changes sign, and exceeds the maximum valued allowed by the trigger. This is a 2% effect for a 2 GeV/c muon, and becomes less important at higher momentum. The Level 2 shape is a step function convoluted with a Gaussian resolution function with a constant width, plus a constant fake background rate. The background arises from muons which should have failed the trigger, but which passed because of noise hits or hits from nearby tracks formed a CFT track.[36] These parameterizations allow the probability that any given event will pass the trigger to be calculated.

Systematic uncertainties on the trigger efficiency are estimated by varying the fitting procedure, and by dividing the data into subsamples which may have different characteristics, and fitting each sample separately. The uncertainty on the Level 1 trigger efficiency is largest at small P_T, and causes an uncertainty of 6.4%(6.1%) in the integrated J/ψ ($\psi(2S)$) cross sections. The uncertainty is in the Level 2 trigger efficiency is also largest at small P_T. There is a 1.1%(1.0%) uncertainty in the integrated $J/\psi(\psi(2S))$ cross section from the Level 2 trigger efficiency. The trigger efficiencies are shown in Figure 3-1.

The efficiency of the Level 3 trigger is measured in two ways. The first method involves hand scanning data from two runs where the Level 3 trigger was run in

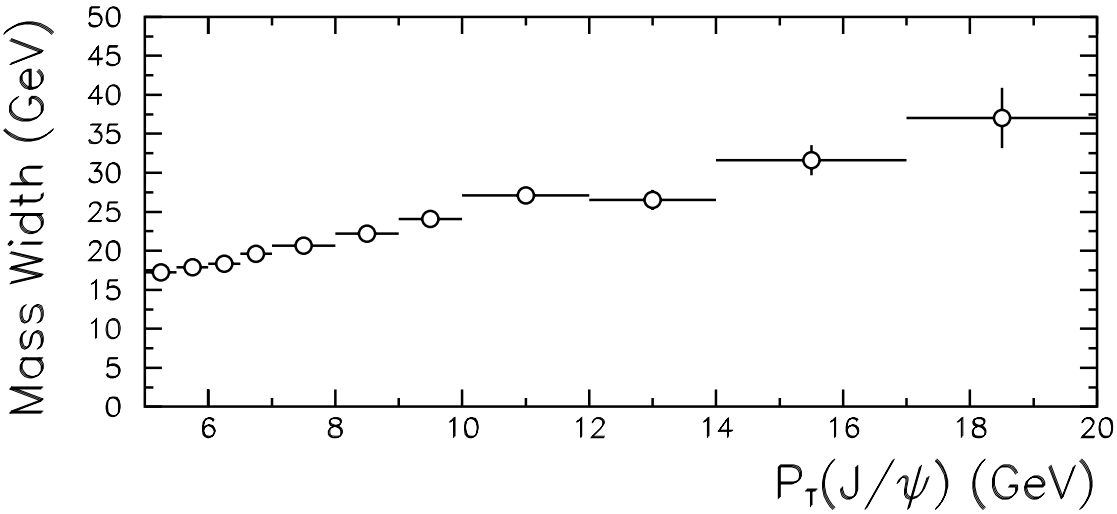

Figure 3-3: Width of the J/ψ mass peak as a function of ψ P_T. The width varies by a factor of two over the range of interest. These values are meant to be used only as an estimate, since the fits used to derive them are of low quality.

tagging mode. After selecting events which passed the Level 2 trigger, it is determined whether or not the CFT track is a real track, or a fake track. Tracks with large impact parameters are rejected, along with tracks from satellite-satellite interactions or tracks which were not found by the offline reconstruction program. After this, the tracking efficiency is the ratio of the number of tracks found by the Level 3 trigger to the number of real tracks found by the CFT.

Since hand scanning is somewhat subjective, the efficiency is cross checked, using data from near the beginning of the collider run. At this time, the Level 3 trigger was run in tagging mode while it was being validated. From this sample, dimuon events are selected, and divided into two samples, based on whether they passed or failed the Level 3 trigger. The dimuon mass is reconstructed, and the mass distributions are fit for the number of events in the J/ψ peaks. This yields an efficiency of $97 \pm 2\%$.[39]

3.2 Mass Fit

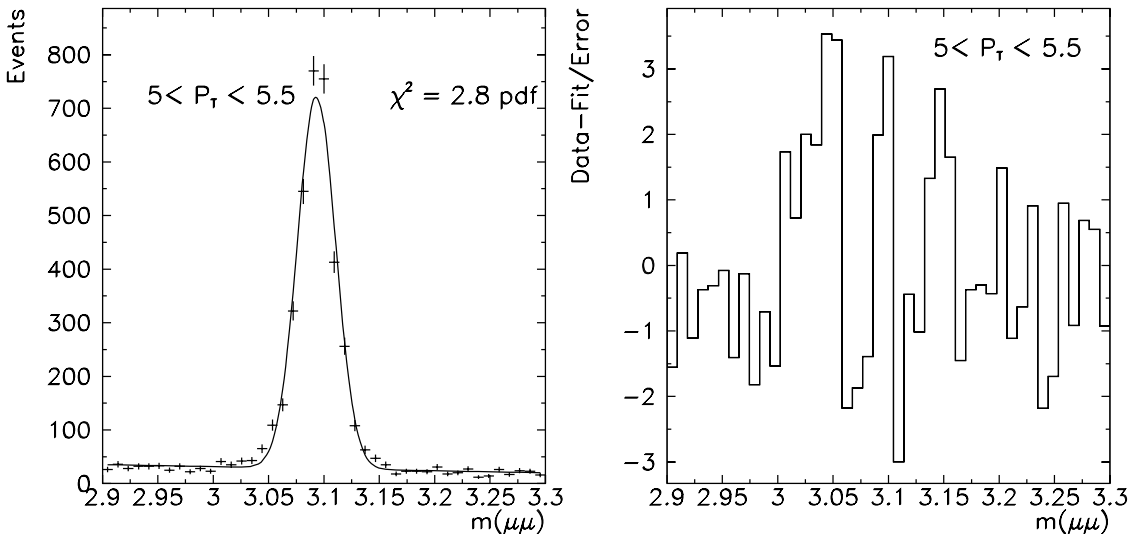

Figure 3-4: Mass and pull (Data - Fit / Error) distribution of the J/ψ candidates with $5 < P_T(\mu^+\mu^-) < 5.5$ GeV/c. Overlaid is a fit to a Gaussian plus a linear background. The fit is clearly too low in the center of the peak and the tails, while it is too high in the sides of the peak.

The number of ψ events is determined by fitting the mass distribution. As the muon P_T resolution is a function of P_T, fitting the full data sample to a single Gaussian yields a poor fit. The width of the mass distribution is shown in Figure 3-3 as a function of $P_T(J/\psi)$, obtained by fitting the mass distribution to a Gaussian plus a linear background. Although the fits are poor, it still shows that the width is increasing with the ψ transverse momentum, demonstrating that the signal shape must be a function of $P_T(\psi)$. Restricting the ψ candidate to a small P_T range alleviates this problem. However, even then the muons have a range of momenta, and the mass peak is still not well described by a Gaussian, as can be seen from Figure 3-4. In addition, the low-side tails are larger than the high-side tails, indicative of radiative decays.

In order to account for the P_T-dependence of the resolution, a mass template is derived from Monte Carlo. ψ events are generated with a flat distribution in P_T, η and ϕ using the ψ generator described in Section 5.1. The ψ is then decayed to

either $\mu^+\mu^-$ or $\mu^+\mu^-\gamma$, using a next-to-leading order QED calculation. In order to simulate the trigger requirement, the muon trajectories are required to extrapolate to the fiducial CMU volume. The event is rejected if either muon does not project into the CMU chambers, or if there is not an empty chamber between the two muons when they are on the same side of detector. The momentum of each muon is smeared (as described below) to simulate the detector resolution. The smeared momenta are required to pass the kinematic cuts of Section 3.1 and are used to calculate the invariant mass and P_T of the muon pair. For events passing these criteria, the smeared mass is put into a histogram corresponding to that P_T. Each Monte Carlo event is assigned a weight proportional to a combination of the predicted cross sections from B production and the Color Singlet Model, where the predictions have been rescaled so that the integrated B production cross section is 20% of the integrated combined cross section. This fraction is used because about 20% of both the J/ψ and $\psi(2S)$ samples originate from B decays. The weight is multiplied by the probability of that event to pass the trigger. This yields the mass templates used to fit the mass distributions.

The tracking resolution is better for tracks which have SVX information, so three mass templates are generated for each P_T region, corresponding to the three possible permutations of tracks with and without SVX information. These three templates are added together, fixing the ratio of the total area under each to the ratio of the number of all the dimuon candidates in the data for each category. A binned likelihood fit is used to fit the data to this template plus a linear background to determine the number of events. Despite fitting the mass distribution in a region which covers ≈ 200 MeV/c^2 on either side of the ψ mass, the radiative decays cause about 1% of the ψ events to have a dimuon mass smaller than the lower boundary, as can be seen in Figure 3-7. The fitted number of events is corrected for events which fall outside the mass window used in the fit.

One possible systematic error is that the number of events returned by the fit could depend on the relative fractions of the three templates used in the fit. To investigate this dependence, several alternative approaches are employed to calculate

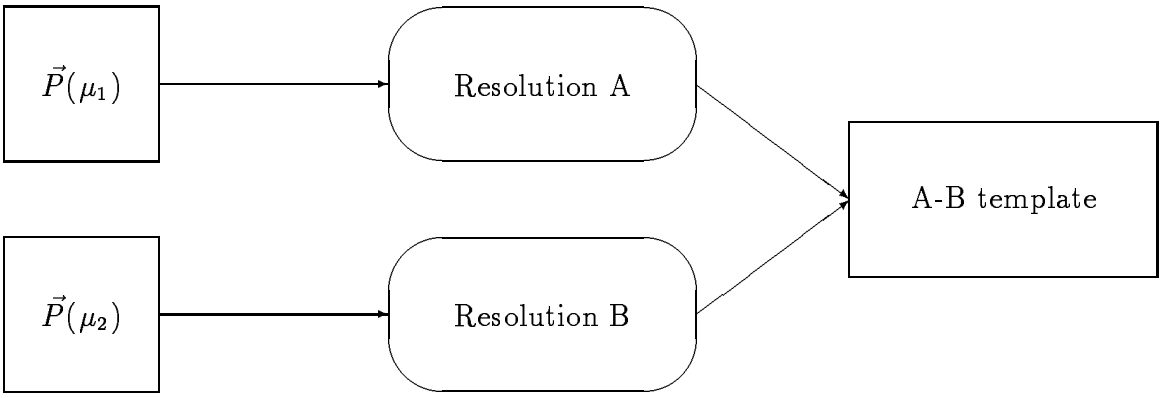

Figure 3-5: Schematic diagram of the mass template creation process. The momentum of each muon is smeared by the resolutions, and used to calculate the mass for the template. This procedure is performed four times, with A and B being all possible combinations of SVX and CTC. The SVX-CTC and CTC-SVX templates are added to form one template.

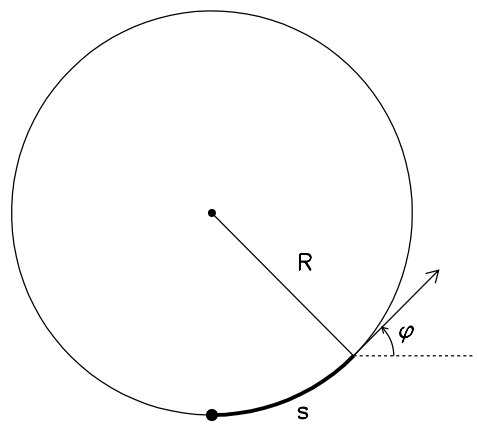

Figure 3-6: The definition of curvature is the change in direction per unit arc length, $C \equiv \left|\frac{d\varphi}{ds}\right|$. For a circle, $C = \frac{1}{R}$.

these fractions. One procedure is to measure the number of events with each SVX classification in three separate fits. In each P_T bin, three fits are performed using only the events with a specific number of SVX tracks, and the corresponding mass template. The number of events from each fit is converted into the fraction of the signal for that template, and the full sample is refit using that fraction. Additionally, the mass distributions are refit after raising or lowering each fraction by one statistical sigma, yielding eight new estimates of the number of events. In all cases, the variations are negligible when compared to the statistical uncertainty.

3.2.1 Resolution determination

The mass templates are not constructed using the standard CDF detector simulation ("QFL"). While QFL reproduces many of the aspects of the data, it produces a better mass resolution than is observed in the data. Since the mass resolution is exactly the aspect of the simulation which needs to be done correctly, this is not a satisfactory situation. Also, since we will need to tune the detector simulation so that

it reproduces the data, a fast simulator is needed, in order that the large Monte Carlo sample can be simulated many times. This eliminates the possibility of using a "first principles" simulation which models the detector by generating hits within the detector, followed by running the standard offline reconstruction on the resulting data, which would be unacceptable slow. For these reasons, we use a simple model of the detector, with a few parameters that allow us to tune the model until it reproduces the data.

The detector measures the change in the track direction per arc length, known as the curvature and shown in Figure 3-6. The curvature resolution, σ_C, is independent of the particle momentum and is the first parameter in our model. The curvature is proportional to $1/P_T$, and $1/P_T$ of each muon is smeared by a Gaussian of width σ_C. The resolution of ϕ and $\cot\theta$, which determine the track direction, are also approximately constant. The second parameter is σ_θ, which is the width of the Gaussian used to smear $\cot\theta$. ϕ should also be smeared by σ_ϕ, except that the ϕ resolution is dominated by multiple Coulomb scattering. The mean scattering angle for a particle undergoing multiple scattering is approximately Gaussian distributed, with the width having a $1/P$ dependence[40, 41, 42]. To simulate this, we take the three track angles, $\vartheta_{x,y,z}$, where $\cos\vartheta_i \equiv \frac{P_i}{P}$, [1] and smear each angle independently by a Gaussian of width $\sigma_{\rm MS}/P$. $\sigma_{\rm MS}$ is the third and final parameter in the detector model.

There is one additional factor affecting the resolution— whether or not the track has SVX information. Each of the three parameters are determined twice, once for tracks with SVX fits, and once for tracks that only use CTC information.

From previous studies, approximate values of these parameters are known.[43] For each parameter, five equidistant values are chosen, centered around the expected values. Mass templates are generated as explained earlier using all possible combinations of the parameters, yielding 125 different resolution parameterizations for both the SVX and CTC cases. In a P_T range with high statistics, the data mass

[1] ϑ_z is identical to the θ used in the rest of this thesis.

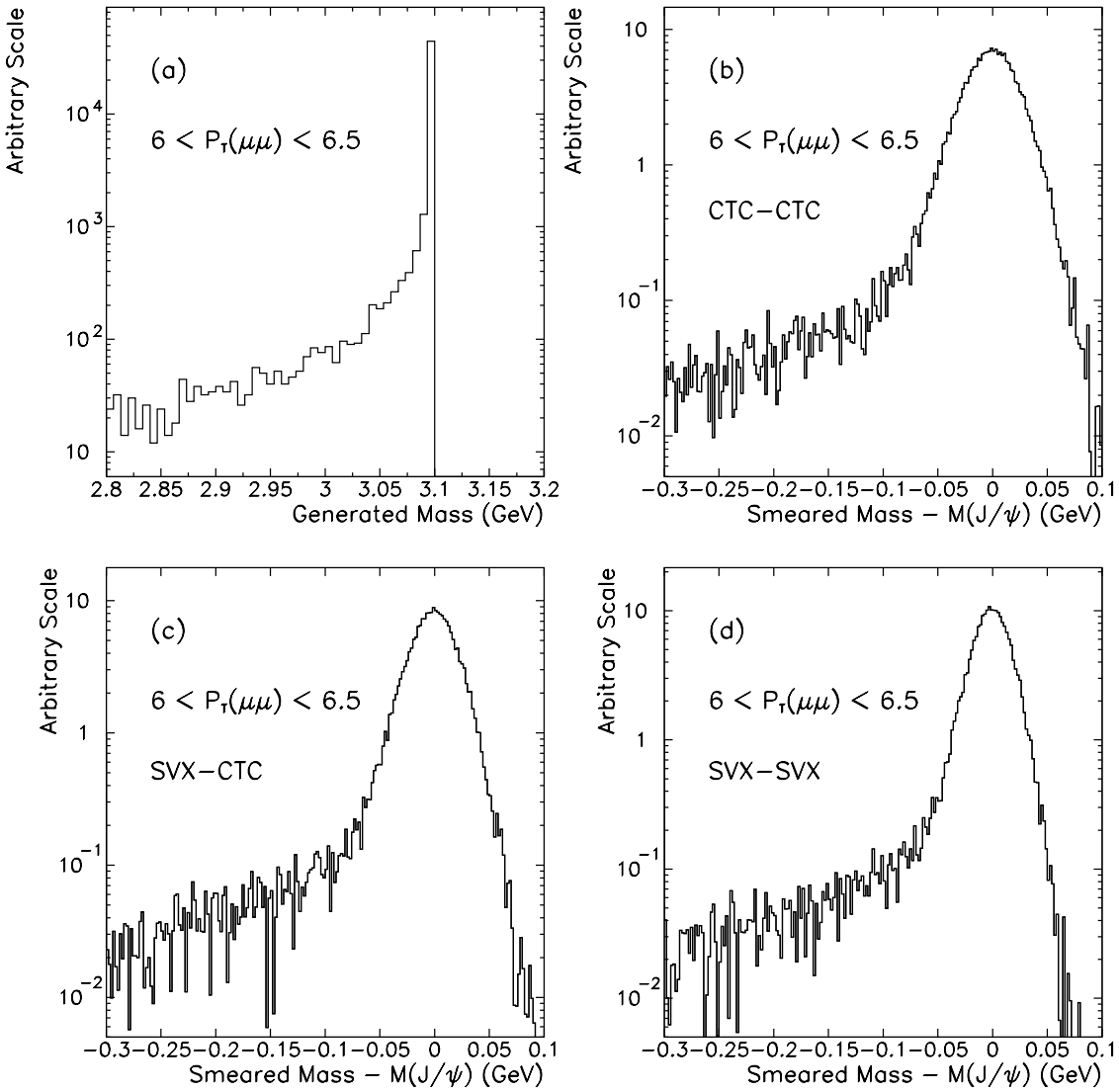

Figure 3-7: The (a) generated dimuon mass distribution and the mass templates for $6 < P_T(\mu^+\mu^-) < 6.5$ GeV/c after being smeared by the fast detector simulator. The templates are for (b) both muons in the CTC, (c) both muons in the SVX and (d) exactly one muon in the SVX. The radiative tail is clearly visible in all the distributions.

distributions in 0.5 GeV/c P_T bins are fit to each of the mass templates plus a linear background. For a given parameterization, we define the total χ^2 to be

$$\chi^2_{\text{tot}} = \sum_i \chi^2_i \tag{3.2}$$

χ^2_i is the chi square from the fit in the ith P_T bin, and the sum runs over all the P_T bins. The parameterization that generates the smallest χ^2_{tot} is chosen to describe the resolution. However, if one of the parameters is at an extreme value, the range of values for that parameter is recentered on that value. New mass templates are generated, and the fits are repeated. This process is iterated until the parameters are stable. The number of events does not change appreciably if the parameters are replaced with any of the six best sets of parameters. Figure 3-8, Figure 3-9 and Figure 3-10 show the results of the mass fits.

3.2.2 Quality of Mass Fits

While it is clear from Figure 3-11 that the radiative fit describes both the center of the mass peak and the tails better than a single Gaussian, it is necessary the ascertain that each fit yields an accurate description of the data, so the quality of the mass fits is checked in several ways. The data is plotted with the fit overlaid and visually checked to be certain that the fit is reasonable. This is also done using (Data-Fit)/Error for each fit. This has the advantage that these values should have a mean of zero with a spread of one, regardless of the number of events in each bin. Each fit is also checked to ascertain that the χ^2 is reasonable.

As these provide fairly subjective tests, a toy Monte Carlo was written to provide additional checks.[2] The result of each fit is used to generate 100 Monte Carlo samples. The number of signal and background events in each sample is chosen from Poisson distributions, where the means of these distributions are given by the number of signal and background events extracted from the data mass fits. Each event is assigned a

[2]See Appendix A for a more detailed description the toy Monte Carlo.

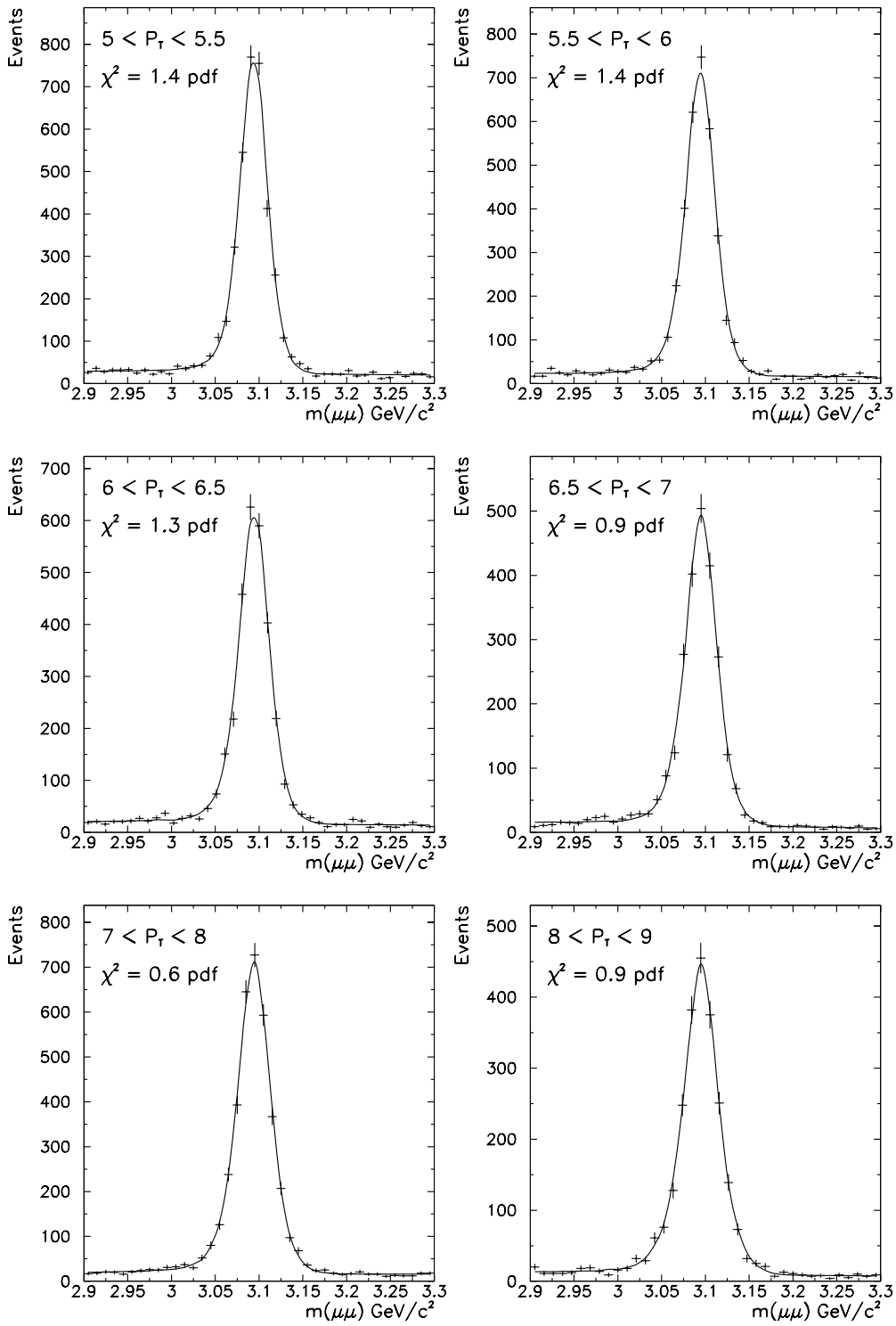

Figure 3-8: J/ψ mass distributions at low P_T, with radiative fit results overlaid.

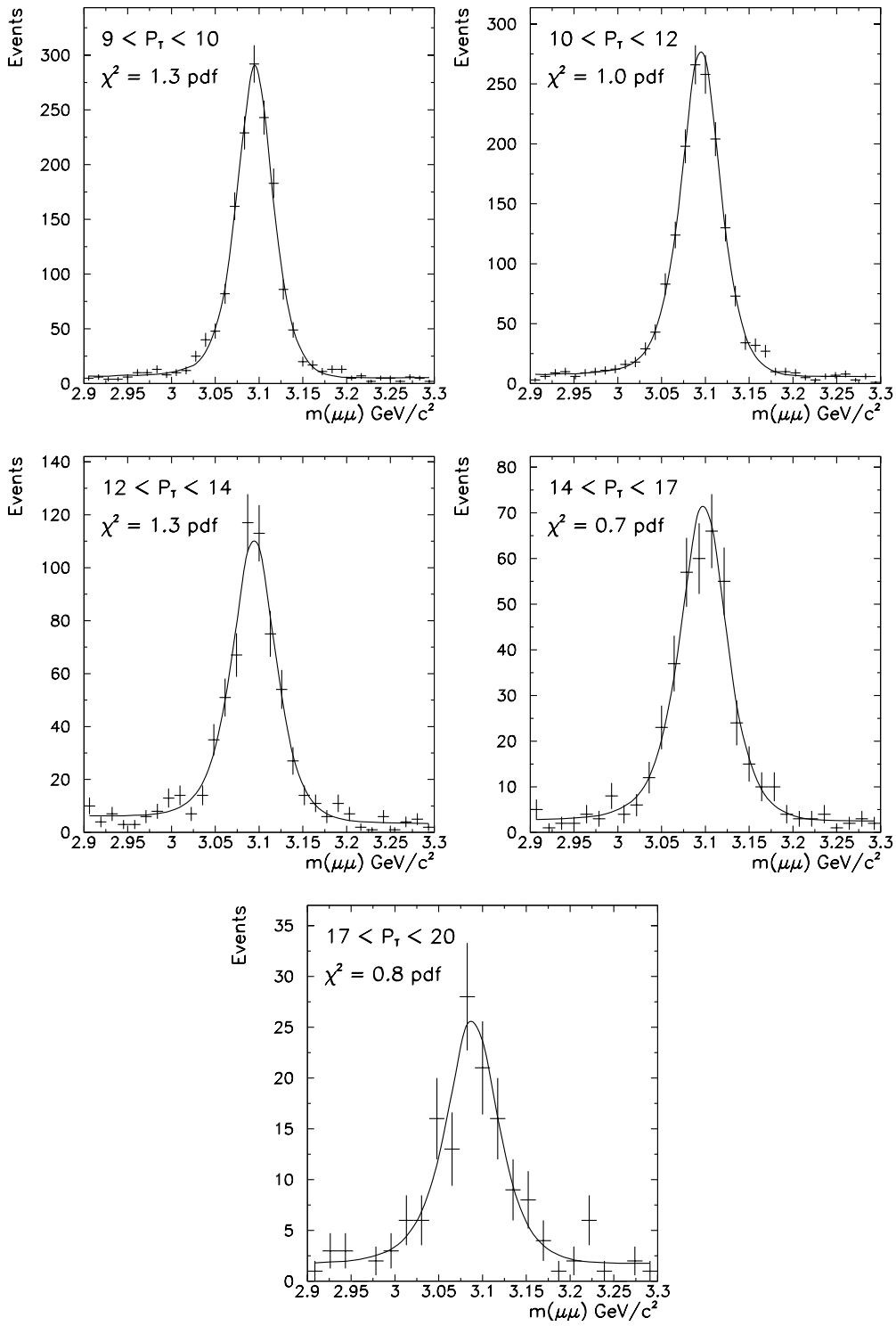

Figure 3-9: J/ψ mass distributions at high P_T, with radiative fit results overlaid.

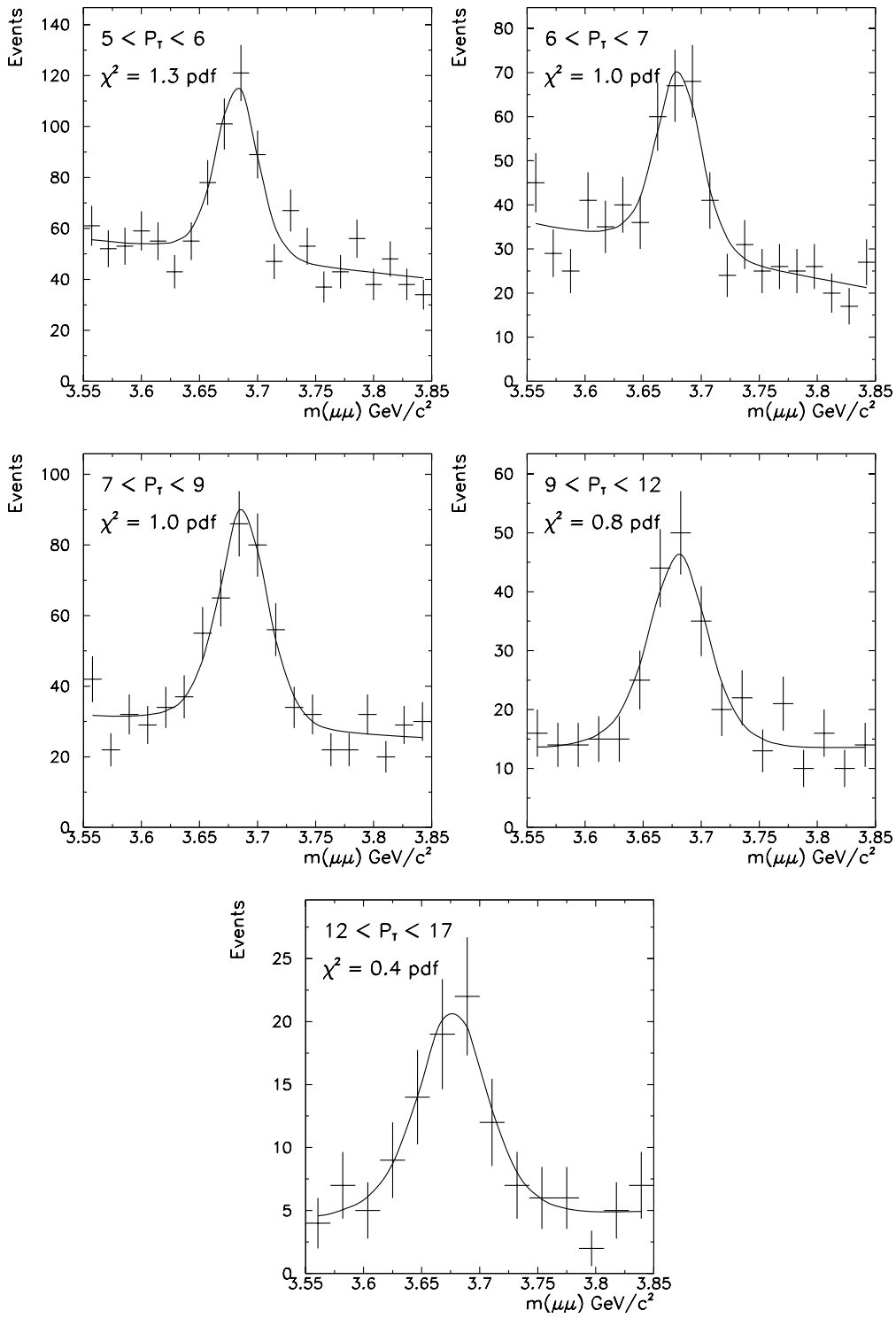

Figure 3-10: $\psi(2S)$ mass distributions, with radiative fit results overlaid.

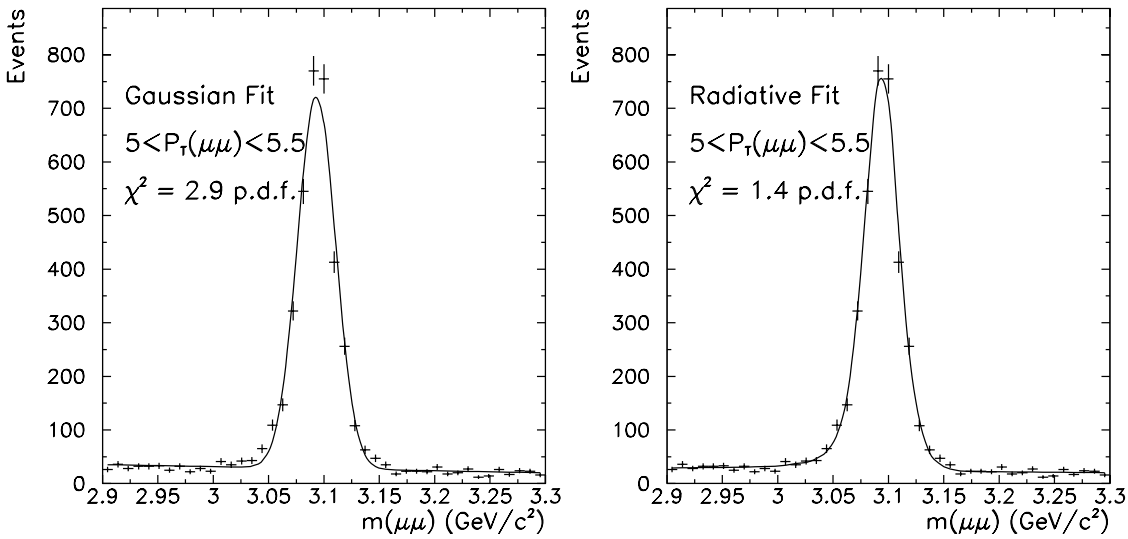

Figure 3-11: Results of fitting the J/ψ mass distribution to a Gaussian plus linear background (left) and using the radiative fit (right).

mass. The signal event masses are generated according to the shape used to fit the signal. The masses of the background events are generated according to a linear distribution with the same slope obtained by the data fit.

With each Monte Carlo sample, the generated masses are used to fill a histogram with the same bin sizes as used for the data, and the histogram is fit using the same code used to fit the data distributions. One can then choose various quantities, "figures of merit," related to the quality of the fit, and compare each figure of merit from the data fit to the distribution in the Monte Carlo fits. The Monte Carlo distribution is an indication of where the figure of merit should lie if the underlying model is accurate and the data is well described by the fit. Furthermore, one can use the Monte Carlo distribution to define a "confidence level" for each figure of merit. The confidence level should be uniformly distributed between 0 and 1 for data sets which are well described.

One figure of merit is the χ^2 of the fit. For the χ^2, the confidence level is the number of Monte Carlo fits with a larger χ^2 divided by the total number of Monte

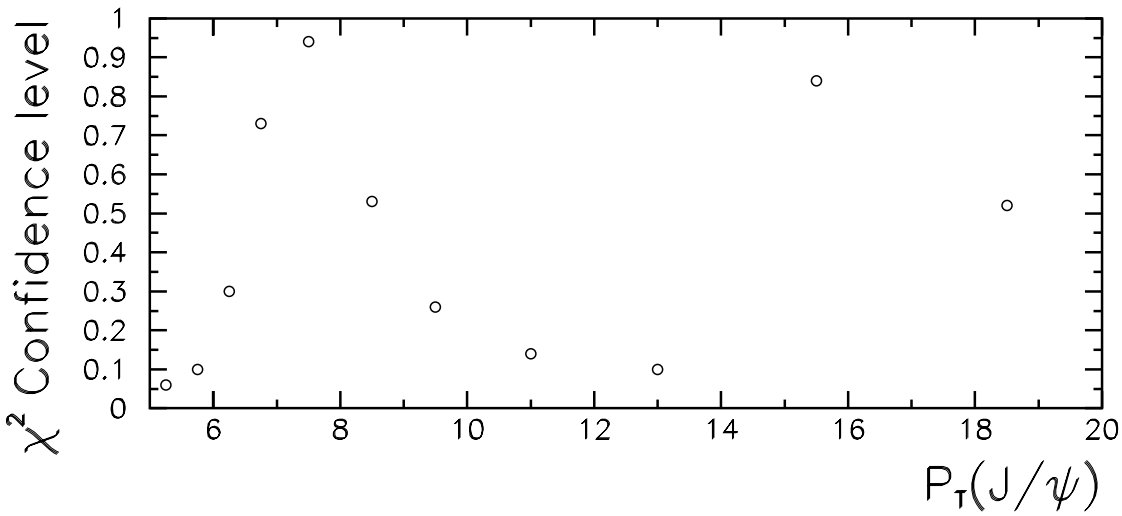

Figure 3-12: Confidence level of the mass fits, based on the χ^2 distribution.

Carlo fits. These are shown in Figure 3-12, and are evenly distributed over the entire interval. While this creates confidence that the fit describes the data, the number of events may be mismeasured. This is because the number of events is driven by only a few bins near the mass peak. Furthermore, the statistical error on the number of events in these bins is larger than in the other bins, allowing larger absolute differences between the data and the fit with only a small increase in the χ^2. If the model is inaccurate in this region, the number of events could be mismeasured without giving a large contribution to the χ^2. To test if this may be happening, a second figure of merit is defined,

$$\sum \mathrm{R} \equiv \sum_i (N_i - F_i) \tag{3.3}$$

where N_i is the number of events in the ith bin, F_i is the value of the fit in that bin, and the sum runs over all bins from 3.02 to 3.15 GeV/c^2 . In contrast to the χ^2, which provides a measure of the probability that the fitted distribution would produce the observed data, $\sum \mathrm{R}$ measures the difference between the expected and the observed number of events in a signal–rich region. While this difference could result from

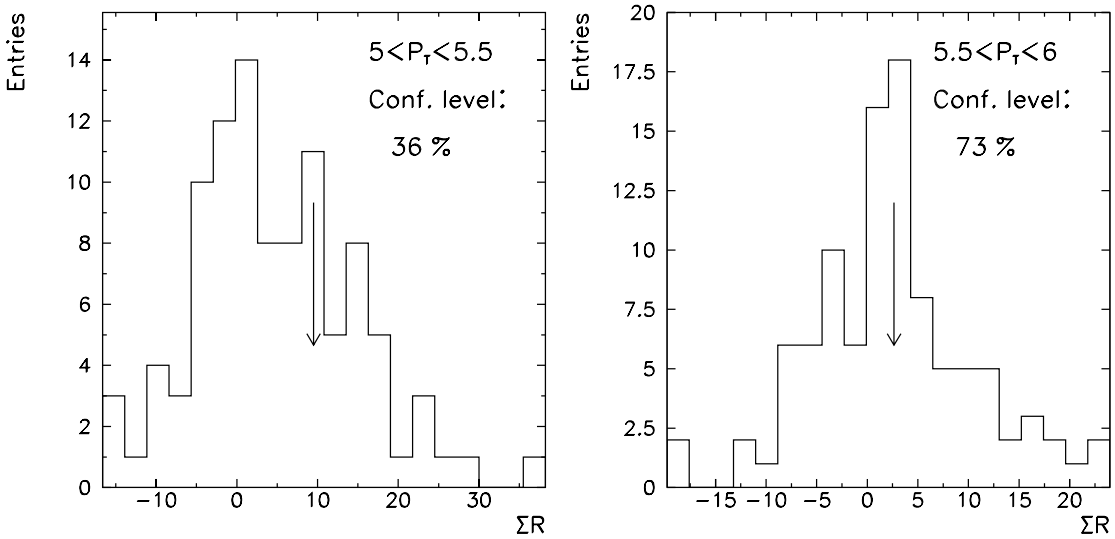

Figure 3-13: Distribution of $\sum$ R values for Monte Carlo (histogram) and data (arrow) in the first two P_T regions.

an excess/deficit of either background events or signal events, unexpectedly large values of $\sum$ R would probably stem from an excess/deficit of signal events, for a combination of two reasons. First, most of the events are signal events, so they are the most important part of calculating $\sum$ R. Secondly, the background level is a slowly varying function of the mass, and can be determined from the sideband regions, while the shape of the signal varies rapidly with mass, and the sidebands do not place a constraint on the number of signal events. For this figure of merit, the confidence level is defined as the number of Monte Carlo samples where $|\sum \mathrm{R}|$ is larger than $|\sum \mathrm{R}|$ in the data. Figure 3-13 shows the Monte Carlo distribution and the data value for $\sum$ R in the first two bins. While the confidence levels for these two figures of merit vary from as low as 1% to as high as 94%, they are consistent with being uniformly distributed over the region from 0 to 1. In addition to χ^2 and $\sum$ R, one additional set of figures of merit is used, the number of bins in which the fit is more than $N\sigma$ from the data, where N runs from 1 to 3.5 in steps of 0.5. There is no indication of problems in these variables either.

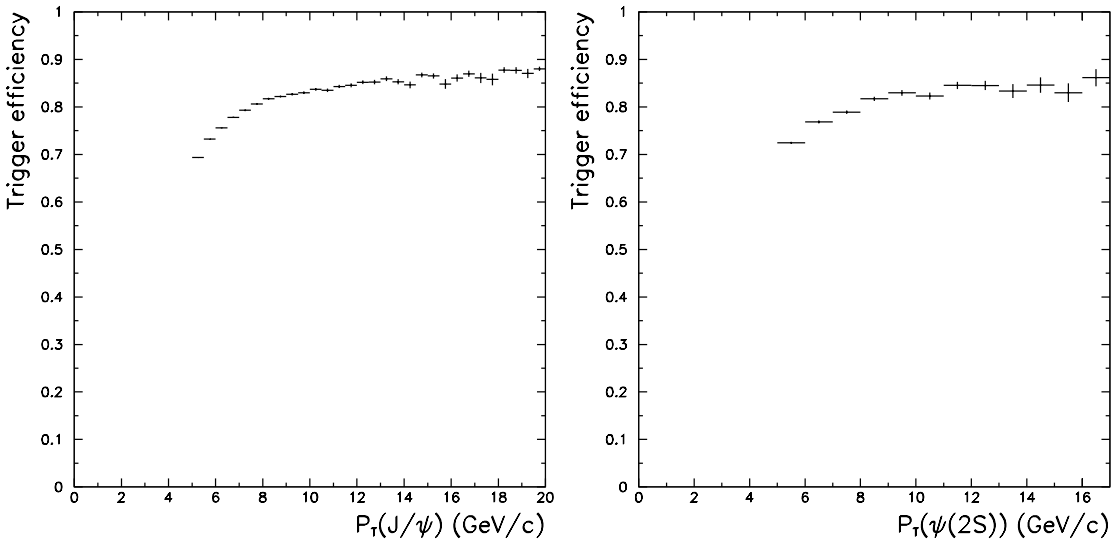

Figure 3-14: Average trigger efficiency for the J/ψ(left) and the $\psi(2S)$(right) candidates as a function of $P_T(\psi)$. The value is calculated by averaging over all events in the data sample.

In addition to checking the quality of the fit, the toy Monte Carlo can also be used to check for biases in the fit. Since the number of generated events is known, the difference between the fitted and the actual values can be calculated. If the mean of this distribution is significantly different from zero, it would indicate a bias in determining the number of events. The mean difference is less than 1% in every P_T bin, and is negligible compared to both the statistical and other systematic uncertainties.

3.2.3 Trigger Efficiency

The above fits measure the number of events reconstructed by this analysis. To extract the cross section, this number needs to be corrected for the fraction of events which fail to pass the trigger. To perform this correction, the mass distribution of the data events is weighted on an event by event basis by $1/\epsilon_{\text{Trigger}}$, where

$$\begin{aligned}\epsilon_{\text{Trigger}} &= \epsilon_{\text{L1}}(P_T(\mu^+)) \cdot \epsilon_{\text{L1}}(P_T(\mu^-)) \cdot \\ &\quad \{1 - [1 - \epsilon_{\text{L2}}(P_T(\mu^+))] \cdot [1 - \epsilon_{\text{L2}}(P_T(\mu^-))]\} \qquad (3.4)\end{aligned}$$

$P_T(J/\psi)$ (GeV/c)	ϵ(MC)/ϵ(Data)	$N_{\rm TC}/(N/\epsilon)$	$\delta N/N$
5-5.5	1.001	1.005	0.018
5.5-6	1.006	1.0001	0.019
6-6.5	1.004	1.002	0.020
6.5-7	1.007	0.9999	0.022
7-8	1.011	0.996	0.018
8-9	1.012	0.994	0.023
9-10	1.004	0.999	0.028
10-12	1.005	0.996	0.028
12-14	1.008	0.993	0.047
14-17	1.004	0.993	0.058
17-20	1.011	0.972	0.110

Table 3.2: Variations in the J/ψ trigger efficiency correction from different techniques for performing the correction. The second column is the ratio of the average trigger efficiency calculated from the Monte Carlo, divided by the same number, calculated in the data. The third column is the ratio of the number of events calculated by fitting the trigger corrected mass distribution and the number of events from fitting the uncorrected distribution, and dividing by the average trigger efficiency from the Monte Carlo. The last column shows the fractional statistical error on the number of events.

$P_T(\psi(2S))$ (GeV/c)	ϵ(MC)/ϵ(Data)	$N_{\rm TC}/(N/\epsilon)$	$\delta N/N$
5-6	0.99	1.02	0.11
6-7	0.997	1.004	0.14
7-9	0.999	0.99	0.10
9-12	1.001	0.99	0.13
12-17	0.99	1.004	0.19

Table 3.3: Variations in the $\psi(2S)$ from different techniques for performing the trigger correction. The columns are the same as in Table 3.2, except that the $\psi(2S)$ sample is used.

$\epsilon_{\mathrm{L1,L2}}(P_T)$ is the probability of a muon to pass the Level 1 or Level 2 trigger, as described in Section 2.3.8. The expression involving the Level 2 efficiencies expresses the probability of at least one of the muons passing the Level 2 trigger. The resulting mass distributions are fit for the number of events, using the same method as described previously. New templates are generated, as the trigger efficiency can affect the shape of the template. These templates are created in the same manner as described earlier in this section, except that the Monte Carlo events are not weighted by the trigger efficiency.

As a cross check, the trigger correction is performed using two other techniques. First, the average trigger efficiency of the Monte Carlo events (ϵ(MC)) is calculated in each P_T bin by averaging the calculated trigger efficiency for each event. The number of reconstructed events divided by the average efficiency gives the number of events corrected for the trigger efficiency. The average trigger efficiency can also be calculated using the data events (ϵ(Data)), just as with the Monte Carlo events. This efficiency is shown in Figure 3-14. All three techniques are in excellent agreement with each other, and are tabulated in Table 3.2 and Table 3.3.

3.3 Acceptance

Having determined the number of events, the next step in extracting the ψ cross section is to determine the detector and kinematic acceptance to ψ events.

The kinematical and detector acceptance is determined from Monte Carlo studies. The ψ Monte Carlo program described in Section 5.1 generates ψ events with a flat P_T spectrum. Each event is assigned a weight based on the predicted cross section as described in Section 3.2. The events are passed through the detector simulation QFL, described in Section 5.1.3.

After the events have been simulated, they are analyzed with a minor variant of the code used to analyze the data. As the Monte Carlo events contain only two charged particles and possibly a photon, there is no possibility that a reconstructed

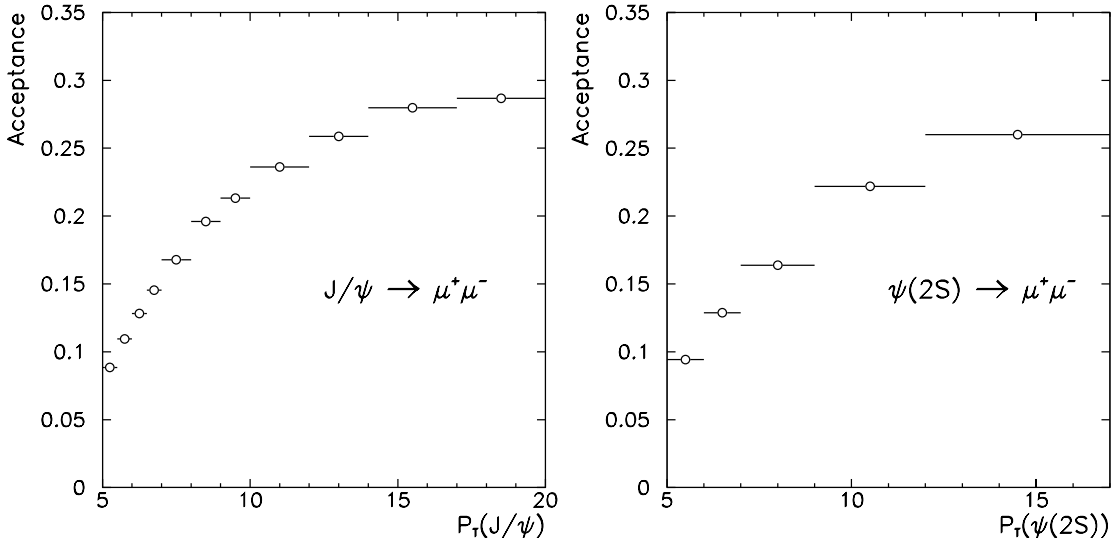

Figure 3-15: Detector acceptance for the J/ψ (left) and $\psi(2S)$ (right) as a function of P_T.

event is not a ψ, so the number of events is determined by summing the weights of all reconstructed events. Since we have not determined that the Monte Carlo correctly reproduces the non-kinematic aspects, such as the muon stub matching χ^2, only the kinematic cuts are applied. To calculate the acceptance in a particular P_T region, the total weight of all the events whose reconstructed P_T lies in that region (W_r) is divided by the total weight of all the events whose generated P_T lies in that region(W_g), so that

$$\alpha(P_T) = \frac{W_r}{W_g} \tag{3.5}$$

This is shown in Figure 3-15. In both cases, the generated P_T is used to calculate the weight of the event. Since the reconstructed P_T is used to determine the P_T region for the numerator, while the generated P_T is used for the denominator, after the acceptance correction is applied, the data is also corrected for any smearing between P_T bins. This smearing has several sources. First, there are events whose true P_T is near the edge of a bin, and the reconstructed value lies on the other side of the edge because of the detector resolution. Secondly, there are events where the true P_T is

above a bin edge, but the ψ decays radiatively into $\mu^+\mu^-\gamma$, and the momentum of the muon pair is below the edge of the bin.

Since there will be events that cross both the high and low bin edges in both directions, the amount of this correction will depend on the P_T distribution. However, this dependence is small. To measure this dependence, the cross section measured later in this chapter is parameterized. The detector and kinematical acceptance is recalculated using that parameterization as the input P_T spectrum. This changes the acceptance by 1%, independent of P_T.

The acceptance also depends on the polarization of the ψ. Taking θ^* to be the angle between the ψ direction in the lab frame and the positive muon direction in the ψ rest frame, the angular distribution of the decay will have the form

$$\frac{d\sigma}{d\cos\theta^*} \propto 1 + \alpha_{\rm pol}\cos^2\theta^* \tag{3.6}$$

where $\alpha_{\rm pol}$ is the polarization of the ψ. At low momentum, the CDF detector can only reconstruct ψ with large values of θ^*, as events with small θ^* produce asymmetric decays, and the low-P_T muon is too soft to be reconstructed. As the transverse momentum of the ψ increases, the soft muon becomes stiffer, and larger values of θ^* become accessible, reducing the uncertainty caused by the unknown polarization. Promptly produced ψ could have any value of $\alpha_{\rm pol}$ in the range $-1 \leq \alpha_{\rm pol} \leq 1$. Charmonia which are formed from the decay of B hadrons can be fully polarized in the B rest frame. However, boosting the ψ to the ψ rest frame tends to depolarize the ψ, which have an effective polarization $0.143(-0.219)$ in the ψ rest frame when the ψ polarization in the B rest frame is $+1(-1)$. In both cases, half the maximum variation is assigned as the systematic uncertainty due to the polarization.

3.4 Efficiencies

The acceptance calculated in the previous section includes neither the efficiency of the reconstruction algorithms, nor the effects of the non-kinematical event selection

criteria. These must be calculated separately.

The efficiency of the offline CTC track reconstruction is measured by adding hits to events, and attempting to reconstruct the added track. This efficiency is found to depend on the density of tracks near the embedded track. Only a few percent of the data is in the region where the tracking efficiency is less than its plateau value. The average efficiency for reconstructing both tracks is $96.4 \pm 2.8\%$.

The efficiency of CMU stub reconstruction and CMU-CTC linking is measured using data from a single muon trigger.[44] One muon is required to pass the trigger, and a second muon is reconstructed using the Central Muon Upgrade (CMP). These muon chambers overlap the coverage of the CMU chambers, but have more absorber before them. The tracks for these muons are required to project through an active CMU chamber, and to not be near the edge of the CMU chamber. The mass of the dimuons with and without a CMU stub is calculated, and the number of J/ψ events in each distribution is fit to determine the efficiency of $97.2 \pm 1.2\%$.

There is a range of runs for which the CTC was not properly calibrated. As a result, the Level 3 trigger was less efficient in those runs. Those runs are excluded from the J/ψ, but included in the $\psi(2S)$ analysis. This drop in efficiency is measured by comparing the observed rate of J/ψ production during the "good" runs and the "bad" runs. This gives an effective Level 3 trigger efficiency of $92.3 \pm 2\%$ for the $\psi(2S)$ analysis. The Level 3 trigger efficiency for the J/ψ analysis is $97 \pm 2\%$,[39] as is described in Section 3.1.3.

The efficiency of the muon quality requirements are determined using the J/ψ sample. The number of J/ψ events before and after the requirements is determined by performing a sideband subtraction, and the efficiency is the ratio of these two numbers. The efficiency of each requirement listed above the double line in Table 3.4 is measured separately, but the efficiencies cannot be combined in a simple manner, since there are correlations. The total efficiency is measured by determining the number of J/ψ events with no requirements and with all of the requirements. This shows that the event selection requirements are $90.5 \pm 1\%$ efficient. The efficiency is

Source	Efficiency (%)
$\chi^2_{\mathrm{FIT}} < 10$	99.0 ± 0.9
$\chi^2_{\mathrm{CMU,R-\phi}} < 9$(High P_T)	$99.5^{+0.5}_{-0.9}$
$\chi^2_{\mathrm{CMU,R-\phi}} < 9$(Low P_T)	$99.6^{+0.4}_{-0.9}$
$\chi^2_{\mathrm{CMU,R-z}} < 9$(High P_T)	98.4 ± 0.9
$\chi^2_{\mathrm{CMU,R-z}} < 9$(Low P_T)	99.0 ± 0.9
$\lvert\Delta z\rvert < 5$	$99.7^{+0.3}_{-0.9}$
$\lvert z\rvert < 60$ cm (High P_T)	96.4 ± 0.9
$\lvert z\rvert < 60$ cm (Low P_T)	96.4 ± 0.9
Hadronic Energy (High P_T)	$100.0^{+0.0}_{-0.9}$
Hadronic Energy (Low P_T)	$99.9^{+0.1}_{-0.9}$
ADC hits (High P_T)	99.0 ± 0.9
ADC hits (Low P_T)	99.1 ± 0.9
All event selection requirements	90.5 ± 1
Level 3 Trigger	$97 \pm 2(92.3 \pm 2)$
CTC Track Reconstruction	96.4 ± 2.8
CMU Reconstruction and Linking	97.2 ± 1.2

Table 3.4: Efficiencies for J/ψ and $\psi(2S)$ reconstruction. All efficiencies are assumed to be the same for the J/ψ and the $\psi(2S)$, except for the Level 3 Trigger efficiency. For that case, the $\psi(2S)$ efficiency is given in parentheses. The efficiencies of some of the requirements listed above the double line are correlated, especially the $|z| < 60$ cuts. The efficiency given by "All event selection requirements" correctly takes the correlations into account, by measuring the efficiency of applying all the requirements at once.

also determined as a function of P_T, but there is no statistically significant deviation from a constant efficiency. The efficiencies are summarized in Table 3.4.

3.5 Cross Section

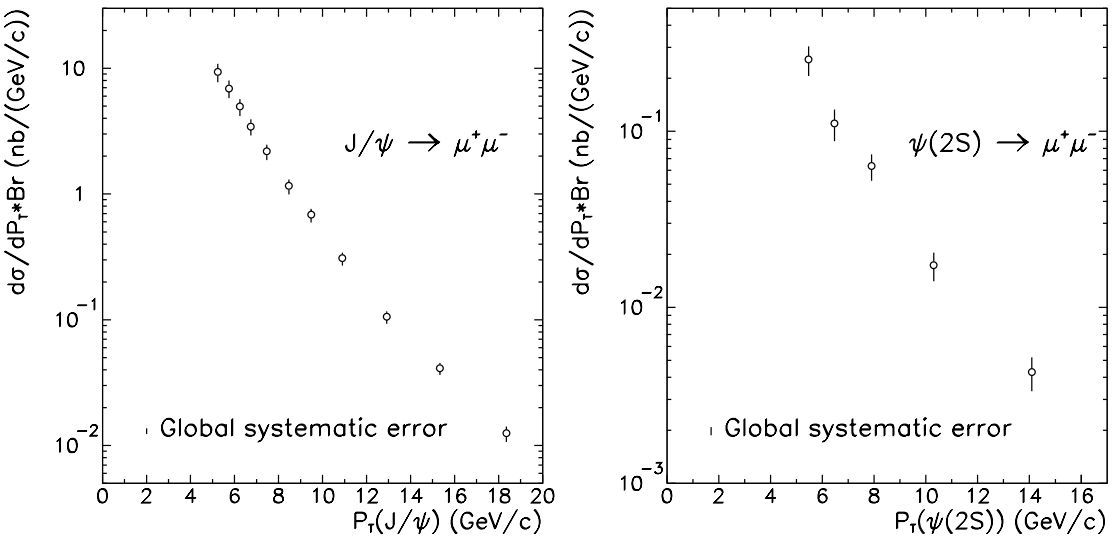

Figure 3-16: J/ψ(left) and $\psi(2S)$(right) differential cross sections. The error bars are the statistical and the P_T-dependent systematic uncertainties, added in quadrature.

The ψ differential cross section is defined by

$$\frac{d\sigma}{dP_T}(\psi) \cdot \mathcal{B}(\psi \to \mu^+\mu^-) = \frac{N_T(\psi)}{\alpha \cdot \epsilon \cdot \int \mathcal{L}dt \cdot \Delta P_T} \tag{3.7}$$

where $N_T(\psi)$ is number of ψ candidates in the bin after correcting for the trigger efficiency, α is the detector and kinematic acceptance, ϵ is the combined event selection and reconstruction efficiencies, $\int \mathcal{L}dt$ is the integrated luminosity, and ΔP_T is the size of the P_T bin.

Figure 3-16 shows the differential cross sections for the two states, and Table 3.5 and Table 3.6 tabulate the results. Table 3.7 summarizes the systematic uncertainties.

$P_T(J/\psi)$(GeV/c)	$\frac{d\sigma}{dP_T} \cdot \mathcal{B}$ (nb/GeV/c)
5-5.5	$9.32^{+1.56}_{-1.62}$
5.5-6	$6.92^{+1.11}_{-1.17}$
6-6.5	$4.95^{+0.76}_{-0.81}$
6.5-7	$3.44^{+0.50}_{-0.55}$
7-8	$2.19^{+0.30}_{-0.34}$
8-9	$1.16^{+0.15}_{-0.17}$
9-10	$0.685^{+0.082}_{-0.096}$
10-12	$0.310^{+0.035}_{-0.042}$
12-14	$0.106^{+0.012}_{-0.014}$
14-17	$0.0413^{+0.0044}_{-0.0053}$
17-20	$0.0125^{+0.0017}_{-0.0019}$

Table 3.5: The differential J/ψ cross section as a function of P_T, for $|\eta(\psi)| < 0.6$. The errors are the statistical and systematic errors added in quadrature.

$P_T(\psi(2S))$(GeV/c)	$\frac{d\sigma}{dP_T} \cdot \mathcal{B}$ (nb/GeV/c)
5-6	0.26 ± 0.05
6-7	0.11 ± 0.02
7-9	$0.064^{+0.011}_{-0.012}$
9-12	0.017 ± 0.003
12-17	$0.0043^{+0.0009}_{-0.0010}$

Table 3.6: The differential $\psi(2S)$ cross sections as a function of P_T, for $|\eta(\psi)| < 0.6$. The errors are the statistical and systematic errors added in quadrature.

Source	J/ψ	$\psi(2S)$	Ratio
*L1 Trigger	6.4%	6.1%	0.2%
*L2 Trigger	1.1%	1.0%	0.2%
L3 Trigger	2%	2%	-
*B Polarization	5%	5%	2.5%
*Prompt Polar.	15%	15%	7.5%
Luminosity	3.6%	3.6%	-
Event Selection	0.9%	0.9%	-
Tracking efficiency	2.9%	2.9%	-
Reconstruction	1.2%	1.2%	-
MC statistics	1%	2%	2%
Total	9.5%(17%)	9.7%(17%)	3.2%(7.8%)

Table 3.7: Fractional systematic uncertainties in the cross section measurements. Items marked with * are P_T-dependent, and the uncertainty on the integrated cross section is given. The total uncertainty is the uncertainty on the B (prompt and inclusive) cross sections.

The integrated cross sections are

$$\sigma(J/\psi) \cdot \mathcal{B}(J/\psi \to \mu^+\mu^-) = 17.4 \pm 0.1(\text{stat})^{+2.6}_{-2.8}(\text{sys}) \text{ nb} \tag{3.8}$$

$$\sigma(\psi(2S)) \cdot \mathcal{B}(\psi(2S) \to \mu^+\mu^-) = 0.57 \pm 0.04(\text{stat})^{+0.08}_{-0.09}(\text{sys}) \text{ nb} \tag{3.9}$$

where

$$\sigma(\psi) = \sigma(\text{p}\overline{\text{p}} \to \psi\text{X}, P_T(\psi) > 5 \text{ GeV/c}, |\eta(\psi)| < 0.6) \tag{3.10}$$

Using the measured branching ratios of $\mathcal{B}(J/\psi \to \mu^+\mu^-) = 5.9 \pm 0.25\%$,[45] and $\mathcal{B}(J/\psi \to \mu^+\mu^-) = 0.88 \pm 0.13\%$[46], this yields absolute cross sections of

$$\sigma(J/\psi) = 295 \pm 2(\text{stat})^{+44}_{-47}(\text{sys}) \pm 13(\mathcal{B}) \text{ nb} \tag{3.11}$$

$$\sigma(\psi(2S)) = 64 \pm 5(\text{stat})^{+9}_{-10}(\text{sys}) \pm 9(\mathcal{B}) \text{ nb} \tag{3.12}$$

where the last error comes from the uncertainty in the branching ratios.

This is the cross section for ψ production from any source. In order to simplify

the comparison with theoretical predictions, the cross section can be divided into the cross section from each of the components. That is the topic of the next chapter.

Chapter 4

Production Fractions

As discussed in Chapter 1, the cross section measured in the previous chapter is the combination of several different production mechanisms. In order to simplify the comparison with theory, we now separate the measurement into the different components. The component from B decays has a distinctive feature, namely, the displaced decay vertex of the ψ resulting from the B proper lifetime of $c\tau_{\mathrm{B}} \approx 450\mu$m. The SVX is capable of resolving vertices with a resolution of $\sim 40\mu$m, so ψ events that are B daughters can be tagged by the clearly displaced vertices. The fraction of ψ events from B decays can thereby be measured by analyzing the decay length distribution of the ψ. For the non-B production modes, the decay lengths are typically nine orders of magnitude smaller than the B decay length and experimentally are characterized by the SVX resolution. These modes are grouped together under the name "prompt production." For the J/ψ, this component can be further divided by reconstructing $\chi_c \rightarrow J/\psi\gamma$ decays. The fraction of J/ψ produced from χ_c is separated in this manner from the "direct production," where the J/ψ is produced in the initial interaction, instead of being produced from the decay of an intermediate state.

4.1 B Fraction

The first step in disentangling the components which form the ψ cross section is to separate the component coming from B decays from the prompt components. This is done by fitting the apparent decay length distribution of the ψ.

4.1.1 Decay Length Measurement

In order to obtain an accurate measurement of the decay length, both muons are required to be reconstructed in the SVX. To avoid introducing biases into the B fraction, the only requirement placed on the muons is that there are at least three hits in the SVX associated with the track. Many of the requirements typically imposed on SVX tracks at CDF are *de facto* isolation requirements. These are inherently less efficient on ψ events resulting from the decay of B hadrons, as the other B daughters will be nearby. For the events in which both of the muons are reconstructed in the SVX, the tracks are refit with the requirement that they extrapolate to a common vertex in three dimensions. This vertex gives the ψ production vertex, also referred to as the secondary vertex, for this is where the B decays when the ψ is produced as the result of a B decay.

To measure the decay length, in addition to the secondary vertex, the $p\overline{p}$ interaction vertex or primary vertex must be known. One could attempt to measure this vertex on an event by event basis, using the other tracks in the event. There are potential problems with this technique. Each event will contain tracks from the primary vertex resulting from the fragmentation process and the underlying event. If the event is a B event, however, there will also be tracks from the other decay products of the B that produced the ψ, and the decay products of the second b-flavored hadron in the event. It is difficult to exclude the other B daughters from the determination of the primary vertex, and including them can shift the location of the reconstructed vertex. Furthermore, ψ events tend to have relatively low track multiplicities, so even if only the correct tracks are used, it may not be possible to accurately reconstruct

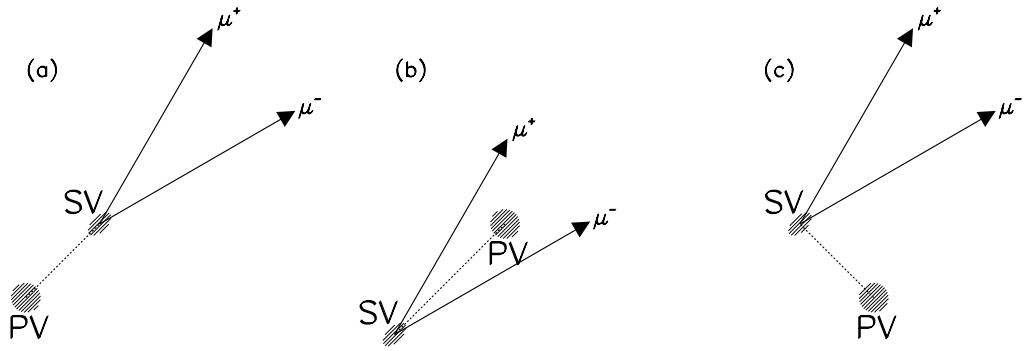

Figure 4-1: Possible decay configurations. PV indicates the primary vertex, and SV the secondary vertex. The arrows show the direction of the two muons. (a) is the normal (physical) configuration. (b) is an unphysical scenario, and indicates an incorrectly reconstructed vertex. (c) is also unphysical, and can cause problems defining the error of a signed decay length.

the primary vertex. ψ candidate events in the data have an average of eight tracks with $P_T > 1$ GeV/c, and only one track with $P_T > 2$ GeV/c. This includes any B daughters that are present.

For these reasons, the run-averaged beam position described in Chapter 2 is used to calculate the production vertex. The SVX provides an excellent measurement of the beam position, as was already shown in Figure 2-7. The beam does not lie exactly parallel to the central axis of the CDF detector, but moves radially by a few microns for every centimeter moved in the z direction. This results in a change of ≈ 100 μm from $z = 0$ to the outer edge of the SVX. Given the $\sim 40\mu$m resolution on secondary vertices, this will induce a significant bias into the B fraction measurement if it is not correctly taken into account. To correct for this effect, the VTX vertex nearest in z to the ψ candidate is used to determine the z of the primary vertex. From this, the location of the beam line in the transverse plane is determined, and the primary vertex is assumed to lie at the center of the beam. Using this algorithm, the uncertainty in the location of the primary vertex is dominated by the beam size, which has a Gaussian distribution with a width of 40μm in both transverse directions.

The relation between the ψ momentum vector and the decay length direction

provides information about the quality of the event reconstruction. Figure 4-1a shows a physical decay configuration where the parent traveled forward from the primary vertex to the secondary vertex, and then decayed. Figure 4-1b shows an unphysical decay configuration, where the parent apparently moved oppositely to its momentum, and then decayed. This can result either from a prompt particle, where the resolution caused the decay vertex to be reconstructed behind the primary vertex, or from an incorrectly reconstructed vertex.

This information is used by associating a sign with the decay length. One method is to take the dot product of the momentum vector and the decay length vector, and assign the sign of the product to the decay length. In this case, it is difficult to define a useful error on the decay length. For example, consider the case in Figure 4-1c, where the two vectors are nearly perpendicular. Moving the decay vertex a small distance along the momentum direction will cause the decay length to change from large and positive to large and negative, while the measured error can be much smaller.

A better solution is to use the projection of the decay length onto the ψ transverse momentum. This value is called L_{xy} to emphasize that is is measured only in the $x - y$ plane, and is shown graphically in Figure 4-2. The error on L_{xy} is well-defined, even for configurations such as Figure 4-1c. Also, in that case, if the event is a real ψ, as opposed to a background event, this removes an incorrect component from the measurement. However, whatever mechanism caused the secondary vertex to be mismeasured perpendicular to the ψ momentum may have also affected the measured location along the direction of the momentum. This (possible) error cannot be corrected using the available information, and results in non-Gaussian tails in the resolution function.

While the L_{xy} distribution could be analyzed directly, the analysis is simplified by using the Lorentz invariant proper lifetime of the B, τ. If the B lived for a time t before decaying in the CDF lab frame, then $t = L_{xy}/v_{xy}$, where v_{xy} is the B velocity in the transverse plane. Then

$$\tau = \frac{t}{\gamma} = \frac{L_{xy}}{v_{xy}\gamma} \tag{4.1}$$

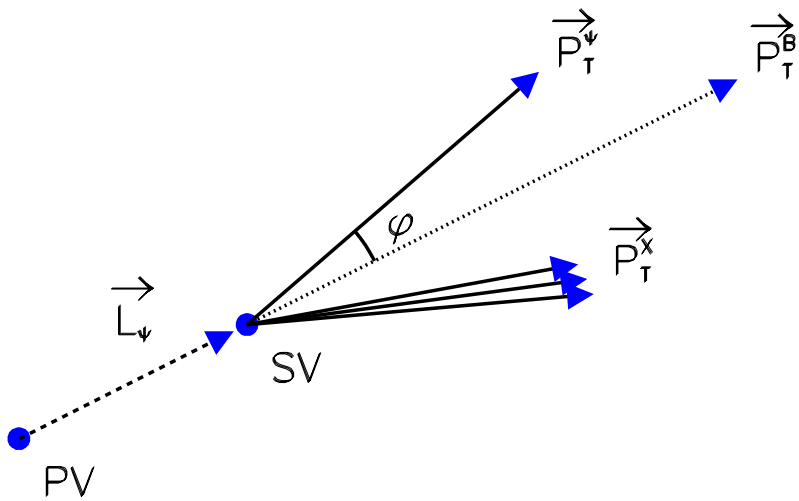

Figure 4-2: The variables used to define L_{xy}, shown in the transverse plane. By using $L_{xy} \equiv \vec{L_\psi} \cdot \vec{P_T}^{\psi} / P_T{}^{\psi}$, the error on L_{xy} is well defined, even for configurations such as Figure 4-1c.

where $\gamma = 1/\sqrt{1-\beta^2}$. v_{xy} can be determined by noting that

$$P_T = m\beta_T\gamma c = m\left(\frac{v_{xy}}{c}\right)\gamma c \tag{4.2}$$

where m is the B rest mass and $\beta_T = v_{xy}/c$. We then have

$$c\tau = L_{xy} \cdot \frac{mc}{P_T} \tag{4.3}$$

There is only one problem with this – P_T is the transverse momentum of the B (which isn't measured), not the transverse momentum of the ψ (which is measured). Fortunately, the ψ takes most of the energy and momentum of the B. Thus, the ψ can be used as an initial estimator of the B momentum and direction.

Since the ψ momentum and the B momentum (or, more accurately, $\vec{\beta_T}\gamma$) are not identical, the $c\tau$ calculated using the ψ quantities are not accurate. A decay length of $L_{xy} = L_{xy}^{\mathrm{B}} \cos\varphi$ is reconstructed for a B which travels a transverse distance L_{xy}^{B}

before decaying into a ψ which moves at an angle φ relative to the B direction in the transverse plane. The $\beta\gamma$ correction will be incorrect by a factor of $\frac{P_T(\mathrm{B})/m_\mathrm{B}}{P_T(\psi)/m_\psi}$. To correct for these effects, the B Monte Carlo described in Section 5.1.1 is used to determine a correction factor. The average correction factor is then

$$F_{\mathrm{corr}}(P_T(\psi)) = \left\langle \frac{P_T(\mathrm{B})/m_\mathrm{B}}{P_T(\psi)/m_\psi} \cos\varphi \right\rangle \tag{4.4}$$

This is calculated by averaging over Monte Carlo events in a P_T region passing the kinematic cuts used in this analysis. With this correction factor, we can calculate the "pseudo-$c\tau$,"

$$c\tau = \frac{L_{xy}}{(P_T(\psi)/m_\psi) \cdot F_{\mathrm{corr}}(P_T(\psi))} \tag{4.5}$$

Figure 4-3 shows the correction factor as a function of P_T for the J/ψ and the $\psi(2S)$. For both particles, there is only a slight P_T dependence at low P_T, which quickly plateaus.

The requirement that both muons be reconstructed in the SVX in order to accurately measure L_{xy} reduces both data samples by about a factor of two. To improve the accuracy of the measurement, about 90 pb^{-1} of data from the 1993-1995 collider run are added. This data is not used to measure the cross section, as the analysis of the efficiencies is not complete. The only difference in analyzing this data is that the muon P_T requirements are lowered to 2 GeV/c on both muons, as is implemented in the trigger.

4.1.2 L_{xy} Distribution

Before the fraction of ψ from B can be measured, the $c\tau$ distribution of the background must be understood. Whereas the background in the mass distribution is well described by a straight line, the background in the $c\tau$ distribution is more complicated. To determine the background shape, the $c\tau$ distribution of events that lie in the sidebands of the mass distribution are used.

Because of the radiative tail in the mass distribution, the lower sideband will

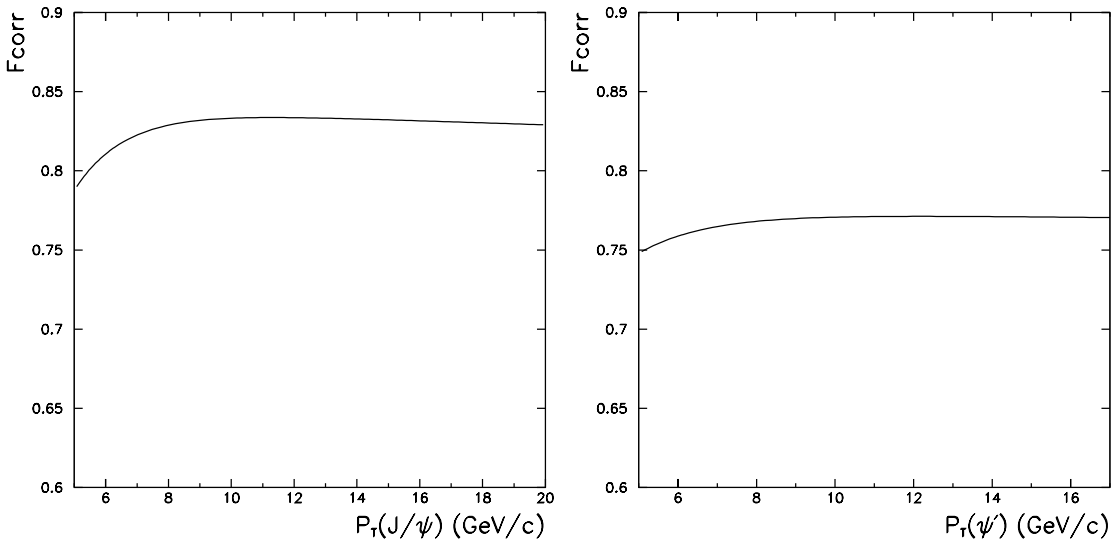

Figure 4-3: The Monte Carlo correction factor $F_{\rm corr}$ for the J/ψ(left) and the $\psi(2S)$(right). $F_{\rm corr}$ relates the $c\tau$ calculated with the ψ parameters to the true $c\tau$ of the B. Both plots have suppressed zeroes.

contain a small number of real ψ events. This should be 1-2% of the total number of ψ events, based on the fraction of the SVX-SVX template in this region, described in Section 3.2. Since the ψ and background distributions have similar shapes, *i.e.*, a large prompt component with asymmetrical tails, this will be interpreted as an additional background when the data is fit to extract the B fraction. As a result, a similar (small) fraction of ψ events in the signal region will be interpreted as background, slightly decreasing the statistical power of the fit. The exact fraction depends on the ratio of the sizes of the signal region and the sideband region, but is about 1%.

The shape of the $c\tau$ distribution of the background components described in Section 3.1.2 is the sum of several distinct distributions. One obvious feature is a large prompt component. This is attributed to punch-through and decay-in-flight after the hadron leaves the CTC. Since most of the particles created at CDF come from the primary vertex, and these backgrounds produce well-measured tracks, the vertices reconstructed from these background events will be consistent with the primary vertex.

There are also clear non-Gaussian tails in both the positive and negative $c\tau$ regions which have several sources. Displaced vertices can arise from muons produced by decay-in-flight. When a pion or a kaon decays, there will be a "kink" at the point of decay. If the decay occurs before or inside the SVX, the resulting muon track will not extrapolate back to the primary vertex. When combined with another track, the resulting vertex will be displaced.

Sequential decays of B hadrons will also produce an opposite sign muon pair, whose mass will sometime be near or at the ψ mass. $b\overline{b}$ and $c\overline{c}$ production can also result in an opposite sign muon pair. While the muons are often separated by a large angle, resulting in a large invariant mass, a low mass pair could result if the B(D) and the $\overline{\mathrm{B}}(\overline{\mathrm{D}})$ are nearby, as is often the case in gluon splitting. As the SVX only provides two-dimensional information, these decays are often reconstructed as coming from a single vertex. Furthermore, this vertex will tend to be displaced with a positive L_{xy}.

In addition to these tails, which result from real physical processes, displaced vertices can be generated by incorrect track reconstruction. If the track reconstruction assigns incorrect SVX hit(s) to the muon candidates, an artificially displaced vertex can be created. Even if the particle came from the primary vertex, the extrapolation will be skewed by the incorrect hit(s).

Parameterization

The data is fit using an unbinned log-likelihood fit. This requires a probability density function for the $c\tau$ distribution of each event. Deriving this function for the background would require a study of each component of the background, plus a detailed understanding of the possible failures of the tracking system. Fortunately, a practical approach, whereby the background is described as the sum of several empirical terms, can be justified *a posteriori*.

The background distribution is constructed from the following components. The prompt component is represented by a Gaussian. The width of the Gaussian is taken to be the measured error on the $c\tau$ of each event, multiplied by a global scale factor.

This scale factor arises because the measured error may not correctly account for the uncertainty in the measurement. The fits indicate that the scale factor deviates from unity by up to 10%. In addition, three exponentials are added, one describing the $c\tau > 0$ region, one describing the $c\tau < 0$ region, and one which is symmetric about $c\tau = 0$. An asymmetry is expected in the lifetime distribution, as the heavy flavor events will tend to have positive $c\tau$. This is also observed in the data. The lifetime and normalization of the three exponentials is independent.

The ψ L_{xy} distribution is the sum of two components. The prompt component of the signal is parameterized by the resolution function, which is a Gaussian with symmetric exponential tails. The width of the Gaussian is the error measured for that event, scaled by the same factor used for the background. The B component is represented by an exponential with $c\tau > 0$ convoluted with the resolution function.

The full parameterization of the signal and background regions are

$$S(c\tau) = (1 - f_B) \cdot R(c\tau) + f_B \cdot \int_0^\infty dc\bar{\tau}\, E(c\bar{\tau}; c\tau_0) \cdot R(c\tau - c\bar{\tau}) \tag{4.6}$$

$$B(c\tau) = \begin{cases} (1 - f_+ - f_- - f_{\text{sym}})G(c\tau;\rho\sigma) + f_+ \cdot E(c\tau;\lambda_+) + \\ \qquad \tfrac{1}{2} f_{\text{sym}} \cdot E(c\tau;\lambda_{\text{sym}}) & , c\tau > 0 \\ (1 - f_+ - f_- - f_{\text{sym}})G(c\tau;\rho\sigma) + f_- \cdot E(c\tau;\lambda_-) + \\ \qquad \tfrac{1}{2} f_{\text{sym}} \cdot E(c\tau;\lambda_{\text{sym}}) & , c\tau \leq 0 \end{cases} \tag{4.7}$$

where

$S(c\tau)$		the signal function
$B(c\tau)$		the background function
$R(x)$	$=$	$(1 - f_{\text{tail}}) \cdot G(x;\rho\sigma) + f_{\text{tail}} \cdot \frac{1}{2} E(x;\lambda_{\text{tail}})$
$G(x;\sigma)$	$=$	$\frac{1}{\sqrt{2\pi}\sigma} \exp\left(-\frac{x^2}{2\sigma^2}\right)$
$E(x;\lambda)$	$=$	$\frac{1}{\lambda} \exp\left(-\frac{\lvert x\rvert}{\lambda}\right)$
f_B		B fraction

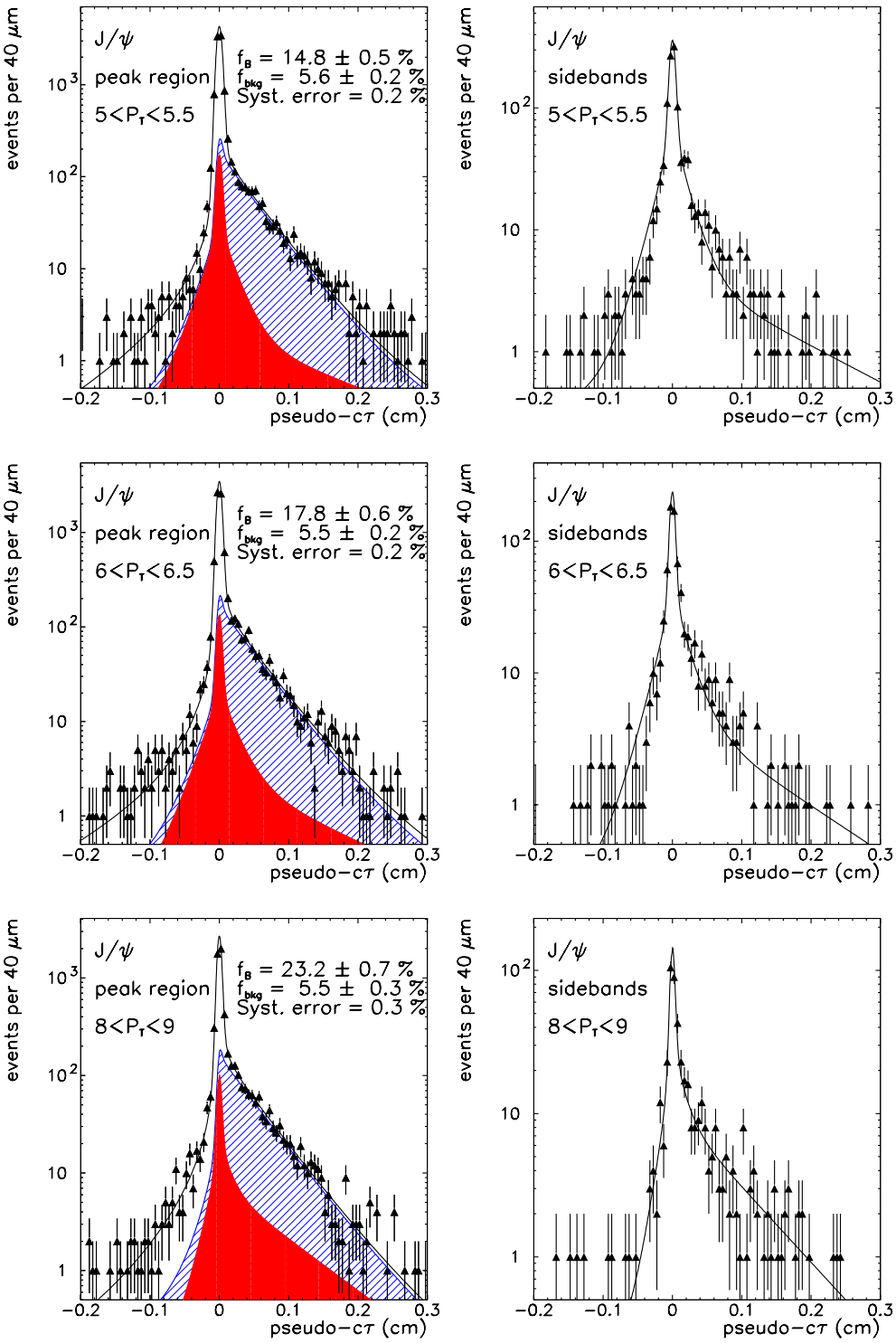

Figure 4-4: J/ψ $c\tau$ distributions, with fit results overlaid. In the signal region (left plots), the solid region is the background shape and the hashed region is the excess of the B component over the background. The solid line represents the total function.

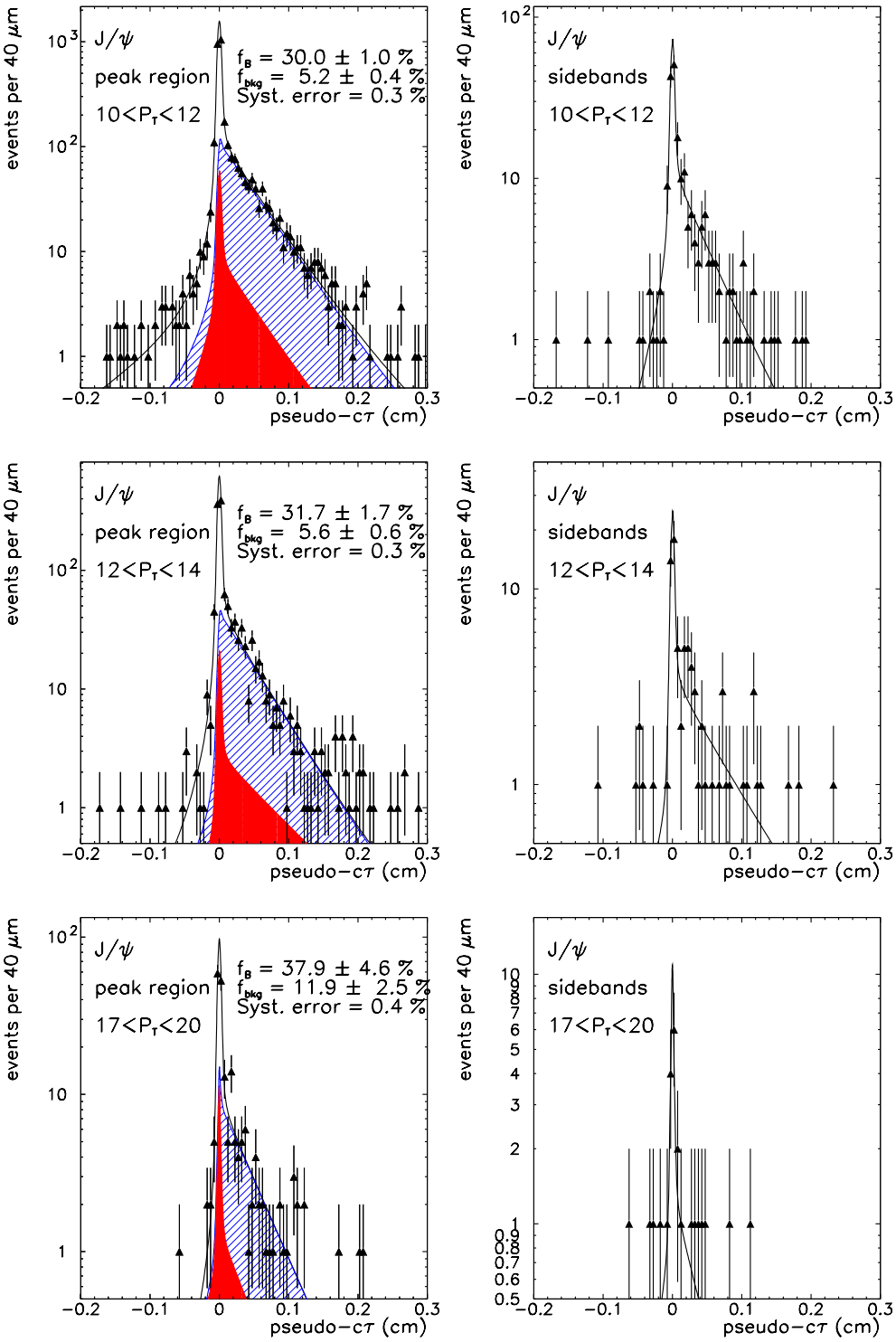

Figure 4-5: The same as Figure 4-4 for higher P_T bins.

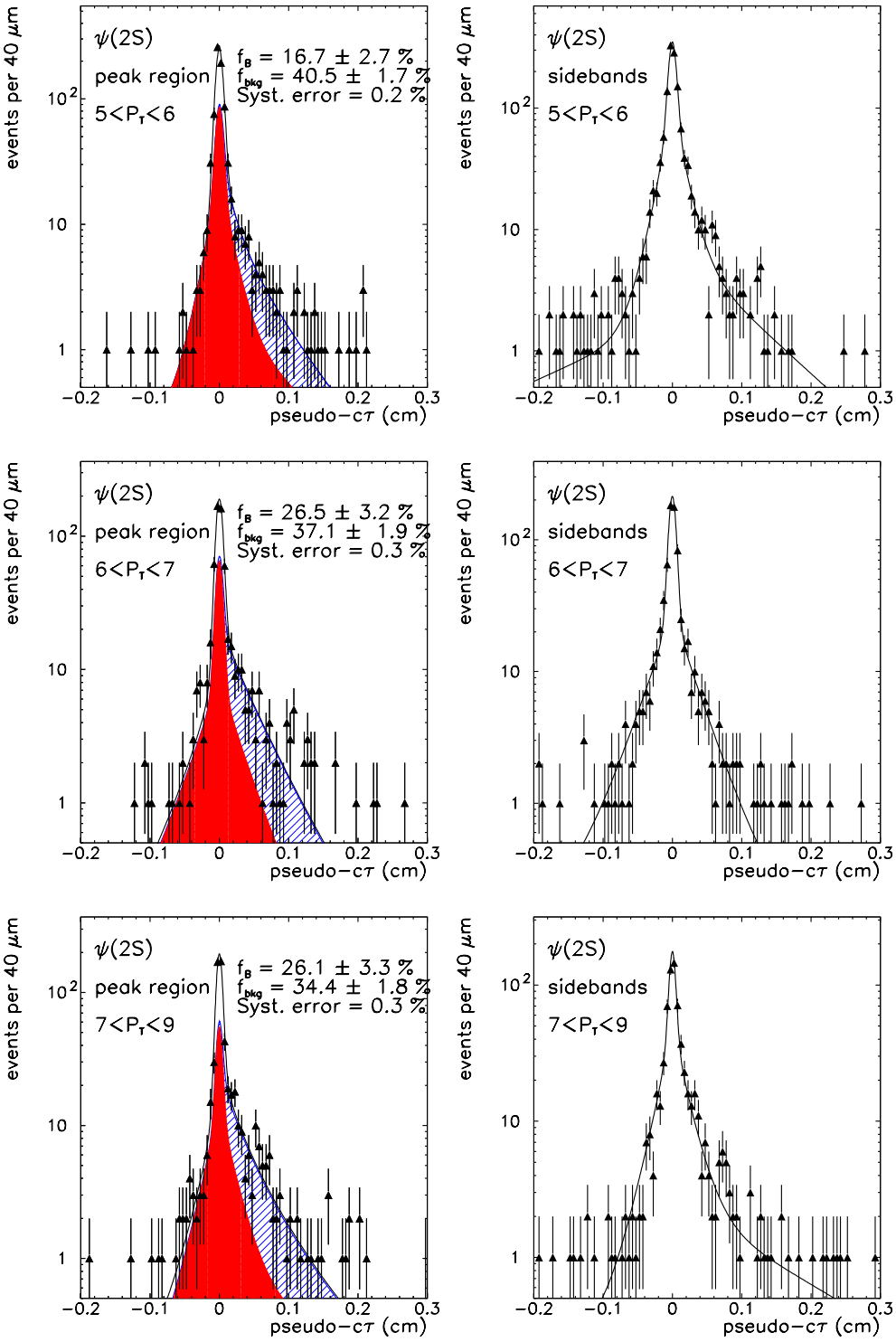

Figure 4-6: The same as Figure 4-4 for the $\psi(2S)$.

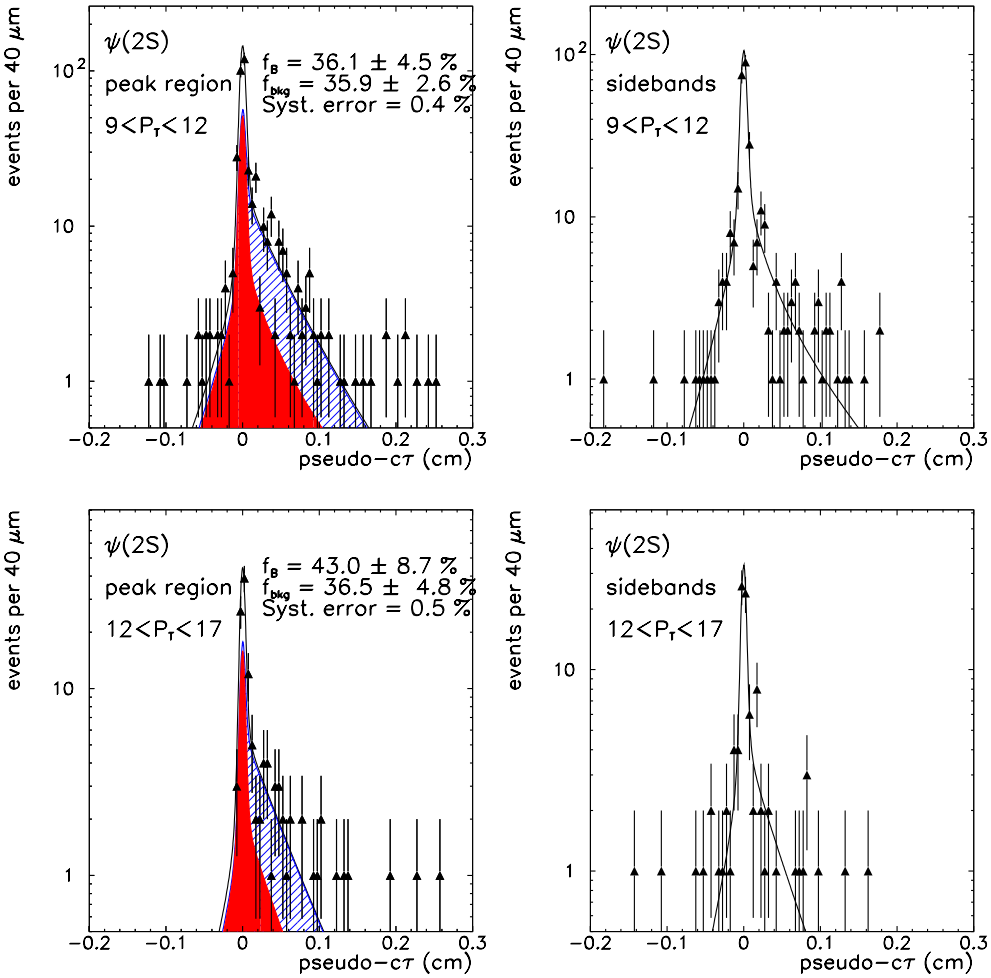

Figure 4-7: The same as Figure 4-4 for the $\psi(2S)$ at high P_T.

$c\tau_0$	average B lifetime
σ	measured error on $c\tau$
ρ	error scale
f_+	fraction of background in the positive exponential
λ_+	lifetime of the positive exponential
f_-	fraction of background in the negative exponential
λ_-	lifetime of the negative exponential
f_{sym}	fraction of background in the symmetric exponential
λ_{sym}	lifetime of the symmetric exponential
f_{tail}	fraction of non-Gaussian tails in resolution function
λ_{tail}	lifetime of non-Gaussian tails in the resolution function

4.1.3 Fitting the Lifetime Distribution

The data is divided into signal and sideband samples based on the dimuon mass in each P_T region. The range of the dimuon mass window for the signal region is chosen to maximize $S^2/(S+B)$, where S(B) are the number of signal (background) events in the mass window. 100 MeV/c^2 regions above and below the mass peak are used as sidebands. The data are fit using an unbinned maximum log-likelihood fit[47] with the following likelihood function:

$$\mathcal{L} = \mathcal{L}_{\text{shape}}^{\text{signal}} \cdot \mathcal{L}_{\text{shape}}^{\text{sideband}} \cdot P(N_{\text{sig}}; N_{\text{sig}}^{\text{fit}}) \cdot P(N_{\text{bkg}}; N_{\text{bkg}}^{\text{fit}}) \tag{4.8}$$

where

$$\mathcal{L}_{\text{shape}}^{\text{signal}} \equiv \left(\prod_{n=1}^{N_{\text{sig}}} [\alpha S(c\tau_n^{\text{sig}}) + (1-\alpha) B(c\tau_n^{\text{sig}})] \right) \tag{4.9}$$

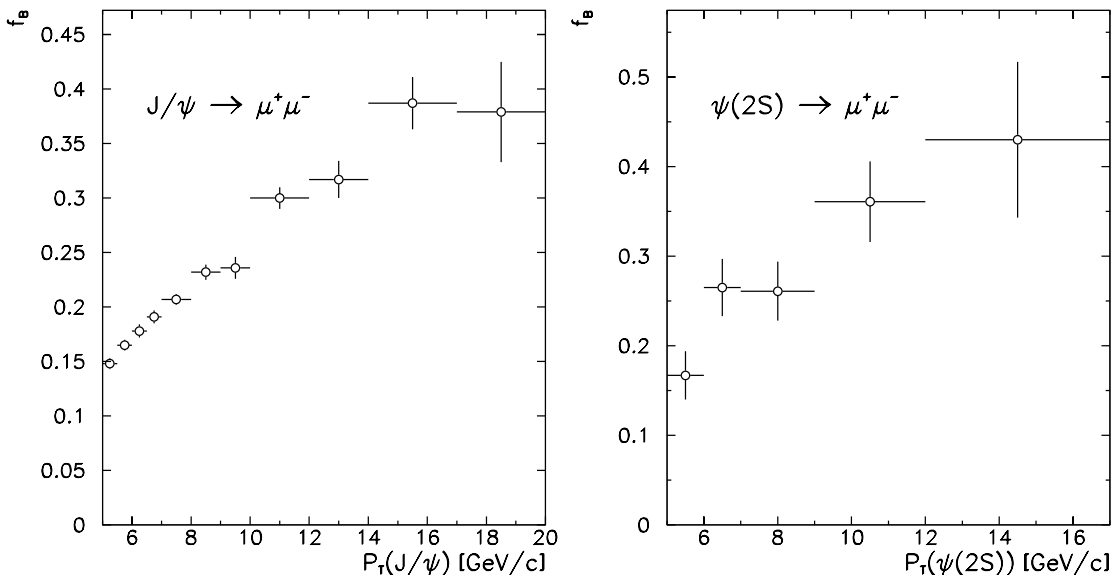

Figure 4-8: The J/ψ(left) and $\psi(2S)$(right) B fraction as a function of $P_T(\psi)$ from fitting the data. The vertical error bars indicate the statistical uncertainty; the horizontal error bars denote the bin width.

is the shape of the signal region, and

$$\mathcal{L}_{\text{shape}}^{\text{sideband}} \equiv \left(\prod_{n=1}^{N_{\text{bkg}}} B(c\tau_n^{\text{bkg}}) \right) \tag{4.10}$$

is the shape of the sideband region.

There are several parameters used in the likelihood function beyond those defined in $c\tau$ parameterizations. N_{sig} is the number of events in the signal region, and N_{bkg} is the number of events in the sideband region, which are determined by counting the number of events in the data. $N_{\text{sig}}^{\text{fit}}(N_{\text{bkg}}^{\text{fit}})$ is the fitted number of events in the signal (sideband) regions. $P(N;\mu)$ is the Poisson probability to observe N events when, on average, μ events are expected. α is the purity of the signal region, defined by

$$\alpha \equiv \frac{N_{\text{sig}}^{\text{fit}} - R \cdot N_{\text{bkg}}^{\text{fit}}}{N_{\text{sig}}^{\text{fit}}} \tag{4.11}$$

where R is a scale factor which corrects for the different widths of the signal and sideband mass windows. $c\tau_n^{\text{sig}}$ ($c\tau_n^{\text{bkg}}$) is the $c\tau$ of the nth candidate in the signal

$P_T(J/\psi)$ (GeV/c)	$f_B(\%)$
5-5.5	14.8 $\pm$ 0.5
5.5-6	16.5 $\pm$ 0.5
6-6.5	17.8 $\pm$ 0.6
6.5-7	19.1 $\pm$ 0.6
7-8	20.7 $\pm$ 0.5
8-9	23.2 $\pm$ 0.7
9-10	23.6 $\pm$ 1.0
10-12	30.0 $\pm$ 1.0
12-14	31.7 $\pm$ 1.7
14-17	38.7 $\pm$ 2.4
17-20	37.9 $\pm$ 4.6

Table 4.1: The B fraction in the J/ψ sample as a function of P_T. The uncertainty is statistical only. There is also a systematic uncertainty of 1.1% of the value for each point.

(sideband) region.

$c\tau_0$ is fixed at 438 μm, the average B lifetime measured using the inclusive J/ψ sample[48]. All other parameters are allowed to vary freely if the fit is able to converge. At high-P_T, there are fewer events, and the fit is unable to converge when all the parameters are allowed to vary. Therefore, the negative tail in the background is removed in the J/ψ fit in the $14 < P_T(\mu^+\mu^-) < 17$ GeV/c bin. This is justified as there are few events at negative $c\tau$, and these are well described by the remaining terms. In the J/ψ fit for $17 < P_T(\mu^+\mu^-) < 20$ GeV/c, the non-Gaussian tails in the resolution function are fixed to be 2% of the resolution function and the symmetric exponential is removed from the background. The tails to the resolution function normally constitute about 2% of the resolution function, and cannot be resolved with the available statistics. For the $\psi(2S)$, the fraction of the non-Gaussian tails in the resolution function cannot be accurately determined, and are fixed to be 2% of the resolution function in every fit.

Figure 4-4, Figure 4-5, Figure 4-6 and Figure 4-7 show the results of some of the fits. The background distributions are well described by the data, indicating that the

$P_T(\psi(2S))$ (GeV/c)	$f_B(\%)$
5-6	16.7 ± 2.7
6-7	26.5 ± 3.2
7-9	26.1 ± 3.3
9-12	36.1 ± 4.5
12-17	43.0 ± 8.7

Table 4.2: The B fraction in the $\psi(2S)$ sample as a function of P_T. The uncertainty is statistical only. There is also a systematic uncertainty of 1.1% of the value for each point.

background parameterization, while lacking a physical justification, does provide an adequate model. The B fractions as a function of P_T are tabulated in Table 4.1 and Table 4.2. They are shown in Figure 4-8. For both modes, the B fraction rises from $\sim 15\%$ at low P_T to $\sim 40\%$ at high P_T.

4.1.4 Quality of the B fraction fits

Several checks are applied to ensure that the fits do indeed describe the data. For each fit, the data is plotted and the fit result are overlaid. This is visually checked to ensure that the fit is accurate, and the χ^2 of each fit is calculated. The χ^2 per degree of freedom, shown in Figure 4-9, is reasonable for all the fits. The pull distributions, defined by (Data − Fit)/Error, are also checked for unusual deviations. Figure 4-10 shows the mean of the pull distribution for each fit. The mean should be zero, and the result is consistent with zero for every fit. Figure 4-11 displays the RMS of the pull distributions, which should be one. 12 of the 16 distribution have an RMS less than 1.1, and the remainder are less than 1.2.

As a further check, a toy Monte Carlo is used to determine the confidence level of the fits.[1] The fit results are used to generate the number of signal and sideband events in each Monte Carlo sample. An error on the $c\tau$ measurement for each event is generated according to the distribution of errors in the data. The error is then

[1]See Appendix A for a more detailed description of toy Monte Carlos.

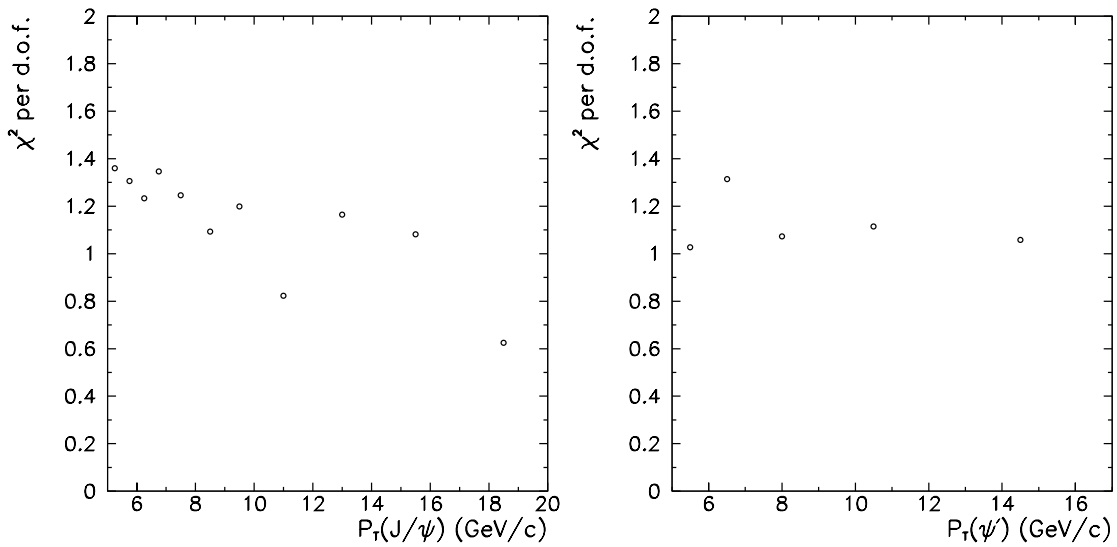

Figure 4-9: χ^2 per degree of freedom for the J/ψ (left) and the $\psi(2S)$ (right) B fraction fits.

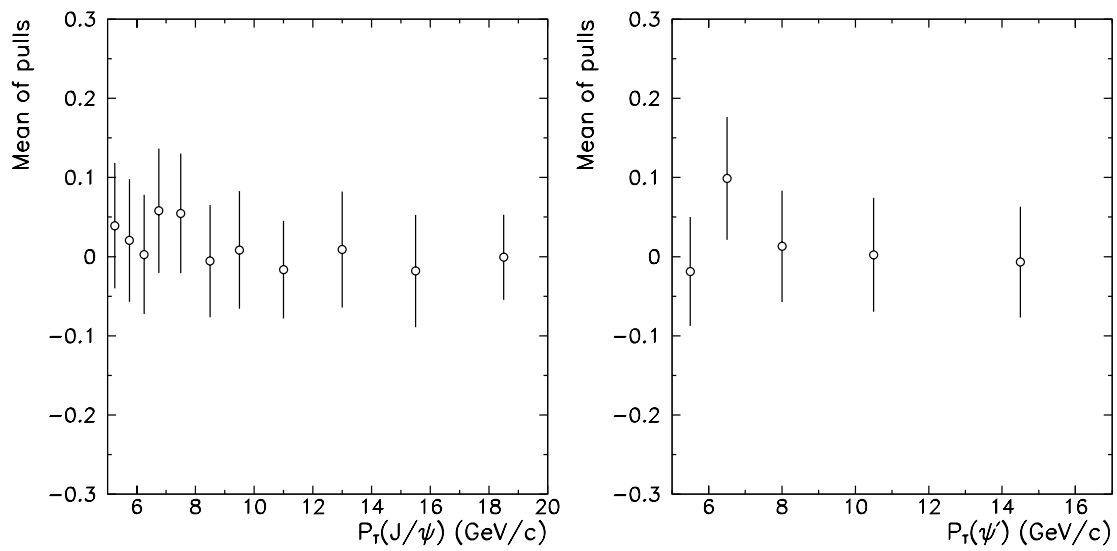

Figure 4-10: Mean of the pull distribution of the J/ψ (left) and the $\psi(2S)$ (right) B fraction fits. The error bars indicate the RMS of the distribution, divided by $\sqrt{N-1}$, where N is the number of bins used to display the fit.

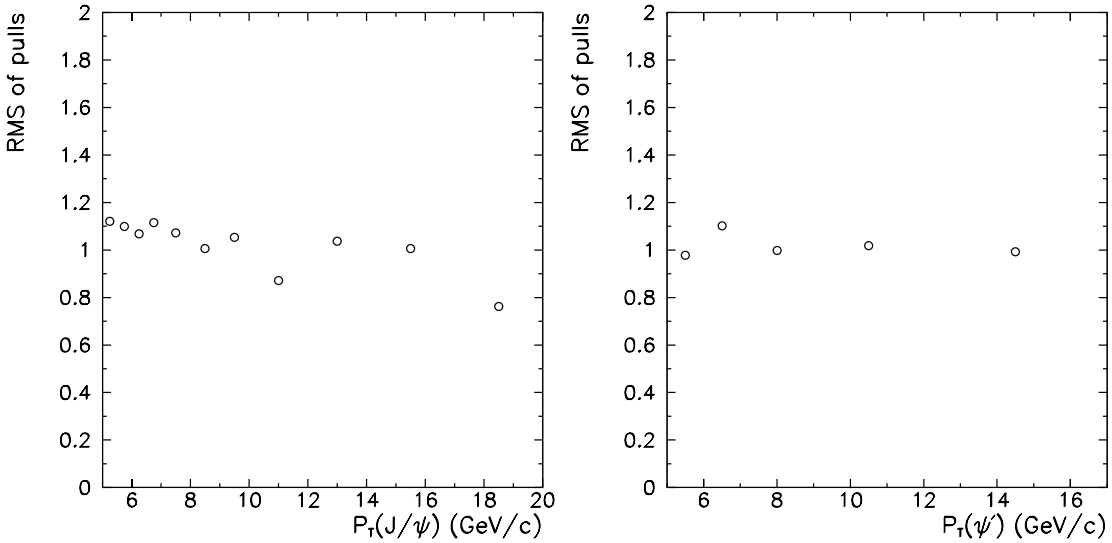

Figure 4-11: RMS of the pull distribution of the J/ψ (left) and the $\psi(2S)$ (right) B fraction fits.

used to generate the value of $c\tau$ for that event. (The error on the value is generated before the value itself because the $c\tau$ probability distribution depends on the error.) 100 Monte Carlo distributions are generated in this manner for each fit, and each distribution is fit with the same code used to fit the data. Using the distribution of the likelihoods obtained from the Monte Carlo fits, a confidence level on the data fit is established. This is shown in Figure 4-12. The confidence level on each fit is acceptable, never falling below 5%. Combined with the other checks, these results provide confidence that the fit is accurately describing the data.

To test if the fits are stable under variations in the fitting technique, the fits are redone with the following variations:

- The mass window is changed so that it is 95% efficient on the signal, based on the shape of the SVX-SVX mass template.
- The window is redefined to be ± 50 MeV/c^2 around the ψ mass
- The average B lifetime is fitted as a free parameter

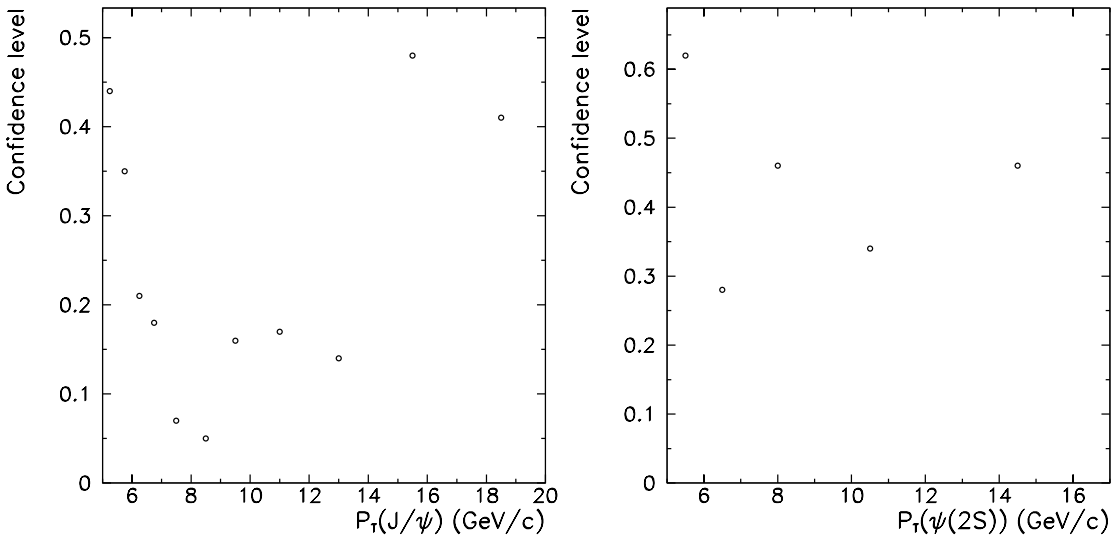

Figure 4-12: Confidence level of the J/ψ (left) and $\psi(2S)$ (right) B fraction fits from the toy Monte Carlo.

Variation	Change in f_B
95% efficient mass window	0.7%
50 MeV/c^2 mass window	3×10^{-4}
Float B lifetime	0.5%
Fit L_{xy} distribution	0.3%
Vertex quality requirements	0.1%
Total	0.9%

Table 4.3: Change in B fraction as the fitting technique is changed

Source	J/ψ	$\psi(2S)$	Ratio
B Fraction Fitting technique	0.9%	0.9%	0.9%
B lifetime	0.7%	0.7%	-
Total	1.1%	1.1%	0.9%

Table 4.4: Systematic uncertainties in the B fraction measurements. All uncertainties are independent of P_T.

- The L_{xy} distribution is fit, instead of the $c\tau$ distribution. Instead of attempting to determine the correct lifetime of the L_{xy} distribution, the lifetime is again allowed to float during the fit.

- Quality requirements are imposed on the vertex. The χ^2 of the SVX fit is required to be less than three per hit, and the error on L_{xy} is required to be less than $30\mu\text{m} \cdot (P_T(\psi)/1 \text{ GeV/c})$.

Figure 4-13 shows the result of the fits divided by the results of the standard fitting method. In all cases, the variations are small compared to the statistical uncertainties. In an effort to decrease the uncertainties in any variation, the ratio is fit to a constant, which is tabulated in Table 4.3. Although the deviations are still not significant, a systematic uncertainty of 0.9%, the sum in quadrature, is assigned to the fitting technique. These are summarized in Table 4.4.

The one external number used in determining the B fraction is the average B lifetime, $c\tau_0$. Raising or lowering $c\tau_0$ by 37 μm (the statistical and systematic uncertainties, added in quadrature) changes the B fraction by 0.7%. This is taken as the systematic uncertainty due to the B lifetime.

All of these checks have two common features. They use the SVX to measure the decay length, and then they use the log-likelihood fit to determine the B fraction. Either of these may introduce systematic effects into the B fraction determination, although there is no known *a priori* reason why they should do so. Testing for possible systematic effects in the SVX requires a method for determining the B content of the sample without using the SVX. One method of doing this is to use the isolation of

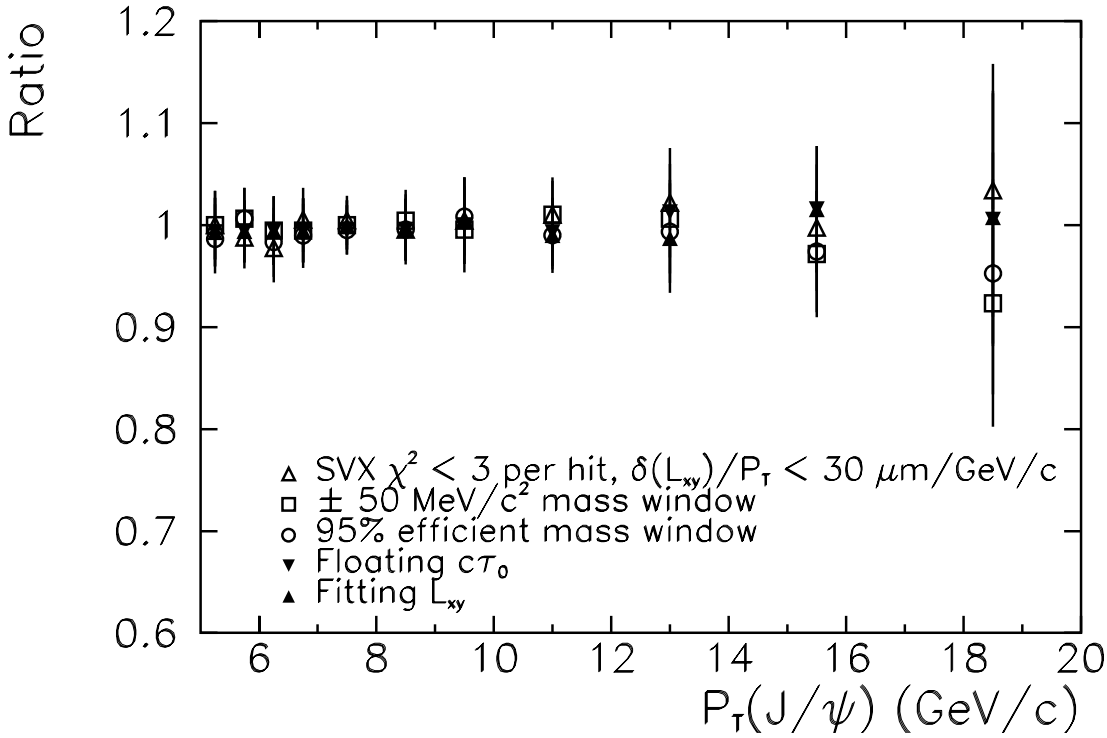

Figure 4-13: Variation in the J/ψ B fraction as a function of P_T for the different fitting methods.

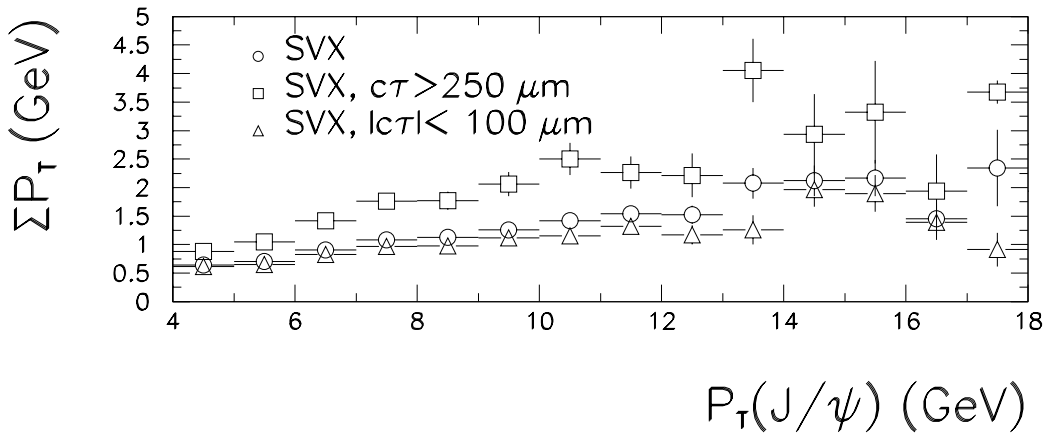

Figure 4-14: Average value of $\sum P_T$ for J/ψ candidates in the SVX, and in B-enriched and B-depleted samples. As expected, the B-enriched sample is less isolated.

the ψ. ψ that are B daughters will be accompanied by the other decay products of the B, while prompt ψ are expected to only be accompanied by particles produced from the fragmentation process or the underlying event. This is studied using the quantity

$$\sum P_T \equiv \sum_i {P_T}^i \tag{4.12}$$

where the index i runs over all reconstructed tracks in a cone of $\Delta R \equiv \sqrt{\Delta\phi^2 + \Delta\eta^2} < 0.4$ around the ψ direction, excluding the two muons. $\sum P_T$ should be larger for B decays than for prompt events. To verify that this is the case, Figure 4-14 shows the $\sum P_T$ distribution for the inclusive J/ψ sample, a B-enriched sample ($c\tau > 250$ μm) and a B-depleted sample ($|c\tau| < 100$ μm). $\sum P_T$ is clearly larger in the B-enriched sample and smaller in the B-depleted sample. While this does make use of the SVX, it is insensitive to systematic effects in the SVX. It only requires that a highly displaced vertex correspond to an increase in the B content. Figure 4-15 compares the $\sum P_T$ distributions for events in the SVX with the same distribution for the entire data set. There is no significant difference between the two distribution. This lack of a

difference, combined with the absence of any reason to believe that the SVX should introduce a bias, leads to the conclusion the the B fraction in the full data set is the fraction extracted by the fit.

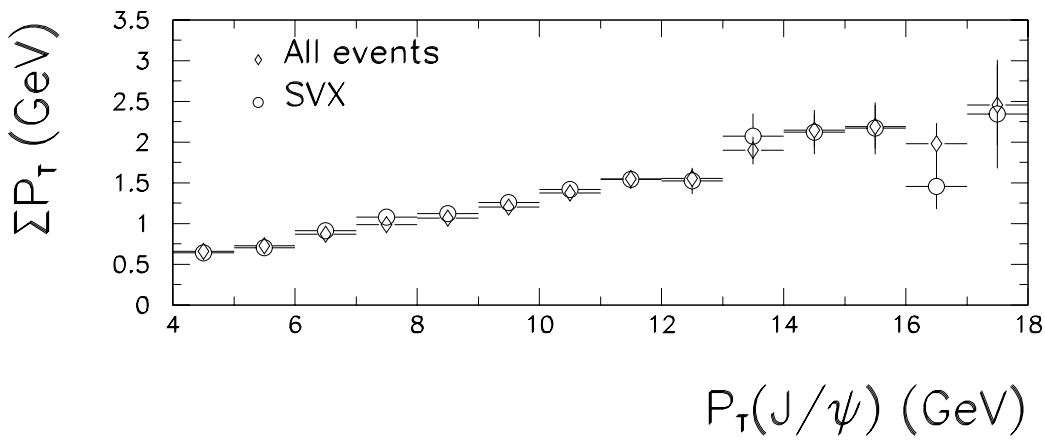

Figure 4-15: Average value of $\sum P_T$ for J/ψ candidates with both muons in the SVX, and for the entire sample. There is no difference between the two distributions, which would be the case if the SVX is introducing a bias.

4.2 $\chi_c \rightarrow J/\psi\gamma$ Fraction

The χ_c component is removed in a statistical manner, by calculating the fraction of J/ψ resulting from χ_c decays as a function of $P_T(J/\psi)$, $F_{\chi_c}^{J/\psi}(P_T(J/\psi))$.[63] The determination of this fraction begins with J/ψ candidates, where the dimuon mass lies in a window around the J/ψ mass. These events are searched for isolated photon candidates detected by the CEM with $E_T > 1$ GeV. The photon and the J/ψ candidate are combined to form the invariant mass difference

$$\Delta M = M(\mu^+\mu^-\gamma) - M(\mu^+\mu^-) \tag{4.13}$$

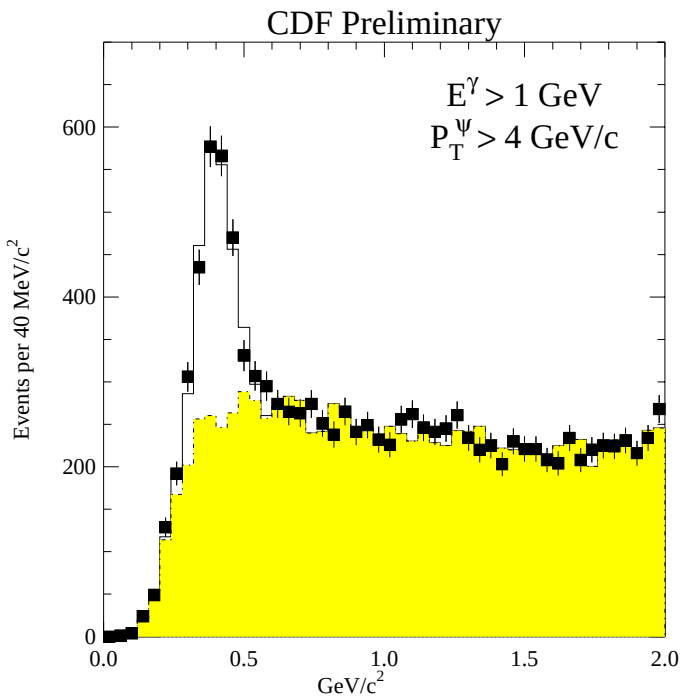

Figure 4-16: Mass difference $m(\mu^+\mu^-\gamma) - m(\mu^+\mu^-)$ for χ_c candidates. The points are the data, and the solid line is the fit to the data of a Gaussian signal plus background. The shaded region is the Monte Carlo background prediction.

The ΔM distribution, shown in Figure 4-16, exhibits a clear peak near ΔM = 400 MeV/c^2, where the χ_c is expected. The resolution is insufficient to resolve the different χ_{cJ} states, but it is sufficient for this analysis to measure the inclusive χ_c fraction.

The peak is near the threshold created by the kinematic cuts, so a simple polynomial background model, such as the one used in fitting the J/ψ mass distribution, will clearly be inadequate. The background shape is derived from a Monte Carlo which includes J/ψ events taken from the data. Excluding the two muons, each charged track in the event is replaced with a π^0, η, or K^0_S. The relative fractions are determined from the measured $K^\pm/\pi^\pm$ and η/π^0 ratios and isospin symmetry. Each particle is decayed, and any photons are simulated using QFL. Running the χ_c reconstruction code on the resulting events produces a ΔM distribution which is used as the background shape. As a cross check, the analysis is repeated using dimuons from the J/ψ sidebands, which contain only background. The shape in this region agrees with the shape obtained from the background Monte Carlo.

The number of χ_c events can now be measured by fitting the data distribution. $F^{J/\psi}_{\chi_c}$ is extracted by

$$F^{J/\psi}_{\chi_c} = \frac{N_{\chi_c}}{N_{J/\psi} \cdot A_\gamma \cdot \epsilon} \tag{4.14}$$

where $N_{\chi_c}(N_{J/\psi})$ is the number of $\chi_c(J/\psi)$ events, A_γ is the acceptance for the photon, once the J/ψ has been found and ϵ is the efficiency of the isolation criteria used in selecting the photon. The photon acceptance is calculated from Monte Carlo, assuming that both the χ_c and the J/ψ decays are unpolarized and includes the efficiency of reconstructing isolated photons. The efficiency of the photon reconstruction is measured using χ_c candidates from a parallel analysis. In that analysis, the photon is not reconstructed using the CEM, but by using the tracking to reconstruct photons which have converted into electron-positron pairs. While the small probability of the photon converting limits the available statistics, this produces a χ_c sample where the photon has been selected using independent criteria. These events are studied to see how often nearby particles in the event would have caused the photon to fail the

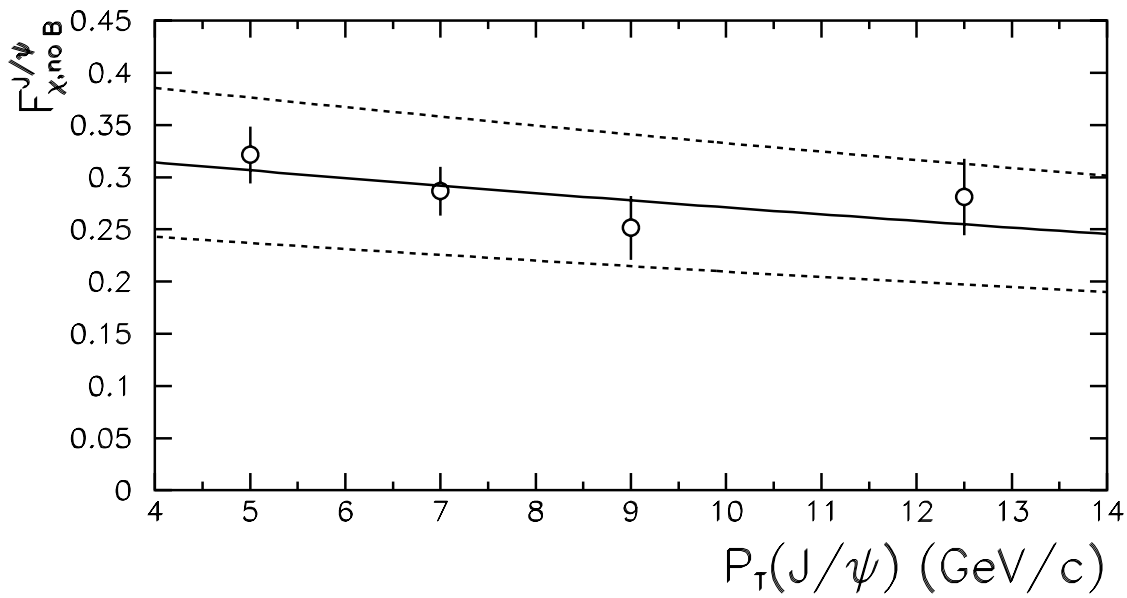

Figure 4-17: $F^{J/\psi}_{\chi_c,\mathrm{no\ B}}$ as a function of P_T. The solid line is the result of fitting the data points to an exponential. The dashed lines represent the systematic uncertainty in the fit value. The error bars indicate the statistical uncertainty.

isolation requirements. The systematic uncertainties on $F^{J/\psi}_{\chi_c}$ are dominated by the efficiency for reconstructing the low-energy photon, the effects of the production and decay models on the acceptance, and the background shape.

The $F^{J/\psi}_{\chi_c}$ described thus far is the fraction from all production modes, including B which decay to charmonium. To remove the B contribution, the χ_c fraction should be calculated by

$$F^{J/\psi}_{\chi_c,\mathrm{no\ B}} = \frac{N_{\chi_c} - N^b_{\chi_c}}{(N_{J/\psi} - N^b_{J/\psi}) \cdot A_\gamma \cdot \epsilon} = F^{J/\psi}_{\chi_c} \cdot \frac{1 - F^{\chi_c}_{\mathrm{B}}}{1 - F^{J/\psi}_{\mathrm{B}}} \tag{4.15}$$

$N^b_{\chi_c}$ ($N^b_{J/\psi}$) is the number of $\chi_c(J/\psi)$ events originating from B decays, and $F^{\chi_c}_{\mathrm{B}}$($F^{J/\psi}_{\mathrm{B}}$) is the fraction of $\chi_c(J/\psi)$ events from B decays. There are not enough χ_c events to determine $F^{\chi_c}_{\mathrm{B}}$ as a function of P_T. However, Monte Carlo studies indicate that the correction factor on the far right-hand side of Equation 4.15 is nearly independent of P_T. The correction is performed by measuring $F^{J/\psi}_{\mathrm{B}}$ and $F^{\chi_c}_{\mathrm{B}}$ in the full sample, and applying the same correction in each bin. The resulting distribution is shown in

Figure 4-17, with a fit to an exponential overlaid.

In the next chapter, these results will be used to extract the cross section from each production mechanism, and to compare those results with the theoretical predictions.

Chapter 5

Comparison with Theoretical Predictions

In this chapter, the cross sections measured in Chapter 3 are combined with the B and χ_c fractions measured in Chapter 4 to extract the cross sections for the different ψ production mechanisms.

The cross section for ψ production via an intermediate B state is given by

$$\frac{d\sigma}{dP_T} \cdot \mathcal{B}(\psi)\bigg|_{\mathrm{B}} = \left(\frac{d\sigma}{dP_T} \cdot \mathcal{B}(\psi)\right) \cdot F_B^{\psi} \tag{5.1}$$

where $\frac{d\sigma}{dP_T} \cdot \mathcal{B}(\psi)$ is the inclusive cross section and F_B^{ψ} is the fraction of ψ events resulting from B decays. All quantities are functions of $P_T(\psi)$. The statistical uncertainties are calculated by adding the fractional statistical uncertainties on the separate measurements in quadrature. The systematic uncertainties are added likewise. The prompt cross sections are calculated similarly:

$$\frac{d\sigma}{dP_T} \cdot \mathcal{B}(\psi)\bigg|_{\mathrm{Prompt}} = \left(\frac{d\sigma}{dP_T} \cdot \mathcal{B}(\psi)\right) \cdot (1 - F_B^{\psi}) \tag{5.2}$$

The direct ψ cross sections are extracted by removing the χ_c contribution from the prompt cross section. Since there is no χ_c feeddown into the $\psi(2S)$, the prompt and

direct cross sections are the same for that state. With $F^{J/\psi}_{\chi_c,\text{no B}}$ being the fraction of the prompt ψ which are produced by χ_c decays, the direct cross sections are calculated by

$$\left.\frac{d\sigma}{dP_T}\cdot\mathcal{B}(J/\psi)\right|_{\text{Direct}} = \left(\frac{d\sigma}{dP_T}\cdot\mathcal{B}(J/\psi)\right)\cdot(1-F^{J/\psi}_{\text{B}})\cdot(1-F^{J/\psi}_{\chi_c,\text{no B}}) \quad (5.3)$$

$$\left.\frac{d\sigma}{dP_T}\cdot\mathcal{B}(\psi(2S))\right|_{\text{Direct}} = \left.\frac{d\sigma}{dP_T}\cdot\mathcal{B}(\psi(2S))\right|_{\text{Prompt}} \quad (5.4)$$

After describing how theoretical predictions for these results are obtained, the predictions will be compared with the data.

5.1 Monte Carlo Simulation

Monte Carlo simulations form an important part of any analysis. This is especially true in a cross section analysis, where the acceptance of the detector must be understood in order to relate the observed number of events to the cross section.

5.1.1 Event Generation

This analysis makes use of two event generators. The first, `BGENERATOR`, is a b-quark generator.[49] The second, `JGENONLY`, generates ψ events directly, without specifying the production model.

`BGENERATOR`

`BGENERATOR` generates an event containing a single b quark, according to the P_T and rapidity distributions of [50]. The b quark is generated with $P_T(b) > P_T(\text{min})$ and $y_{\text{min}} < y(b) < y_{\text{max}}$, where $P_T(\text{min})$, y_{min} and y_{max} are parameters controlled by the user. MRSD0 and MRSD- structure functions[51] are available, and the renormalization scale and the b quark mass can be set. The b quark is fragmented in B^+, B^0, B_s or Λ_b using Petersen fragmentation[14], where the fragmentation parameter z is

defined as

$$z \equiv \frac{E_{\mathrm{B}} + P_{\mathrm{B}}^{\parallel}}{E_b + P_b} \tag{5.5}$$

E_{B} is the energy of the B hadron, $P_{\mathrm{B}}^{\parallel}$ is the momentum of the B hadron parallel to the momentum of the b quark, E_b is the energy of the b quark and P_b is the momentum of the b quark. This process can violate energy conservation, in the sense that it is possible to obtain $E_{\mathrm{B}} > E_b$. If this occurs, a new value of z is generated. This creates a region of phase space ($P_T(b)$ and $y(b)$ both near zero) where the fragmentation process cannot terminate, because $E_b < m_{\mathrm{B}} \leq E_{\mathrm{B}}$. If this is detected by the fragmentation restarting a large number of times, the b quark momentum is regenerated, effectively removing a portion of the available phase space, as shown in Figure 5-1. Once this portion of the fragmentation succeeds, the B hadron is given momentum perpendicular to the b quark direction. The direction is selected uniformly, and the magnitude is given by

$$P_{\perp} = \frac{16}{3\pi}\sqrt{r^{-1/3} - 1}\,(350 \text{ MeV/c}) \tag{5.6}$$

where r is a random number uniformly distributed between 0 and 1. The distribution is has a mean value of 350 MeV/c and an RMS of 233 MeV/c ($\frac{2}{3}$ the mean value).

When `BGENERATOR` finishes generating events, it reports the theoretical cross section corresponding to the generation constraints. As noted above, the fragmentation procedure removes a portion of the b quark phase space. The cross section calculation does not take this into account, and will be inaccurate if the generation parameters do not exclude this region. For that reason, all the `BGENERATOR` Monte Carlo samples used in this analysis are generated with $P_T(\min) > 3$ GeV/c and $|y(b)| < 1$, which excludes the affected region. This does not affect the ψ P_T spectrum, as ψ with $P_T(\psi) > 5$ GeV/c are not produced by b quarks with $P_T(b) < 3$ GeV/c.

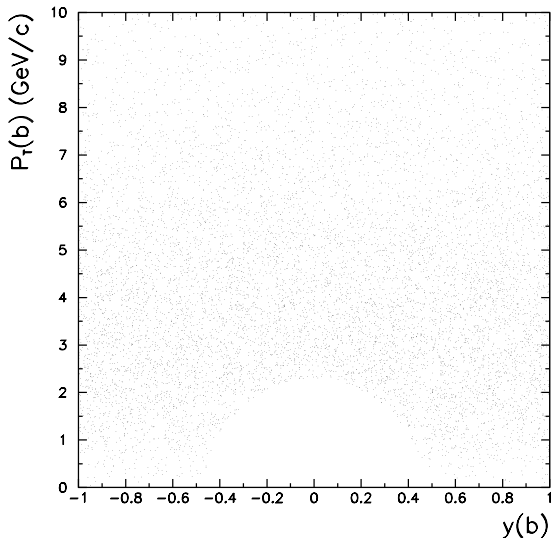

Figure 5-1: Transverse momentum versus rapidity of the b quark for BGENERATOR events with successful fragmentation.

JGENONLY

Early in this analysis, it became obvious that the Color Singlet Model and the B Production Model were insufficient to explain the $\psi(2S)$ cross section. Rather than developing a ψ generator which implements a particular production model, a generator was developed which uses a flat P_T spectrum. As various models are introduced, it is possible to apply that model by weighting each event in the already generated and simulated Monte Carlo sample, rather than using the much slower process of generating a new Monte Carlo data set and running the detector simulation. JGENONLY is such a generator, which generates events containing only a ψ. The transverse momentum of the ψ is uniformly distributed between $P_T(\text{min})$ and $P_T(\text{max})$; the pseudorapidity of the ψ is uniformly distributed with $\eta_{\text{min}} < \eta(\psi) < \eta_{\text{max}}$. The azimuthal angle of the ψ is generated from a uniform distribution between 0 and 2π.

It should be noted that both of the generators produce only the particles being studied. There are no additional particles produced from fragmentation, and the underlying event is completely ignored. Any other particles produced by the hard

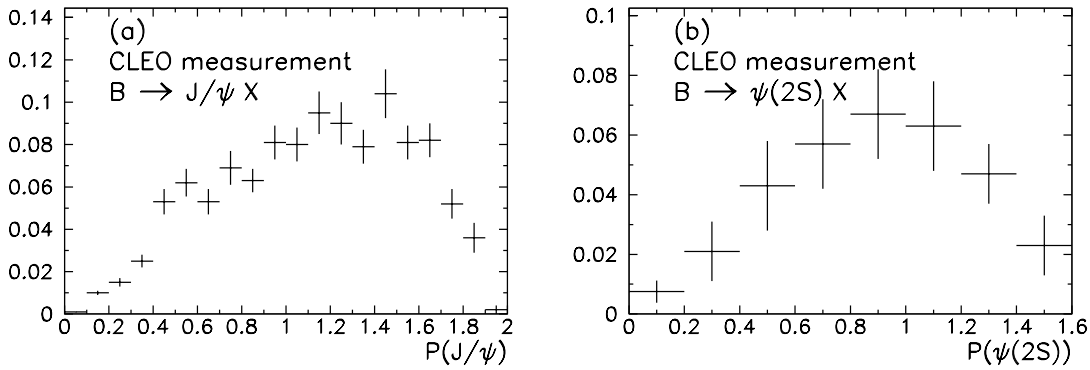

Figure 5-2: The (a) J/ψ and (b) $\psi(2S)$ momentum distributions in the CLEO lab frame.

scattering are also missing. At the very least, there will be another particle to recoil against the produced b or ψ. While these generators will model the physics being studied, they will not model the environment of the event, such as the isolation of the ψ.

5.1.2 Particle Decay Simulation

There are three decays which need to be modeled for this analysis: B$\rightarrow\psi$X, $\psi\rightarrow\mu^+\mu^-$ and $\psi(2S)\rightarrow J/\psi\pi\pi$. For the B$\rightarrow\psi$X decay, rather than modeling each decay mode, an inclusive decay model is developed, based on the ψ momentum spectrum in inclusive B decays measured at CLEO.[27] The remaining decays are modeled using the QQ Monte Carlo, developed at CLEO.

B$\rightarrow\psi$X

The B is forced to decay to a ψ with a momentum distribution parameterized from inclusive measurements by CLEO,[27] and corrected for the boost of the B meson in the CLEO lab frame. The ψ momentum spectra in the CLEO lab frame are shown in Figure 5-2. The ψ direction is assumed to be uniform in the B rest frame. The branching ratios used are $\mathcal{B}$(B$\rightarrow J/\psi$X) $= 1.13 \pm 0.07\%$,[27] $\mathcal{B}(J/\psi\rightarrow\mu^+\mu^-) = 5.9 \pm$

0.25%,[45] $\mathcal{B}(\mathrm{B}\to\psi(2S)\mathrm{X}) = 0.34\pm0.05\%$[27] and $\mathcal{B}(\psi(2S)\to\mu^+\mu^-) = 0.77\pm0.17\%$[6].

The decays $\mathrm{B}^\pm\to J/\psi\mathrm{K}^\pm$ and $\mathrm{B}^0\to J/\psi\mathrm{K}^*$ are dealt with separately. In the B rest frame, the momentum distribution for a given two body decay is a delta function. When boosting to the CLEO lab frame, this distribution spreads out, depending on the angle between the B and ψ momenta. The correction for the CLEO boost is correct on average, but individual events are distributed about the correct value. The momentum distributions of the J/ψ in the CLEO lab frame has been measured for the decays $\mathrm{B}^\pm\to J/\psi\mathrm{K}^\pm$ and $\mathrm{B}^0\to J/\psi\mathrm{K}^*$.[27] These distributions are subtracted from the J/ψ momentum distribution used to generate the J/ψ momentum. For each mode, the appropriate fraction $(f_{\mathrm{K}^\pm}, f_{\mathrm{K}^*})$ of the events are decayed into the given two-body modes, where

$$f_{\mathrm{K}^\pm} = \frac{\mathcal{B}(\mathrm{B}^\pm\to J/\psi\mathrm{K}^\pm)}{\mathcal{B}(\mathrm{B}\to J/\psi\mathrm{X})} \tag{5.7}$$

$$f_{\mathrm{K}^*} = \frac{\mathcal{B}(\mathrm{B}^0\to J/\psi\mathrm{K}^*)}{\mathcal{B}(\mathrm{B}\to J/\psi\mathrm{X})} \tag{5.8}$$

While only B_u and B_d mesons are produced at CLEO interaction region, the CDF data also contain B_s, B_c and Λ_b events. This model ignores B_c production, as B_c production is expected to be about 10^{-3} of the total B hadron production rate.[52] The c quark in the initial state will enhance the branching ratio to charmonium, but B_c production is expected to account for $\lesssim 1\%$ of all B to ψ events.[53] Currently, there is no measurement of the ψ momentum distribution in B_s and Λ_b decays. To model the decay of these particles, it is assumed that the momentum spectrum in the B_s or Λ_b rest frame has the same shape as for the lighter B mesons but that the momentum scale is different. The ψ momentum is generated identically for all the parents, assuming the parent is a B^0. After moving to the B rest frame, the ψ momentum is scaled by $P \Rightarrow P \cdot P_{\mathrm{max}}(\mathrm{B})/P_{\mathrm{max}}(\mathrm{B}^0)$. P_{max} is the momentum of the ψ in the B rest frame for the two-body decay mode where the other particle, X, is the lightest particle for which the decay is not suppressed, *e.g.*, $\mathrm{B}^\pm\to\psi\mathrm{K}^\pm$, $\mathrm{B}^0\to\psi\mathrm{K}^0$,

$B_s \to \psi\phi$, and $\Lambda_b \to \psi\Lambda$. Using conservation of energy, it is simple to show that

$$P_{\max}(\mathrm{B}) = \frac{\sqrt{m_{\mathrm{B}}^4 + (m_\psi^2 - m_{\mathrm{X}}^2)^2 - 2m_{\mathrm{B}}^2(m_\psi^2 + m_{\mathrm{X}}^2)}}{2m_{\mathrm{B}}} \tag{5.9}$$

The ψ decay model presents a source of systematic error in the B to ψ cross section prediction. However, this turns out to be very small compared with the uncertainties in the B hadron cross section, discussed below. The reason is that the effect of boosting the ψ from the B rest frame to the CDF lab frame washes out most of the effects of the ψ momentum in the rest frame. When a J/ψ is produced in the B rest frame, it has less than 1.8 GeV/c of momentum, or $\beta\gamma < 0.6$. (For the $\psi(2S)$, $\beta\gamma < 0.4$.) Almost all the B parents for which the ψ is reconstructed at CDF have $P_T > 8$ GeV/c, or $\beta\gamma > 1.5$. When the ψ is boosted from the B center of mass frame to the lab frame, the boost from the B is at least as important as the initial ψ momentum. Furthermore, the ψ momentum distribution is constrained by the CLEO measurement, so only small variations in the momentum spectrum are allowed. Still, several different checks are performed to quantify the size of this uncertainty.

One source of uncertainty is the ψ momentum spectrum measured by CLEO. Since the spectrum is used as a probability distribution, changes in the normalization do not affect the model; only the shape is important. To measure the effect of the uncertainty on the shape, the value at each point (σ_n) is varied according to its error (δ_n) by

$$\sigma_n \Rightarrow \sigma_n \pm \frac{n - N/2}{N/2}\delta_n \tag{5.10}$$

where N is the number of points measured and $n = 1, 2, \ldots, N$. The new distributions are parameterized, and used to redecay the same Monte Carlo sample of B events used to calculate the central value of the predicted cross section.

To be certain that performing the two-body decays separately is not biasing the prediction, the calculation is performed in two different manners. First, the $J/\psi K^\pm$ and $J/\psi K^*$ decays are not removed from the inclusive distribution. As a second check, the B_s and Λ_b are decayed to $J/\psi\phi$ and $J/\psi\Lambda$ assuming the same branching

ratios as B^0 to $J/\psi K^*$. This is reasonable, as both decays are color suppressed, and similar Feynman diagrams are involved. Furthermore, all are pseudo-scalar to vector–vector decays. The effect of scaling the momentum spectrum for the heavier mesons is tested by assuming the ψ is recoiling against a massless particle when calculating P_{max}. In all cases, the prediction changes by only a few percent, which is completely insignificant compared to the uncertainties from variations in the renormalization scale, the Petersen fragmentation parameter and the b quark mass.

QQ

The remainder of the decays are performed using the QQ Monte Carlo, version 9.0, developed at CLEO and adapted for use within the CDF framework by Jonathan Lewis. QQ will decay the input particles to the specified final states. For the $\psi \to \mu^+\mu^-$ decays, leading order radiative corrections, including the emission of hard photons, are included.

5.1.3 Detector Simulation

The CDF detector simulation used here, "QFL," is a high-level simulator, in that it does not create raw data, but directly produces the data structures used by physics analyses. There is also a detector simulation which performs a low-level simulation (CDFSIM), but it is much slower, and is not used by this analysis.

QFL models the detector by propagating the generated particles through the detector. The z of the event vertex is distributed according to a Gaussian distribution, with a user-specified mean and width. A particle experiences energy loss due to ionization and is deflected by multiple Coulomb scattering whenever it passes through material. In the CTC, individual hits are not generated; rather, a reconstructed track is generated using the resolution of the CTC. For particles which pass through the SVX and/or the CMU, hits are generated, with their positions smeared by the detector resolution and by multiple scattering effects. The standard offline reconstruction code is then used to link the CTC tracks with the SVX and CMU hits.

5.2 B Production

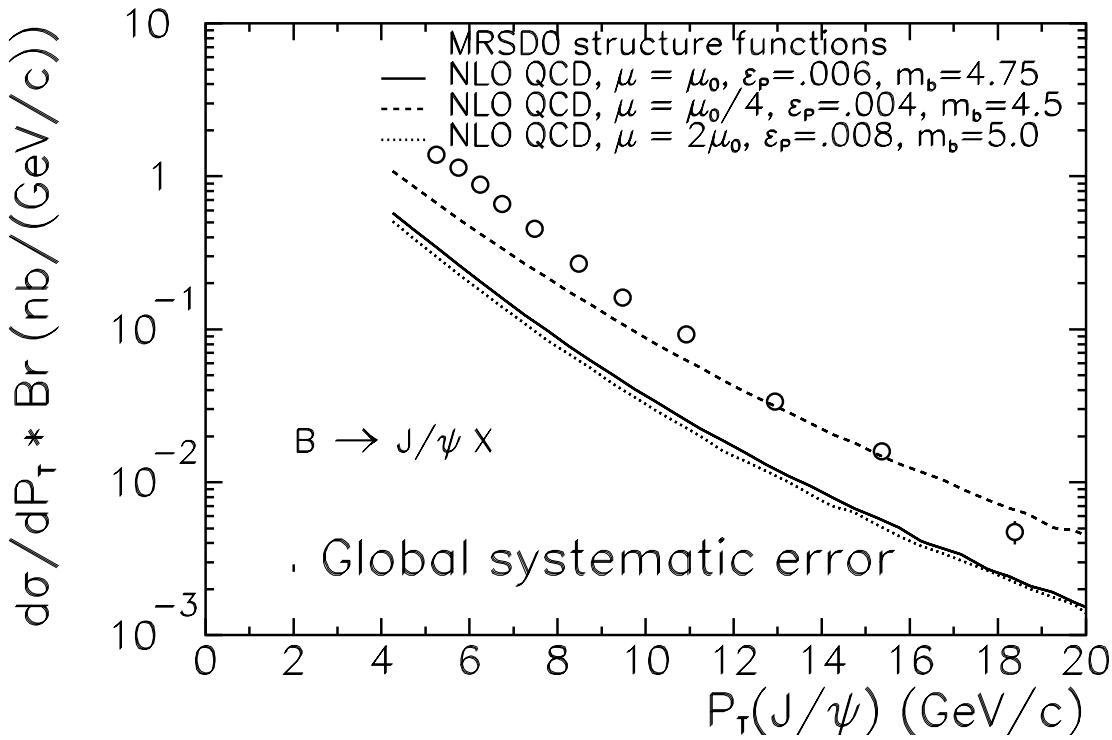

Figure 5-3: J/ψ differential cross sections from B production, compared with expectations. The data points are plotted at the location where the central theory curve has its average value.

The cross sections for J/ψ and $\psi(2S)$ production from B decays are shown in Figure 5-3 and Figure 5-4. The results are tabulated in Table 5.1 and Table 5.2. Also shown in the figures are the theoretical predictions for the ψ from B cross sections; these are calculated by generating b quarks according to the NLO QCD predictions[50], using the renormalization scale $\mu = \mu_0 \equiv \sqrt{m_b^2 + {P_T}^2}$ and the b quark mass $m_b = 4.75$ GeV/c. The b quark is fragmented into B_u, B_d and B_s mesons and Λ_b baryons using Petersen fragmentation[14] in a 37.5 : 37.5 : 15 : 10 ratio with the Petersen fragmentation parameter, ϵ_P, set to 0.006. The B is decayed to a ψ using the model described in Section 5.1.

There are several sources of uncertainty in the predicted $b \rightarrow \psi$ rates beyond those

$P_T(J/\psi)$(GeV/c)	$\frac{d\sigma}{dP_T} \cdot \mathcal{B}$ (10^{-3}nb/GeV/c)
5-5.5	1380 ± 150
5.5-6	1140^{+110}_{-120}
6-6.5	881^{+85}_{-90}
6.5-7	658^{+60}_{-65}
7-8	452^{+39}_{-42}
8-9	269^{+23}_{-25}
9-10	162 ± 15
10-12	$92.9^{+7.8}_{-8.1}$
12-14	$33.6^{+3.5}_{-3.4}$
14-17	$16.0^{+1.8}_{-1.7}$
17-20	$4.74^{+0.85}_{-0.84}$

Table 5.1: The differential J/ψ cross section from B production, as a function of P_T, for $|\eta(\psi)| < 0.6$. The errors are the statistical and systematic errors added in quadrature.

$P_T(\psi(2S))$(GeV/c)	$\frac{d\sigma}{dP_T} \cdot \mathcal{B}$ (10^{-3} nb/GeV/c)
5-6	43 ± 9
6-7	29 ± 6
7-9	17 ± 3
9-12	6.2 ± 1.2
12-17	1.8 ± 0.5

Table 5.2: The differential $\psi(2S)$ cross sections from B production, as a function of P_T, for $|\eta(\psi)| < 0.6$. The errors are the statistical and systematic errors added in quadrature.

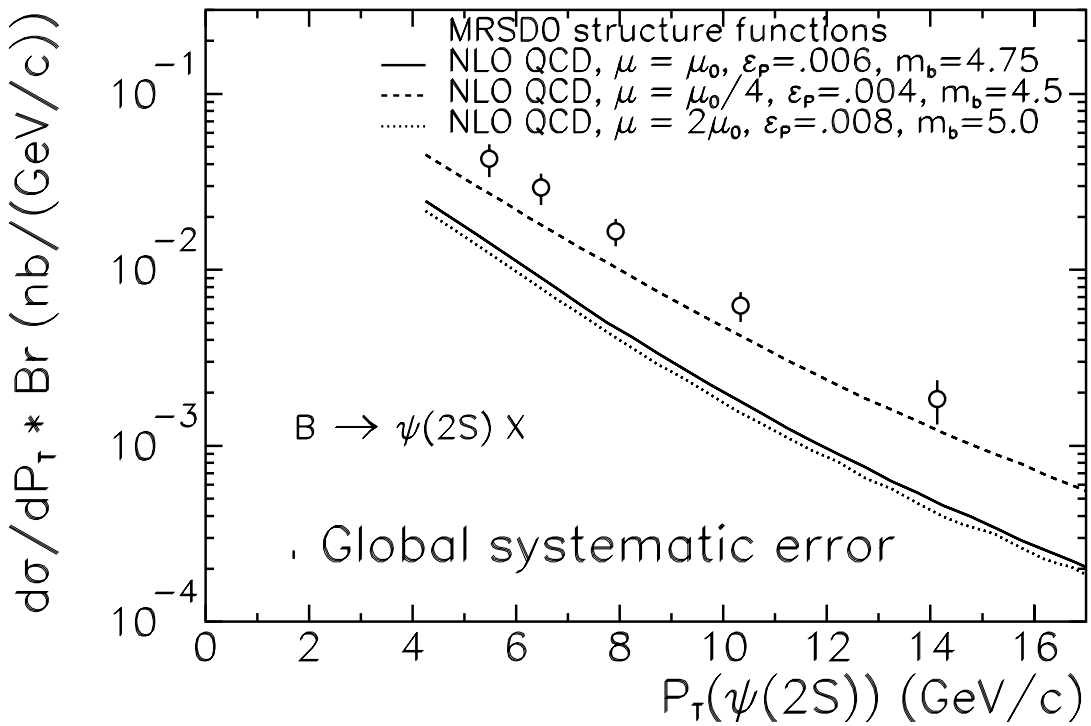

Figure 5-4: $\psi(2S)$ differential cross sections from B production, compared with expectations. The data points are plotted at the location where the central theory curve has its average value.

in the ψ decay model. The cross section for b quark production depends on the values chosen for μ and m_b. To obtain an upper variation, μ is lowered from μ_0 to $\mu_0/4$ and the b quark mass is lowered from 4.75 GeV/c to 4.5 GeV/c.[54] The ψ cross section also depends on the fragmentation of the b quark, so ϵ_P is lowered from 0.006 to 0.004. A lower variation is produced by setting μ to $2\mu_0$, the b quark mass to 5.0 GeV/c and ϵ_P to 0.008. As may be seen in Figure 5-3 andd Figure 5-4, the data falls substantially above the nominal calculation. The J/ψ upper variation is consistent with the data at large P_T, but is lower than the data at small values of P_T. The $\psi(2S)$ upper variation is always below the data, although at large P_T, the discrepancy is only about 1σ. The nominal J/ψ predictions are a factor of 2-4 below the data, while the $\psi(2S)$ predictions are a factor of 3-4 low.

The integrated ψ cross sections from B production, multiplied by the branching ratios, are

$$\sigma(J/\psi, \mathrm{B}) \cdot \mathcal{B}(J/\psi \to \mu^+\mu^-) = 3.23 \pm 0.05(\mathrm{stat})^{+0.28}_{-0.30}(\mathrm{sys})\ \mathrm{nb} \tag{5.11}$$

$$\sigma(\psi(2S), \mathrm{B}) \cdot \mathcal{B}(\psi(2S) \to \mu^+\mu^-) = 0.13 \pm 0.01(\mathrm{stat}) \pm 0.01(\mathrm{sys})\ \mathrm{nb} \tag{5.12}$$

where

$$\sigma(\psi, \mathrm{B}) = \sigma(\mathrm{p\overline{p}} \to \psi \mathrm{X}, P_T(\psi) > 5\ \mathrm{GeV/c}, |\eta(\psi)| < 0.6) \tag{5.13}$$

proceeding through an intermediate B state. This can be compared to the predicted values of

$$\sigma(J/\psi, \mathrm{B}) \cdot \mathcal{B}(J/\psi \to \mu^+\mu^-) = 0.82(1.76)\ \mathrm{nb} \tag{5.14}$$

$$\sigma(\psi(2S), \mathrm{B}) \cdot \mathcal{B}(\psi(2S) \to \mu^+\mu^-) = 0.04(0.09)\ \mathrm{nb} \tag{5.15}$$

where the value in parentheses is the upper variation. The integrated cross sections are a factor of 3-4 higher than the predicted values. Given the disagreement in the differential cross sections, this is not surprising, as the integrated cross sections are dominated by the low P_T differential cross sections.

While what is actually measured is the cross section multiplied by the branching ratio, dividing by the branching ratios given earlier allows a comparison where the normalization is expected to be similar. Doing so yields

$$\sigma(J/\psi, \mathrm{B}) = 4840 \pm 70(\mathrm{stat})^{+420}_{-450}(\mathrm{sys}) \pm 360(\mathcal{B})\ \mathrm{nb} \tag{5.16}$$

$$\sigma(\psi(2S), \mathrm{B}) = 5000 \pm 400(\mathrm{stat}) \pm 400(\mathrm{sys}) \pm 1300(\mathcal{B})\ \mathrm{nb} \tag{5.17}$$

where the last error is due to the uncertainty in the branching ratios. The theoretical predictions are

$$\sigma(J/\psi, \mathrm{B}) = 1230(2637)\ \mathrm{nb} \tag{5.18}$$

$$\sigma(\psi(2S), \mathrm{B}) = 1559(3294)\ \mathrm{nb} \tag{5.19}$$

The larger $\psi(2S)$ mass means that the $\psi(2S)$ takes a larger fraction of the parent momentum (on average) than the J/ψ, resulting in a 27% larger predicted rate for $\psi(2S)$ production with $P_T(\psi) > 5$ GeV/c, compared to the J/ψ. While the $\psi(2S)$ cross section is larger than the J/ψ cross section, it is not 27% larger. However, the statistical error and the uncertainty on the branching ratios, which are entirely uncorrelated, are more than large enough to cover the difference.

5.3 Direct Production

Early predictions for direct ψ production were done at lowest order in α_S, and only considered diagrams where the $c\bar{c}$ pair is formed in a color singlet state.[20, 21] After experimental results indicated possible disagreement with the shape at large transverse momentum[55, 56], Braaten and Yuan[57] realized that fragmentation diagrams would dominate the cross section at high P_T, even though those diagrams are higher order in α_S. These two contributions, when taken together, constitute the Color Singlet Model (CSM).

5.3.1 Color Singlet Model

The comparison of the data with the CSM is straightforward, as there are no undetermined parameters beyond the usual scale parameters. Figure 5-5 shows the direct J/ψ and $\psi(2S)$ cross sections along with the CSM predictions.[58] The calculation uses the MRSD0 structure function[51] and the renormalization, factorization and fragmentation scales are set to $P_T/2$. The CSM fails horribly, as the data exceeds the predicted rates by factors of 50 to 100! This stark disagreement between the two predictions is the "CDF $\psi(2S)$ anomaly."[1]

[1]It is called the $\psi(2S)$ anomaly and not the ψ anomaly for historical reasons. When this result was first presented, the χ_c content in the J/ψ sample was poorly known.[59] The J/ψ cross section could be explained by a large χ_c fraction, but there was no explanation for the excess $\psi(2S)$ production. So while the anomaly existed in both the J/ψ and the $\psi(2S)$, it was apparent only in the $\psi(2S)$.

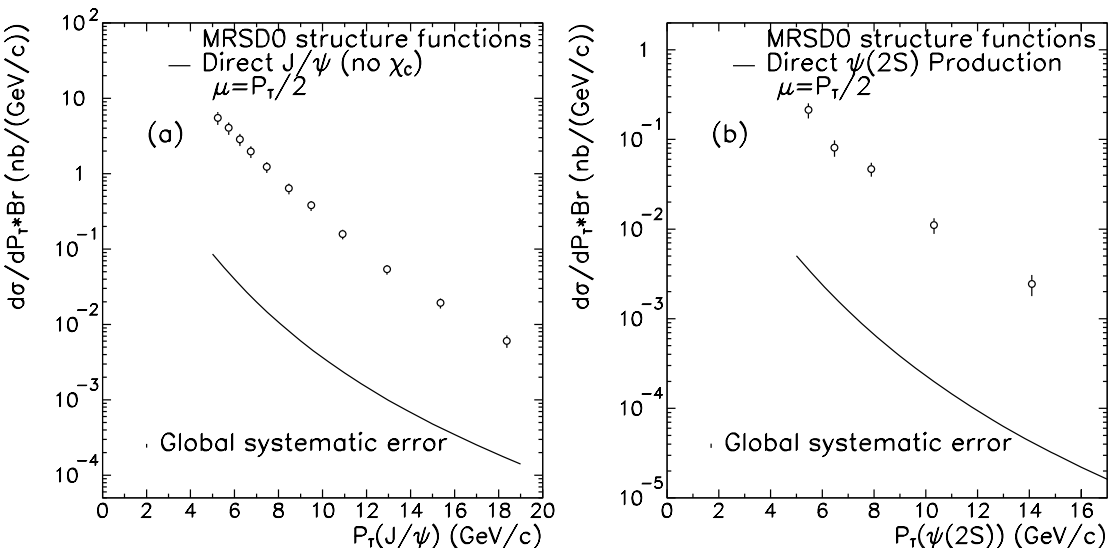

Figure 5-5: Direct J/ψ (a) and $\psi(2S)$ (b) cross sections, compared with the CSM. The χ_c contribution to the J/ψ cross section has been removed. The solid curves are the CSM predictions. The vertical error bars are the statistical and P_T-dependent uncertainties, added in quadrature. The points are plotted at the position where the prediction has its average value in the bin.

The integrated cross sections times branching ratio are

$$\sigma(J/\psi, \text{direct}) \cdot \mathcal{B}(J/\psi \rightarrow \mu^+\mu^-) = 9.95 \pm 0.08(\text{stat})^{+1.8}_{-1.9}(\text{sys}) \text{ nb} \tag{5.20}$$

$$\sigma(\psi(2S), \text{direct}) \cdot \mathcal{B}(\psi(2S) \rightarrow \mu^+\mu^-) = 0.43 \pm 0.03(\text{stat})^{+0.06}_{-0.07}(\text{sys}) \text{ nb} \tag{5.21}$$

where

$$\sigma(\psi, \text{direct}) = \sigma(\text{p}\overline{\text{p}} \rightarrow \psi \text{X}, P_T(\psi) > 5 \text{ GeV/c}, |\eta(\psi)| < 0.6) \tag{5.22}$$

for direct production. These values dwarf the CSM predictions of

$$\sigma(J/\psi, \text{direct}) \cdot \mathcal{B}(J/\psi \rightarrow \mu^+\mu^-) = 0.113 \text{ nb} \tag{5.23}$$

$$\sigma(\psi(2S), \text{direct}) \cdot \mathcal{B}(\psi(2S) \rightarrow \mu^+\mu^-) = 0.0068 \text{ nb} \tag{5.24}$$

Dividing out the branching ratio, we have

$$\sigma(J/\psi, \text{direct}) = 169 \pm 1(\text{stat})^{+31}_{-32}(\text{sys}) \pm 7(\mathcal{B}) \text{ nb} \tag{5.25}$$

$$\sigma(\psi(2S), \text{direct}) = 49 \pm 3(\text{stat})^{+7}_{-8}(\text{sys}) \pm 7(\mathcal{B}) \text{ nb} \tag{5.26}$$

which is a factor of 90 (60) above the CSM predictions for the $J/\psi(\psi(2S))$ cross sections:

$$\sigma(J/\psi, \text{direct}) = 1.91 \text{ nb} \tag{5.27}$$

$$\sigma(\psi(2S), \text{direct}) = 0.77 \text{ nb} \tag{5.28}$$

The J/ψ direct cross section is a factor of 3.5 larger than the direct $\psi(2S)$ cross section. The J/ψ cross section does include feeddown from the $\psi(2S)$. However, the J/ψ will be softer than the $\psi(2S)$ because of the energy taken by the other decay particles. This, combined with the rapidly falling P_T spectrum and the branching ratio, means that only about 20% of the $\psi(2S)$ cross section feeds into the J/ψ cross section. Any theory which describes charmonium production must also predict that J/ψ production is about a factor of three larger than $\psi(2S)$ production.

Clearly, the CSM fails to describe direct production of charmonium at the Tevatron. In an attempt to explain this discrepancy, new calculations were performed, using the Color Octet Model (COM), where the $c\bar{c}$ pair is produced in a color octet state, and sheds the unwanted color during the fragmentation process.

5.3.2 Color Octet Model

As described in Chapter 1, the Color Octet Model (COM) attempts to resolve this anomaly. Unlike the CSM, the COM can only predict the shape of the cross section, which is multiplied by a non-perturbative matrix element describing the fragmentation of the color octet $c\bar{c}$ state into the color singlet ψ or χ_c. The COM does provide an order of magnitude estimate for the normalization, which limits the number of additional diagrams which need to be considered. In the case of direct ψ produc-

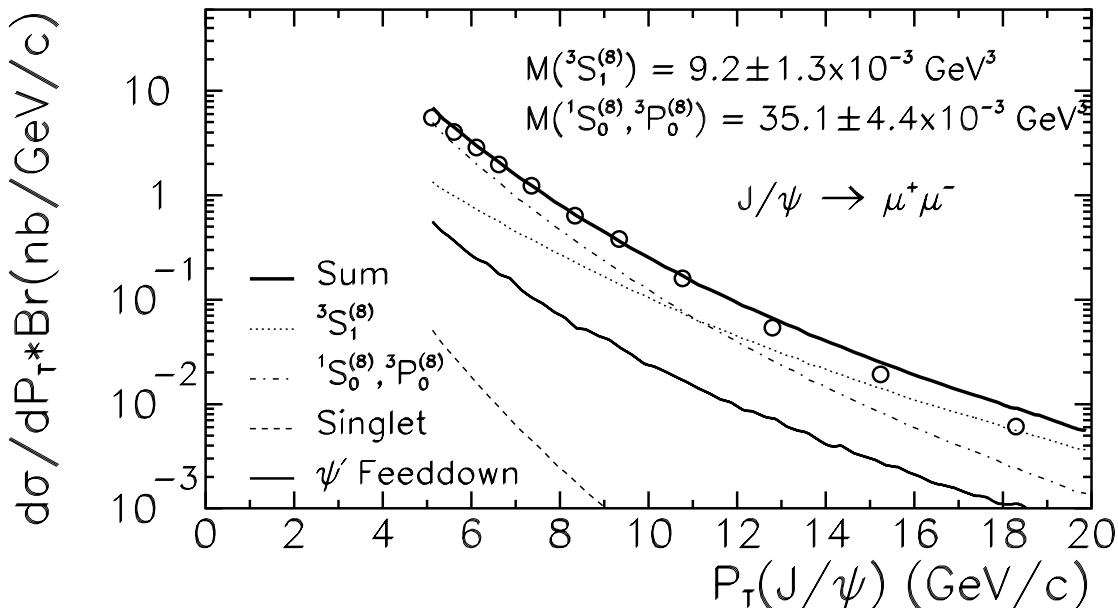

Figure 5-6: Results of fitting the color octet shapes to the J/ψ cross section. The B and χ_c contributions have been removed. The expectation is that the $^3S_1$ and $(^1S_0, ^3P_0)$ should be the same order of magnitude. The points are plotted at the P_T where the fitted function has its average value.

tion, there are three diagrams which need to be considered. Each of them introduces an unknown matrix element, which is a free parameter of the theory. Two of these components, associated with the matrix elements $\langle 0|\mathcal{O}_\psi^{(8)}(^3P_J)|0\rangle$ and $\langle 0|\mathcal{O}_\psi^{(8)}(^1S_0)|0\rangle$, have similar shapes in the kinematic region of interest. These two matrix elements are combined into one term, referred to by $(^1S_0, ^3P_0)$. The other contribution is associated with the $\langle 0|\mathcal{O}_\psi^{(8)}(^3S_1)|0\rangle$ matrix element, denoted by $^3S_1$. The $^3S_1$ is the result of fragmentation production, and will dominate the cross section at high P_T.

This leaves us with a prediction involving two free parameters for J/ψ direct production, and two parameters for $\psi(2S)$ production. The direct J/ψ cross section as calculated above does not correspond directly to the predictions of the Color Octet Model, but also includes feeddown contributions from $\psi(2S) \rightarrow J/\psi$X. The $\psi(2S) \rightarrow J/\psi$X feeddown contribution is accounted for by using a Monte Carlo to

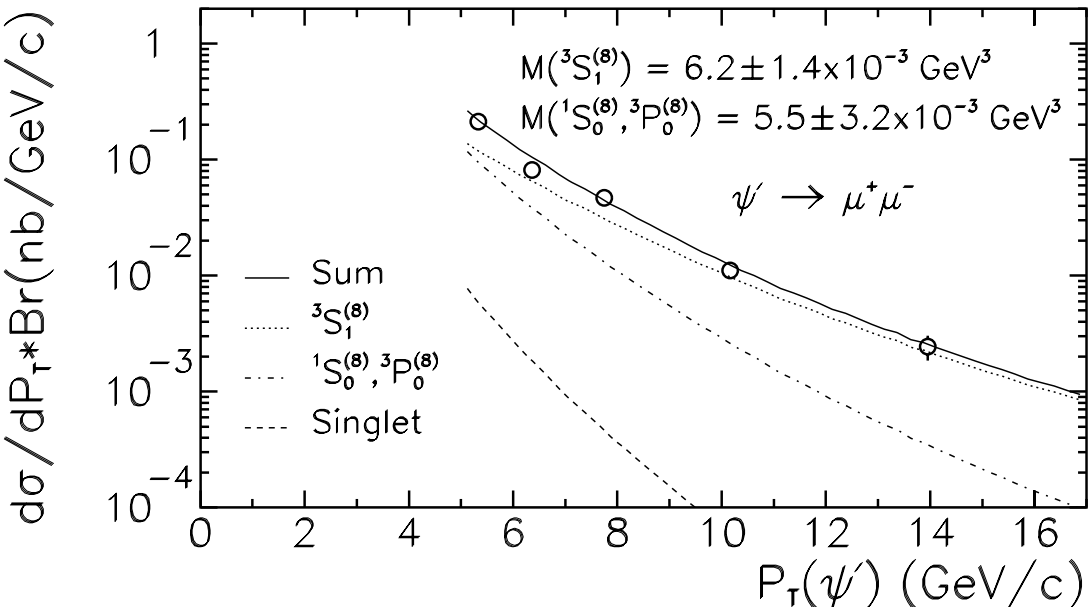

Figure 5-7: Results of fitting the color octet shapes to the $\psi(2S)$ cross section. The B contribution has been removed. The expectation is that the $^3S_1$ and ($^1S_0$,$^3P_0$) should be the same order of magnitude. The points are plotted at the P_T where the fitted function has its average value.

determine the shape of the feeddown. Monte Carlo $\psi(2S)$ events are generated with a flat P_T distribution, and decayed to $J/\psi\pi^+\pi^-$. For each production mechanism, we calculate the P_T distribution of the events with $|\eta(J/\psi)| < 0.6$, and weight these events by the $\psi(2S)$ cross section with the matrix element set to one. After normalizing for the number of events, the $\psi(2S)$ feeddown contribution to the J/ψ cross section is given by multiplying these distributions by the $\psi(2S)$ matrix element.

The simplest method to determine the matrix elements is to fit the J/ψ and $\psi(2S)$ independently, normalizing the $\psi(2S)$ feeddown into the J/ψ by the result of the $\psi(2S)$ fit. The global systematic uncertainties will just affect the value of the matrix elements. However, the P_T-dependent uncertainties will also affect the shape of the cross section, and change the ratio of the two components that best fits the data.

To allow for this, variations of at most one sigma are allowed on the trigger efficiency, the normalization of the χ_c fraction parameterization and the decay constant of the χ_c fraction parameterizations. The ψ polarization is allowed to take any value between -1 and $+1$, although it is assumed to be the same at for all values of P_T. The normalization of the $\psi(2S)$ feeddown into the J/ψ is also allowed to vary by the uncertainty on the branching ratios. In the J/ψ fit, the ratio of the $^3\mathrm{S}_1$ to $(^1\mathrm{S}_0,^3\mathrm{P}_0)$ matrix elements is about 1:3, in agreement with the prediction that the two parameters are the same order of magnitude. There are $\approx 20\%$ deviations at high P_T. For the $\psi(2S)$, the $^3\mathrm{S}_1$ contribution dominates the fit. While the $(^1\mathrm{S}_0,^3\mathrm{P}_0)$ matrix element has a large error, it is the same order of magnitude as the $^3\mathrm{S}_1$ matrix element. The fits are shown in Figure 5-6 and Figure 5-7, and the results are summarized in Table 5.3.

A more complex approach is to simultaneously fit the J/ψ and $\psi(2S)$ curves. This exploits the fact that there are correlations between the two measurements, which are lost if the two measurements are fitted separately. For instance, if the measured trigger efficiency is lower than the actual efficiency, it will be lower for both measurements by the same amount.

	$\langle 0\|\mathcal{O}_\psi^{(8)}(^3\mathrm{S}_1)\|0\rangle$ (GeV^3)	$\langle 0\|\mathcal{O}_\psi^{(8)}(^1\mathrm{S}_0,^3\mathrm{P}_0)\|0\rangle$ (GeV^3)
J/ψ	$9.2 \pm 1.3\times10^{-3}$	$35.1 \pm 4.4\times10^{-3}$
$\psi(2S)$	$6.2 \pm 1.4\times10^{-3}$	$5.5 \pm 3.1\times10^{-3}$
COM	$m_c^3 v_c^7 \sim 10\times10^{-3}$	$m_c^3 v_c^7 \sim 10\times10^{-3}$

Table 5.3: Fitted color octet matrix elements, using separate fits. The COM values are order-of-magnitude estimates based on scaling laws.

$P_T(J/\psi)$(GeV/c)	$\frac{d\sigma}{dP_T} \cdot \mathcal{B}$ (nb/GeV/c)
5-5.5	$7.94^{+1.34}_{-1.39}$
5.5-6	$5.86^{+0.95}_{-1.00}$
6-6.5	$4.07^{+0.63}_{-0.67}$
6.5-7	$2.79^{+0.41}_{-0.45}$
7-8	$1.73^{+0.24}_{-0.27}$
8-9	$0.890^{+0.12}_{-0.13}$
9-10	$0.523^{+0.064}_{-0.074}$
10-12	$0.217^{+0.025}_{-0.030}$
12-14	$0.0724^{+0.0083}_{-0.0098}$
14-17	$0.0253^{+0.0029}_{-0.0034}$
17-20	$0.0078^{+0.0012}_{-0.0013}$

Table 5.4: The differential J/ψ cross section from prompt production, as a function of P_T, for $|\eta(\psi)| < 0.6$. The contribution from χ_c feeddown is included, unlike the plots. The errors are the statistical and systematic errors added in quadrature.

$P_T(J/\psi)$(GeV/c)	$\frac{d\sigma}{dP_T} \cdot \mathcal{B}$ (nb/GeV/c)
5-5.5	$5.52 \pm ^{+1.09}_{-1.12}$
5.5-6	$4.04 \pm ^{+0.77}_{-0.80}$
6-6.5	$2.86 \pm ^{+0.52}_{-0.55}$
6.5-7	$1.97 \pm ^{+0.35}_{-0.37}$
7-8	$1.23 \pm ^{+0.21}_{-0.22}$
8-9	$0.640 \pm ^{+0.10}_{-0.11}$
9-10	$0.380 \pm ^{+0.057}_{-0.064}$
10-12	$0.159 \pm ^{+0.023}_{-0.026}$
12-14	$0.0542 \pm ^{+0.0076}_{-0.0085}$
14-17	$0.0193 \pm ^{+0.0027}_{-0.0030}$
17-20	$0.0061 \pm ^{+0.0010}_{-0.0011}$

Table 5.5: The differential J/ψ cross section from direct production, as a function of P_T, for $\eta(\psi)| < 0.6$. The contribution from χ_c feeddown has been removed. The errors are the statistical and systematic errors added in quadrature.

$P_T(\psi(2S))$(GeV/c)	$\frac{d\sigma}{dP_T} \cdot \mathcal{B}$ (nb/GeV/c)
5-6	0.21 ± 0.04
6-7	$0.081^{+0.017}_{-0.018}$
7-9	$0.047^{+0.008}_{-0.009}$
9-12	0.011 ± 0.002
12-17	$0.0024^{+0.0006}_{-0.0007}$

Table 5.6: The differential $\psi(2S)$ cross sections from prompt production as a function of P_T, for $|\eta(\psi)| < 0.6$. The errors are the statistical and systematic errors added in quadrature.

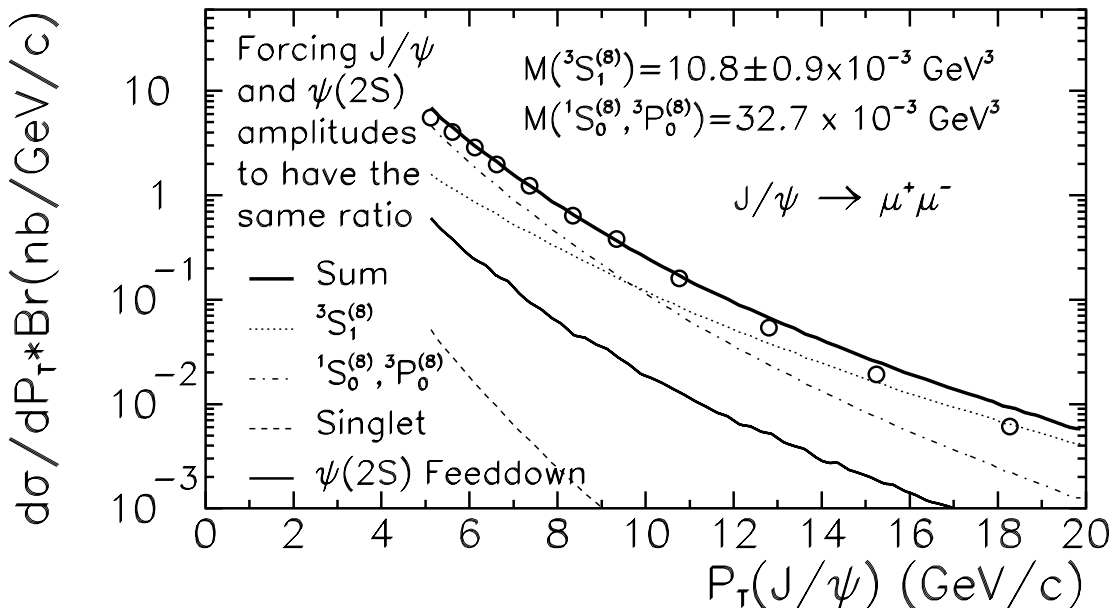

Figure 5-8: The J/ψ result from the simultaneous fit of the color octet to the J/ψ and $\psi(2S)$ cross sections. The B and χ_c contributions have been removed. The ratio of the $^3S_1$ and $(^1S_0, ^3P_0)$ amplitude has been required to be the same in the J/ψ and the $\psi(2S)$. P_T dependent uncertainties in the cross section have been included in the fit. The points are plotted at the P_T where the fitted function has its average value.

Since the theory predicts that the $^3S_1$ and $(^1S_0, ^3P_0)$ amplitudes should be similar for the J/ψ and $\psi(2S)$, we impose the additional constraint that the ratio of the two amplitudes be the same for the J/ψ and the $\psi(2S)$. Again, the ratio of the amplitudes is 1:3. The results are shown in Figure 5-8 and Figure 5-9 and are summarized in Table 5.7.

The COM is able to resolve the order of magnitude discrepancy of the CDF $\psi(2S)$ anomaly. However, this is a trivial statement, as the theory is normalized by fitting the data. A more stringent test is whether the COM describes the shape of the P_T spectrum. Here it does not do as well, predicting larger rates at both low and high P_T than are observed in the J/ψ data. Furthermore, while the matrix elements are supposed to be the same regardless of the experimental conditions which measure

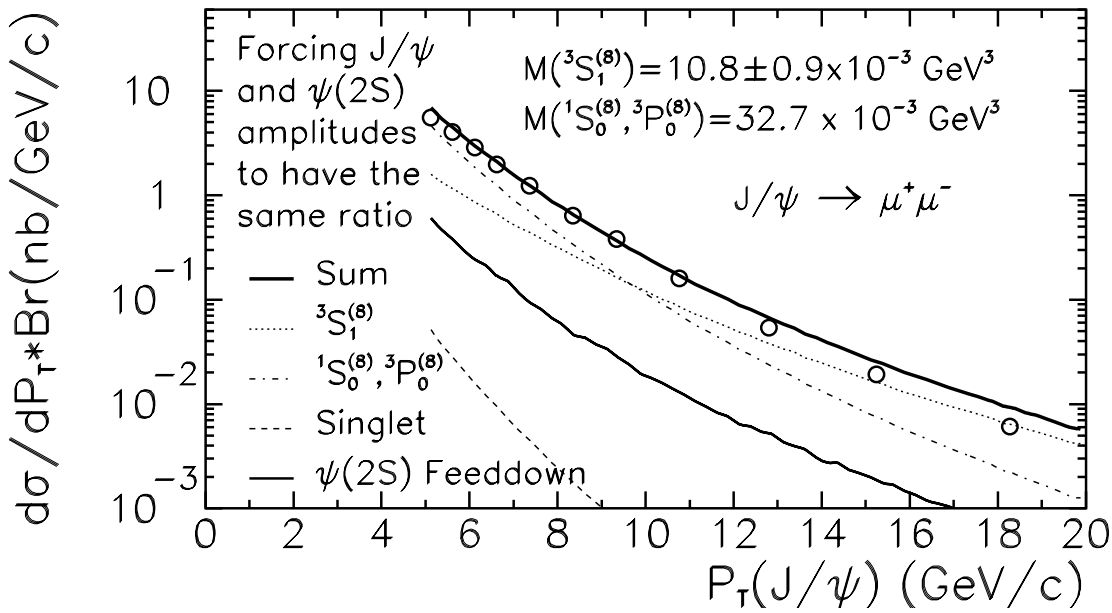

Figure 5-9: The $\psi(2S)$ result from the simultaneous fit of the color octet to the J/ψ and $\psi(2S)$ cross sections. The B contribution has been removed. The ratio of the $^3S_1$ and $(^1S_0, ^3P_0)$ amplitude has been required to be the same in the J/ψ and the $\psi(2S)$. P_T dependent uncertainties in the cross section have been included in the fit. The points are plotted at the P_T where the fitted function has its average value.

them, when fixed target experiments measure the same matrix elements, the values found are typically about a factor of three smaller. Additionally, when the matrix elements measured using CDF data are used to predict J/ψ photoproduction,[60], measurements made at HERA[61] are better described by the CSM than the COM at large z, the only regime where there are substantial differences between the COM and the CSM model predictions.

However, the current calculation is only a leading order calculation. Not only that, the uncertainties in the theory due to changing the renormalization scale, μ, or the charm quark mass, m_c, are ignored. It is not unreasonable to hope that these effects will allow the model to come into better agreement with the data. Failing that, further refinements to the theory, such as an improved fragmentation function

	$\langle 0\|\mathcal{O}_\psi^{(8)}(^3\mathrm{S}_1)\|0\rangle$ (GeV^3)	$\langle 0\|\mathcal{O}_\psi^{(8)}(^1\mathrm{S}_0,^3\mathrm{P}_0)\|0\rangle$ (GeV^3)
J/ψ	$10.8 \pm 0.9\times10^{-3}$	$32.7 \pm 2.2\times10^{-3}$
$\psi(2S)$	$3.6 \pm 0.1\times10^{-3}$	$10.8 \pm 1.0\times10^{-3}$
COM	$m_c^3 v_c^7 \sim 10\times10^{-3}$	$m_c^3 v_c^7 \sim 10\times10^{-3}$

Table 5.7: Fitted color octet matrix elements, fitting both distributions simultaneously. The ratio of the $(^1\mathrm{S}_0,^3\mathrm{P}_0)$ and $^3\mathrm{S}_1$ matrix elements is required to be the same for the J/ψ and the $\psi(2S)$. The COM values are order-of-magnitude estimates based on scaling laws.

or consideration of the intrinsic transverse momentum of the partons[62], are also possible.

5.4 Cross Section Ratios

The ratio of the J/ψ and $\psi(2S)$ cross sections is interesting for several reasons. First, it provides an internal cross check on the analysis. Additionally, many of the systematic uncertainties cancel. Furthermore, while the theory does not describe the data very well, large changes in the predicted shapes are correlated between the two states, and result in small changes in the ratio. In fact, in the case of B production, the theoretical uncertainty is dominated by the uncertainty in the branching ratios. At the end of this section, we will be able to extract an improved measurement of ratio of the product branching ratio

$$\frac{\mathcal{B}(\mathrm{B}\to\psi(2S)\mathrm{X})\cdot\mathcal{B}(\psi(2S)\to\mu^+\mu^-)}{\mathcal{B}(\mathrm{B}\to J/\psi\mathrm{X})\cdot\mathcal{B}(J/\psi\to\mu^+\mu^-)} \tag{5.29}$$

Each of the systematic uncertainties must be reconsidered, to determine to what extent the systematic uncertainties are correlated between the two measurements. The systematic uncertainty in the luminosity comes from the uncertainty in the total $\mathrm{p\overline{p}}$ cross section. In the ratio of cross sections, this cancels completely. The track reconstruction efficiency is the same for both the J/ψ and the $\psi(2S)$, so there is

Source	Uncertainty
Cross section	3.2%
B fraction	0.9%
B$\rightarrow\psi$ model	2%
μ, ϵ_P and m_b	2%
Total	4%

Table 5.8: Theoretical systematic uncertainties in the B cross section ratio measurements. All uncertainties are independent of P_T.

no uncertainty in the ratio from this source. Likewise, the muon reconstruction, event selection and the Level 3 trigger efficiencies cancel. The Level 1 and Level 2 trigger efficiencies depend on the P_T of the muons. The spectrum of the muons is slightly different for the J/ψ and the $\psi(2S)$, due to the $\sim$ 20% difference in the masses. As a result, there is a slight uncertainty from the efficiencies of these triggers, 0.2% for each trigger. The statistical uncertainties in the acceptance calculations are completely uncorrelated, and yield a 2% uncertainty. The effect of the ψ polarization is more difficult to calculate. In the absence of χ_c production, the J/ψ and the $\psi(2S)$ should have similar polarizations, as the same diagrams contribute to the production of each. In that case, there should be a near total cancelation of the uncertainties from the acceptances for the ratio. In reality, about one third of the J/ψ are produced from χ_c decays[63]. The polarization of these J/ψ could be markedly different from the polarization of the directly produced J/ψ. Therefore, we assign half the uncertainty on the absolute cross section to the ratio of the cross sections. The systematic uncertainties are summarized in Table 5.8.

Figure 5-10 shows the ratio of the cross sections for B production, and for direct production. The ratio from B production rises with P_T, which is predicted by the theory as a result of the kinematics of the B decay. The direct cross section ratio is approximately flat. The χ_c feeddown has been removed from the J/ψ cross section to make the ratio.

As the uncertainty in the branching ratios is the dominant uncertainty in the

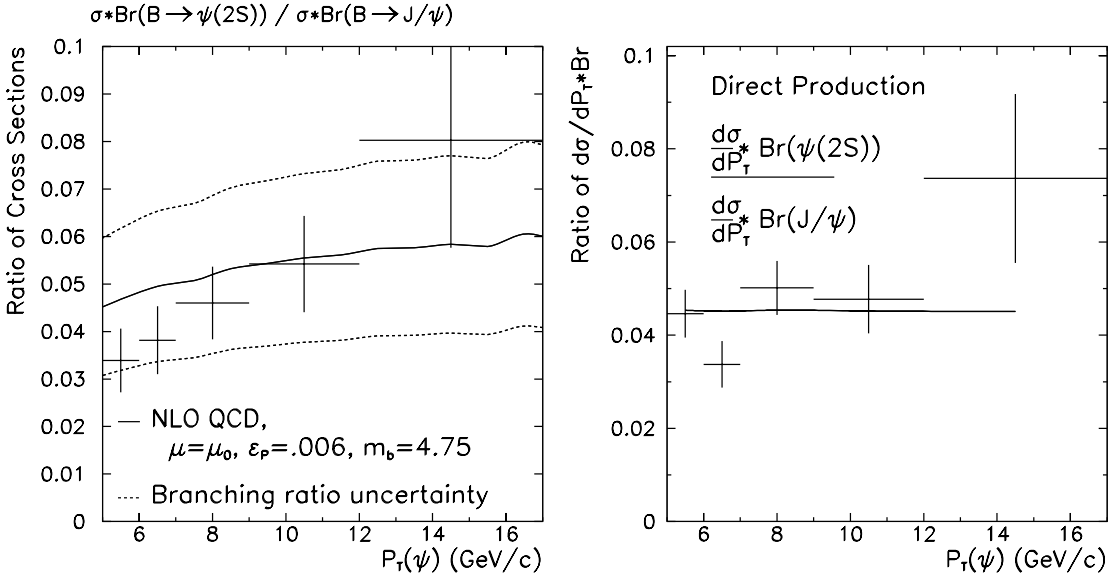

Figure 5-10: Ratio of cross sections, $\frac{d\sigma}{dP_T} \cdot \mathcal{B}(\psi(2S))/\frac{d\sigma}{dP_T} \cdot \mathcal{B}(J/\psi)$ for production from B decays (left) and direct production(right). For B production, the solid line is the central prediction and the dashed lines indicate the error on the branching ratios. For direct production, the solid line is the ratio of the fit results. The χ_c feeddown has been removed from the direct J/ψ cross section.

B ratio, an improved measurement of the ratio of branching ratios is possible. In Figure 5-11, the data has been divided by the theory, and fit to a constant. By multiplying this number by the ratio of branching ratios which are input to the theory, we are able to extract the ratio of branching ratios,

$$\frac{\mathcal{B}(\mathrm{B}\to\psi(2S)\mathrm{X}) \cdot \mathcal{B}(\psi(2S)\to\mu^+\mu^-)}{\mathcal{B}(\mathrm{B}\to J/\psi\mathrm{X}) \cdot \mathcal{B}(J/\psi\to\mu^+\mu^-)} = 0.033 \pm 0.003 \text{ (stat)} \pm 0.002 \text{ (sys)} \tag{5.30}$$

This is in agreement with the previous measurement (using the branching ratios listed on page 129)

$$\frac{\mathcal{B}(\mathrm{B}\to\psi(2S)\mathrm{X}) \cdot \mathcal{B}(\psi(2S)\to\mu^+\mu^-)}{\mathcal{B}(\mathrm{B}\to J/\psi\mathrm{X}) \cdot \mathcal{B}(J/\psi\to\mu^+\mu^-)} = 0.039 \pm 0.011 \tag{5.31}$$

where all the errors have been combined in quadrature. The error on ratio the branching ratios is a factor of 3 smaller than the previous measurement.

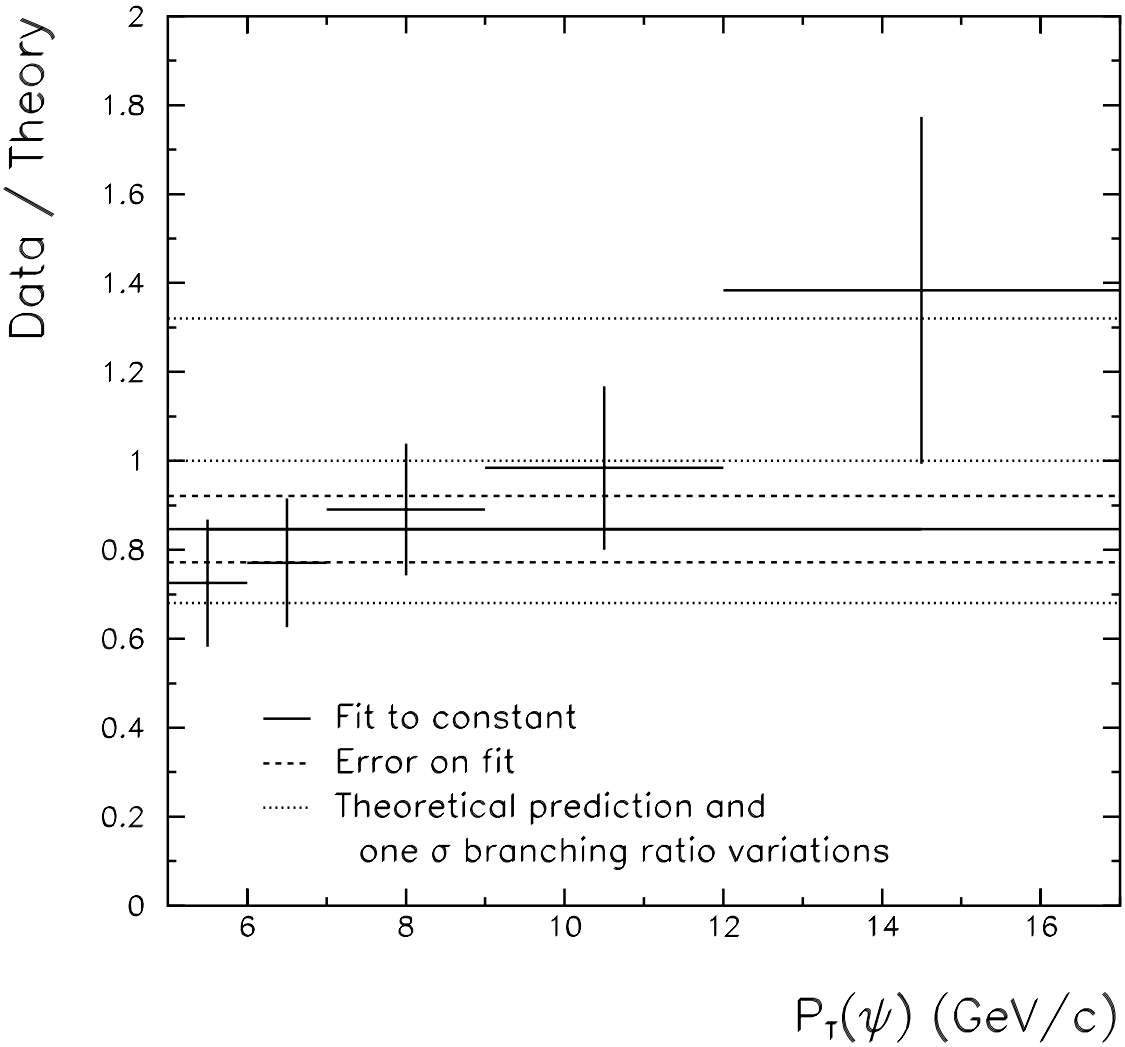

Figure 5-11: Ratio of cross sections from B production, divided by theory. The points are data, and the errors are statistical only. The solid line is a fit to a constant. The dashed lines are one σ variations on the fit. The dotted lines are correspond to the theoretical predictions, and the the one sigma limit based only on the branching ratios.

Using the measured J/ψ branching ratios, the product $\psi(2S)$ branching ratios can be extracted:

$$\mathcal{B}(\mathrm{B}\to\psi(2S)\mathrm{X})\cdot\mathcal{B}(\psi(2S)\to\mu^+\mu^-) = \\ (2.2\pm0.2(\mathrm{stat})\pm0.1(\mathrm{sys})\pm0.2(\mathcal{B}))\times10^{-5} \tag{5.32}$$

where the third error is from the uncertainty in the J/ψ branching ratios. This is in agreement with the previous measurement

$$\mathcal{B}(\mathrm{B}\to\psi(2S)\mathrm{X})\cdot\mathcal{B}(\psi(2S)\to\mu^+\mu^-) = (2.6\pm0.7)\times10^{-5} \tag{5.33}$$

where all the errors have been added in quadrature.

Chapter 6

Conclusions And Outlook

6.1 Summary of Results

We have measured the inclusive ψ cross section in $p\overline{p}$ collisions at $\sqrt{s} = 1.8$ TeV using the decay mode $\psi \rightarrow \mu^+\mu^-$. The integrated cross sections are found to be

$$\sigma(J/\psi) \cdot \mathcal{B}(J/\psi \rightarrow \mu^+\mu^-) = 17.4 \pm 0.1(\text{stat})^{+2.6}_{-2.8}(\text{sys}) \text{ nb} \tag{6.1}$$

$$\sigma(\psi(2S)) \cdot \mathcal{B}(\psi(2S) \rightarrow \mu^+\mu^-) = 0.57 \pm 0.04(\text{stat})^{+0.08}_{-0.09}(\text{sys}) \text{ nb} \tag{6.2}$$

where

$$\sigma(\psi) = \sigma(p\overline{p} \rightarrow \psi X, P_T(\psi) > 5 \text{ GeV/c}, |\eta(\psi)| < 0.6) \tag{6.3}$$

This is the first measurement of the ψ cross section at a hadron collider with the ability to clearly distinguish ψ production through an intermediate B state from prompt ψ production. This is done by accurately measuring the location of the ψ decay vertex, instead of using model-dependent methods such as examining P_T or isolation distributions. The integrated ψ cross sections from B production are found to be

$$\sigma(J/\psi, \text{B}) \cdot \mathcal{B}(J/\psi \rightarrow \mu^+\mu^-) = 3.23 \pm 0.05(\text{stat})^{+0.28}_{-0.30}(\text{sys}) \text{ nb} \tag{6.4}$$

$$\sigma(\psi(2S), \text{B}) \cdot \mathcal{B}(\psi(2S) \rightarrow \mu^+\mu^-) = 0.13 \pm 0.01(\text{stat}) \pm 0.01(\text{sys}) \text{ nb} \tag{6.5}$$

	$\langle 0\|\mathcal{O}_\psi^{(8)}(^3\mathrm{S}_1)\|0\rangle$ (GeV^3)	$\langle 0\|\mathcal{O}_\psi^{(8)}(^1\mathrm{S}_0,^3\mathrm{P}_0)\|0\rangle$ (GeV^3)
J/ψ	$9.2 \pm 1.3\times10^{-3}$	$35.1 \pm 4.4\times10^{-3}$
$\psi(2S)$	$6.2 \pm 1.4\times10^{-3}$	$5.5 \pm 3.1\times10^{-3}$
COM	$m_c^3 v_c^7 \sim 10\times10^{-3}$	$m_c^3 v_c^7 \sim 10\times10^{-3}$

Table 6.1: Fitted color octet matrix elements, using separate fits. The COM values are order-of-magnitude estimates based on scaling laws.

These are factors of 2-4 (3-4) higher than the central theoretical predictions for J/ψ ($\psi(2S)$) production.

The direct ψ cross sections are also extracted by removing the B and (for the J/ψ) the χ_c components. The integrated ψ cross sections from prompt production (including χ_c and $\psi(2S)$ feeddown into the J/ψ) and direct production (excluding the χ_c feeddown into the J/ψ) are found to be

$$\sigma(J/\psi, \mathrm{prompt}) \cdot \mathcal{B}(J/\psi \to \mu^+\mu^-) = 14.1 \pm 0.1(\mathrm{stat})^{+2.2}_{-2.3}(\mathrm{sys})\ \mathrm{nb} \tag{6.6}$$

$$\sigma(J/\psi, \mathrm{direct}) \cdot \mathcal{B}(J/\psi \to \mu^+\mu^-) = 9.95 \pm 0.08(\mathrm{stat})^{+1.8}_{-1.9}(\mathrm{sys})\ \mathrm{nb} \tag{6.7}$$

$$\sigma(\psi(2S), \mathrm{direct}) \cdot \mathcal{B}(\psi(2S) \to \mu^+\mu^-) = 0.43 \pm 0.03(\mathrm{stat})^{+0.06}_{-0.07}(\mathrm{sys})\ \mathrm{nb} \tag{6.8}$$

These exceed the predictions of the Color Singlet Model (CSM) by factors of 50-100, positively ruling out the CSM as the dominant explanation of direct charmonium production. The *shape* of the direct component can be described by the Color Octet Model (COM), with a discrepancy of only about 20% between the data and the central value of the theory at large transverse momentum. After the data is fit to determine the COM matrix elements, the values, given in Table 6.1 and Table 6.2, agree with the order-of-magnitude predictions of the COM.

Additionally, the ratio of the $\psi(2S)$ and J/ψ cross sections has been measured for both B production and direct production. The ratio of the direct cross sections is flat within the uncertainties on the data, indicating that the shape of the cross section does not have a large dependence on the mass of the charmonium state. The ratio of

	$\langle 0\|\mathcal{O}_\psi^{(8)}(^3\mathrm{S}_1)\|0\rangle$ (GeV^3)	$\langle 0\|\mathcal{O}_\psi^{(8)}(^1\mathrm{S}_0,^3\mathrm{P}_0)\|0\rangle$ (GeV^3)
J/ψ	$10.8 \pm 0.9\times10^{-3}$	$32.7 \pm 2.2\times10^{-3}$
$\psi(2S)$	$3.6 \pm 0.1\times10^{-3}$	$10.8 \pm 1.0\times10^{-3}$
COM	$m_c^3 v_c^7 \sim 10\times10^{-3}$	$m_c^3 v_c^7 \sim 10\times10^{-3}$

Table 6.2: Fitted color octet matrix elements, fitting both distributions simultaneously. The ratio of the ($^1\mathrm{S}_0,^3\mathrm{P}_0$) and $^3\mathrm{S}_1$ matrix elements is required to be the same for the J/ψ and the $\psi(2S)$. The COM values are order-of-magnitude estimates based on scaling laws.

the $\psi(2S)$ and J/ψ cross sections from the decay of B hadrons is expected to rise with P_T, due to kinematical effects resulting from the mass difference. This is observed in the data, and while the data rises faster than the theory predicts, the difference is not statistically significant. By fitting the data to the shape predicted by the theory, an improved measurement of the ratio of branching ratios is obtained:

$$\frac{\mathcal{B}(\mathrm{B}\to\psi(2S)\mathrm{X})\cdot\mathcal{B}(\psi(2S)\to\mu^+\mu^-)}{\mathcal{B}(\mathrm{B}\to J/\psi\mathrm{X})\cdot\mathcal{B}(J/\psi\to\mu^+\mu^-)} = 0.033 \pm 0.003\ (\mathrm{stat}) \pm 0.002\ (\mathrm{sys}) \qquad (6.9)$$

which has an error that is a factor of 3 smaller than the previous measurement. This is a model dependent measurement, although the model dependence is slight, and it is included in the systematic uncertainty.

6.2 Future Prospects

Charmonium production remains an interesting and exciting field. While this thesis has provided insight into important questions, unresolved issues still exist. The B production measured in this thesis is substantially larger than predictions, as is also observed in other measurements at CDF[64]. This may indicate that there is still a large "K factor" due to higher order terms. The large variation in the theory when the renormalization scale is lowered also indicates that a higher-order calculation may be necessary.

There is also work to be done regarding prompt charmonium production. The COM appears to resolve the CDF $\psi(2S)$ anomaly, but this merely reflects that the COM only predicts the shape of the components, not an absolute rate. Although the matrix elements measured with the Tevatron data, fixed target results[65] and in photoproduction data[61] are currently in disagreement with each other and thus in conflict with the COM prediction that they are universal, there is concern that effects which are neglected in the current calculations may be important.[66, 67] These issues must be resolved before the COM can be accepted or excluded as an accurate model of charmonium production. In addition to establishing the uncertainties in the theory, a prediction about the hadronic activity near the charmonium would provide another method for experimentalists to test the COM. It is straightforward to measure the isolation of the charmonium, but the interpretation is difficult in the absence of a theoretical prediction. From an experimental perspective, measuring the charmonium polarization at CDF would provide a direct test of one of the COM predictions.[68] There is 110 pb^{-1} of additional data taken with the CDF detector which is currently being analyzed to determine the charmonium polarization.

The CDF detector is currently being upgraded for Run II, scheduled to begin in 1999. The upgrades are intended to allow CDF to collect at least 2 fb^{-1} of data, while triggering on dimuons at lower P_T and larger η.[69] CDF also intends to record events with two electrons using similar thresholds. The greatly increased statistics will allow precise measurements in both the J/ψ and the $\psi(2S)$ modes. The simple increase in statistics will help the $\psi(2S)$ measurements. For the J/ψ, the additional events will increase the precision of the measurements at large transverse momentum, as well as increasing the accessible P_T region, probing the region where only fragmentation production is important. A more precise measurement of the polarization will also be possible, especially at high P_T, where the COM prediction is driven by the fragmentation component. The polarization measurement will reduce the systematic uncertainty on the acceptance, which is currently one of the largest systematic uncertainties. Other systematic effects will also be reduced as the improved statistics

provide a better measurement of detector effects.

The D0 detector is also being upgraded. One upgrade is the installation of a solenoid around the tracking system, which will significantly improve the muon momentum resolution, allowing D0 to resolve the J/ψ and $\psi(2S)$ states. A silicon vertex detector will also be installed, allowing D0 to separate the prompt component from B production. These upgrades will enable D0 to provide important confirmation of results obtained at CDF.

The Large Hadron Collider (LHC) currently being built at CERN will have proton-proton collisions with a center-of-mass energy of 14 TeV. This will allow the study of charmonium production to be extended to even larger values of P_T. Some theoretical calculations will also be simplified, as the accessible regions will have ${P_T}^2 \gg M^2$, so that fragmentation contributions should dominate production cross sections. If the COM does describe prompt charmonium production, then the matrix elements measured at the Tevatron and fixed target experiments can be used to predict not only the shape, but also the absolute rate of charmonium production at the LHC. Additionally, the center-of-mass energy dependence of not only the COM, but of any charmonium production model will also be tested.

Charmonium production will remain an exciting field for many years. Clearly determining the source of prompt charmonium production will be a challenge for both theorists and experimentalists. The charmonium decay channel will remain important handle for studying B physics at low momentum in high energy colliders.

Appendix A

Statistical Methods

A.1 Fitting Methods

The scientific method is based on determining whether a hypothesis, possibly with undetermined parameters, is consistent with a set of data and the errors on that data. In the case where the hypothesis is not completely specified, the best values of the parameters and the error on those parameters also need to be determined.

A common situation is where several independent measurements, $X(\vec{\alpha})$, have been made with errors $\sigma(\vec{\alpha})$. $\vec{\alpha}$ denotes the different conditions under which the measurements are made. $\vec{\alpha}$ may be an index, indicating a particular measurement in a series of identical measurements. Alternatively, $\vec{\alpha}$ may specify the conditions, such as the mass and P_T, which define a set of orthogonal measurements. If the measurements have a Gaussian distribution about the true value, the χ^2 test is useful, defined by

$$\chi^2 = \sum_{\{\vec{\alpha}\}} \frac{(X(\vec{\alpha}) - H(\vec{\alpha}, \vec{\beta}))^2}{\sigma(\vec{\alpha})^2} \tag{A.1}$$

$\vec{\beta}$ represents the undetermined parameters , and $H(\vec{\alpha}, \vec{\beta})$ is the predicted result for the conditions defined by $\vec{\alpha}$. By minimizing the χ^2, the best value for the parameters can be found. This χ^2 can be converted into a probability, indicating the likelihood that an experiment would produce the observed data, assuming the hypothesis is

correct. The change in the χ^2 as the parameters are varied from their optimal values yields the error on the parameters.

The χ^2 test is simple to use, but, like any method, it can give incorrect results when applied inappropriately. In particular, the derivation of the χ^2 test assumes that the results of repeated measurements form a Gaussian centered at the correct value. One common situation where this fails is in Poisson distributions. While it is true that when the number of expected events, N, is large, the errors are approximately Gaussian with

$$\sigma(N) = \sqrt{N} \tag{A.2}$$

this formula is not accurate for small values of N, and using the χ^2 method will give incorrect results if it is applied in these circumstances. This can be seen in Figure A-1, where the χ^2 fit significantly overestimates the number of events and the width of the distribution.

An improved technique is the maximum log-likelihood method.[70] In this case, the hypothesis is used to generate a probability density function for each data point, $P(X(\vec{\alpha}), \sigma(\vec{\alpha}), \vec{\alpha}, \vec{\beta})$. The likelihood function is defined as

$$\mathcal{L} \equiv \prod_{\{\vec{\alpha}\}} P(X(\vec{\alpha}), \sigma(\vec{\alpha}), \vec{\alpha}, \vec{\beta}) \tag{A.3}$$

which is just the product of the probabilities of all the events. The configuration of the parameters which maximizes $\mathcal{L}$ is the "most likely" hypothesis. Returning to Figure A-1, the log-likelihood fit yields a significantly better estimate of both the number of events and the width of the distribution. For technical reasons, one does not maximize $\mathcal{L}$, but instead minimizes $-2\ln\mathcal{L}$. Note that in the case where the errors are Gaussian,

$$P(X(\vec{\alpha}), \sigma(\vec{\alpha}), \vec{\alpha}, \vec{\beta}) \propto \exp\left(-\frac{\left[X(\vec{\alpha}) - H(\vec{\alpha}, \vec{\beta})\right]^2}{2\sigma(\vec{\alpha})^2}\right) \tag{A.4}$$

and $-2\ln\mathcal{L}$ reduces to the χ^2 plus a constant.

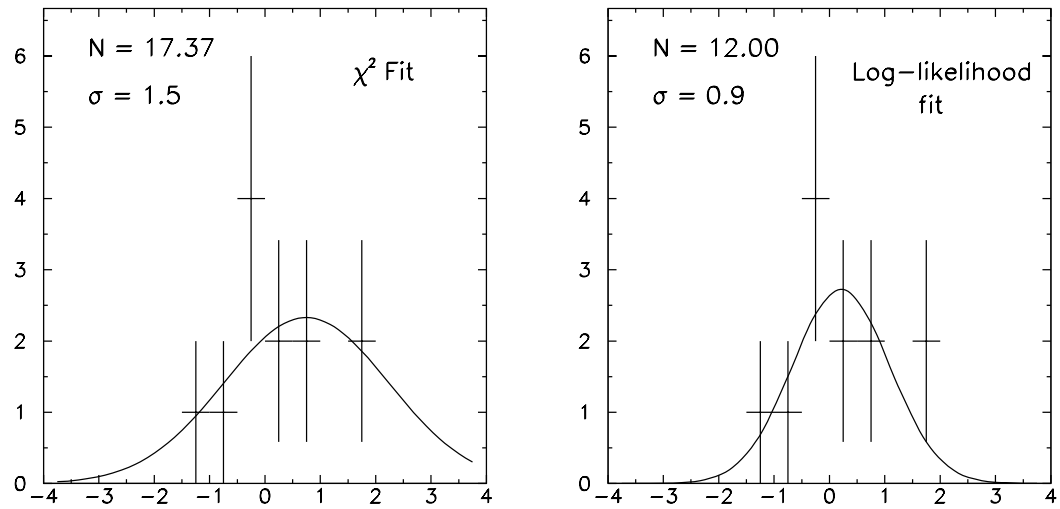

Figure A-1: Difference between χ^2 (left) and log-likelihood (right) fits. Twelve numbers are generated according to a normal distribution. The number of entries in each bin will have a Poisson distribution. The χ^2 fit fails to correctly determine the number of events ($N = 12$) or the width($\sigma = 1$). The log-likelihood fit is much more accurate.

Log-likelihood fits have an further advantage over χ^2 fits, in that it is simple to incorporate additional information by adding additional terms to the likelihood function. For instance, in the B fraction fit in Chapter 4, the number of events in each mass region is measured in the data, and a parameter in the fit. The likelihood function is multiplied by the Poisson probability for the fitted number to fluctuate to the observed number. This allows the level of the background in the signal region to vary, while still being constrained by the observed background levels. One disadvantage of log-likelihood fits is that there is no simple way to translate the value of the likelihood function into a confidence level, as is easily done with a χ^2 fit.

A.2 Toy Monte Carlos

To test the results of a log-likelihood fit, one typically constructs a "toy Monte Carlo." Assuming the hypothesis to be correct, a large number N of Monte Carlo data sets are generated according to the hypothesis. Each of these Monte Carlo data sets can then be fit in the same manner as the data. This produces a distribution of values for the likelihood function, measured on samples in which it is known that the hypothesis is correct. The confidence level of the fit is determined by counting the number of Monte Carlo data sets $N_<$ which have a likelihood smaller than the value obtained from the data. The confidence level of the fit is $N_</N$. If the hypothesis does describe the data, the confidence level should be a random number, uniformly distributed between 0 and 1.

These Monte Carlo samples can also be used to check the fitting method for biases. For any parameter, the mean of the values obtained from fitting the Monte Carlo samples should agree with the value used to generate the samples. If there is a difference, a confidence level can be constructed as above to determine if there is a significant possibility of a bias resulting from the fitting technique. Lastly, the toy Monte Carlo can check the errors determined by the fit. The pulls of the fitted values, defined by (Fitted - Generated)/Fitted Error, should have an RMS of one. The error from fitting the data should lie within the range of errors found while fitting the Monte Carlo samples.

Bibliography

[1] P.A.M. Dirac, *Proc. Roy. Soc*, **A117**, 610 (1928);
See also *The Principles of Quantum Mechanics*, Oxford University Press, 1947.

[2] P.A.M. Dirac, *Proc. Roy. Soc*, **133**, 60 (1931).

[3] S. Glashow, *Nucl. Phys.* **22**, 579 (1961).

[4] S. Weinberg, *Phys. Rev. Lett.* **19**, 1264 (1967).

[5] A. Salam, *Elementarty Particle Theory*, ed. N. Svartholm (Almquist and Wiksells, Stockholm, 1969), p. 367.

[6] Particle Data Group, *Phys. Rev. D* **50**, 1173 (1994).

[7] S. Glashow, J. Iliopoulos and L. Maiani, *Phys. Rev. D* **2**, 1285 (1970).

[8] J. Augustin *et al.*, *Phys. Rev. Lett.* **33**, 1404 (1974).

[9] J. Aubert *et al.*, *Phys. Rev. Lett.* **33**, 1406 (1974).

[10] G. Abrams, *Phys. Rev. Lett.* **33**, 1452 (1974).

[11] H. Satz, *Ann. Rev. Nucl. Part. Sci*, **35** 245 (1985) and references therein.

[12] T. Matsui and H. Satz, *Phys. Lett. B* **178**, 416 (1986). See M. Gyulassy, *Nucl. Phys.* **A418**, 59C (1985), J. Cleymans, R.V. Gavai and E. Suhonen, *Phys. Reports*, **130**, 218 (1986) and references therein for other proposed signatures.

[13] P.F. Smith, Ann. Rev. Nucl. and Part. Sci. **39**, 73 (1989);
L.Lyons, Phys. Reports **129**, 225 (1985);
M.Marinelli and G. Morpurgo, Phys. Reports **85**, 161 (1982) and references therein.

[14] C. Petersen *et al.*, *Phys. Rev. D* **27**, 105 (1983).

[15] J.Chrin, *Zeit. Phys.*, **C36**, 163 (1987).

[16] S. Bethke, *Zeit. Phys.*, **C29**, 175 (1985).

[17] W. Bartel, *et al.*, *Zeit. Phys.*, **C33**, 339 (1987).

[18] G. Zweig, CERN Report 8419/Th 412, 1964.

[19] R. Van Royen and V. Weisskopf, *Nuovo Cim* **50**, 617 (1967) and *Nuovo Cim* **51**, 583 (1968).

[20] C.-H. Chang, *Nucl. Phys.* **B172**, 425 (1980).

[21] R. Baier and R. Rückl, *Phys. Lett. B* **102**, 364 (1981);
R. Baier and R. Rückl, *Zeit. Phys.*, **C19**, 251 (1983).

[22] S.D. Ellis, *et al.*, *Phys. Rev. Lett.* **36**, 1263 (1976);
C.E. Carlson and R. Suaya, *Phys. Rev. D* **15**, 1416 (1977).

[23] G. Bodwin, E. Braaten and G. Lapage, *Phys. Rev. D* **46**, R1914 (1992);
G. Bodwin, E. Braaten and G. Lapage, *Phys. Rev. D* **51**, 1125 (1995).

[24] A good review of HQET is available in M. Neubert, *Phys. Reports*, **245**, 259 (1994) and references therein.

[25] E. Shuryak, *Phys. Lett. B* **93**, 134 (1980);
E. Shuryak, *Nucl. Phys.* **B198**, 83 (1982).

[26] N. Isgur and M. Wise, *Phys. Rev. Lett.* **66**, 1130 (1991);
N. Isgur and M. Wise, *Phys. Lett. B* **232**, 113 (1989);
N. Isgur and M. Wise, *Phys. Lett. B* **237**, 527 (1990).

[27] R. Balest *et al.*, *Phys. Rev. D* **52**, 2661 (1995).

[28] S. van der Meer, *Stochastic Damping of Betatron Oscillations in the ISR*, CERN/ISR-PO/72-31 (1994);
F. Sacherer, *Stochastic Cooling Theory*, CERN-ISR-TH/78-11 (1981).

[29] F.Abe *et al.*, CDF Collab., *Nucl. Inst. and Meth.*, Sect. A, **271**,387 (1988) and references therein.

[30] N. Amos, *et al.*, *Phys. Rev. Lett.* **68**, 2433 (1992).

[31] F. Abe *et al.*, *Phys. Rev. D* **50**, 5550 (1994).

[32] E710 Collaboration, N. Amos *et al.*, *Phys. Rev. B* **243**, 158 (1990).

[33] U.S. Depeartment of Energy report DOE/ER-0189 (1983).

[34] G. Drake *et al.*, *Nucl. Inst. and Meth.*, Sect. A, **269**,68 (1988).

[35] H. Brafman *et al.*, IEEE Trans. Nucl. Sci. NS-32, 336 (1985).

[36] Ph.D. Thesis, "Polarization in Vector-Vector Decay of B Mesons at CDF," Randal Milton Hans, Yale University, May 1996;
R. Hans and F. DeJongh, **CDF** Internal Note 1999 (1993).

[37] B. Denby and M. Contreras, **CDF** Internal Note 1324 (1990).

[38] *Punchthrough in Hadronic Shower Cascades, Muon Identification and Scaling Laws for Different Absorbers*, Arie Bodek, University of Rochester preprint, UR 911 (1985).

[39] F. DeJongh, **CDF** Internal Note 1984 (1993).

[40] H. Bethe, *Phys. Rev.* **89**, 1256 (1953).

[41] V.Highland, *Nucl. Inst. and Meth.*, **129**,497 (1975) and *Nucl. Inst. and Meth.*, **161**,171 (1979).

[42] G. Lynch and O. Dahl, *Nucl. Inst. and Meth.*, Sect. B, **58**,6 (1991).

[43] Y. K. Kim, **CDF** Internal Note 2664 (1994).

[44] J. Lewis and D. Vučinić, **CDF** Internal Note 3023 (1995)

[45] Coffman *et al.*, *Phys. Rev. D* **41**, 1410 (1992)

[46] G. Feldman and M. Perl, *Phys. Reports*, **33C**, 287 (1977).

[47] Much of the code used to perform the B fraction fit was written by Olivier Schneider for the exclusive B lifetime measurement.[71] The well-organized and clearly documented manner in which the code was written was a great aid in extending it to measure the B fraction in the ψ samples.

[48] F. Abe *et al.*, *Phys. Rev. Lett.* **71**, 3421 (1993).

[49] P. Sphicas, **CDF** Internal Note 2655 (1994). Not all of the available options are used or described in this thesis.

[50] P. Nason *et al.*,*Nucl. Phys.* **B327**, 49 (1988).

[51] A. Martin, R. Roberts and W. Stirling, *Phys. Rev. D* **50**, 6734 (1994);
A. Martin, R. Roberts and W. Stirling, RAL-92-021, DTP-92-16.

[52] E. Braaten, K. Cheung, and T.C. Yuan, *Phys. Rev. D* **48**, R5049 (1993).

[53] C. Chang and Y. Chen, *Phys. Rev. D* **49**, 3399 (1994).

[54] M. Mangano, Invited talk at the 9th Topical Workshop on Proton-Antiprotn Collider Physics, 18-22 October 1993, Tsukuba, Japan. IFUP-TH 60/93.

[55] C. Albajar *et al.*, *Phys. Lett. B* **256**, 112 (1991).

[56] F. Abe, *Phys. Rev. Lett.* **69**, 3704 (1992).

[57] E. Braaten and T. Yuan, *Phys. Rev. Lett.* **71**, 1673 (1993);
E. Braaten and T. Yuan, *Phys. Rev. D* **52**, 6627 (1995).

[58] M. Cacciari, M. Greco, M.L. Mangano and A. Petrelli, *Phys. Rev. B* **356**, 553 (1995).

[59] F. Abe *et al.*, *Phys. Rev. Lett.* **71**, 2537 (1993).

[60] M. Cacciari and M. Krämer, DESY preprint DESY 96-005 (1995), hep-ph/9611324.

[61] H1 Collaboration, DESY preprint DESY 96-037 (1996), hep-ph/9603005.

[62] M. A. Sanchis-Lozano and B. Cano-Coloma, Contribution to the 2nd Int. Conference on Hyperons, Charm and Beauty Hadrons (Montreal, Aug. 27-30, 1996), hep-ph/9611264. To be published in Nucl. Phys. **B** Proc. Suppl.

[63] F. Abe *et al.*, "Production of J/ψ from χ_c decays in $p\bar{p}$ Collisions at $\sqrt{s} = 1.8$ TeV", Fermilab Preprint FERMILAB-PUB-97/026-E, submitted to Phys. Rev. Letters.

[64] J. Olsen, Proceedings of the 1996 Meeting of the Division of Particles and Fields, American Physical Society, Minneapolis, MN, August 10-15, 1996 and references therein.

[65] Y. Lemoigne *et al.*, *Phys. Lett. B* **113**, 509 (1982);
D. M. Alde *et al.*, *Phys. Rev. Lett.* **66**, 2285 (1991);
J. G. Heinrich *et al.*, *Phys. Rev. D* **44**, 1909 (1991);
L. Antoniazzi *et al.*, *Phys. Rev. Lett.* **70**, 383 (1993);
C. Akerlof *et al.*, *Phys. Rev. D* **48**, 5067 (1993);
M. H. Schub *et al.*, *Phys. Rev. D* **52**, 1307 (1995);
T. Alexopoulos *et al.*, *Phys. Lett. B* **374**, 271 (1996);

[66] M. Beneke and I. Rothstein, *Phys. Rev. D* **54**, 2005 (1996) and references therein.

[67] W.-K. Tang, Invited talk presented at Workshop on the Future of High Sensitivitiy Charm Experiments: Charm2000, Fermilab, Batavia, Il., June 7-9, 1994, SLAC-PUB-95-6577, hep-ph/9408372.

[68] A. Leibovich, Cal. Tech. Preprint CALT-68-2082, hep-ph/9610381.

[69] "The CDF II Detector: Technical Design Report, The CDF II Collaboration," FERMILAB-Pub-96/390-E, October 1996.

[70] H. Cramér, *Mathematical Methods of Statistics*, Princeton University Press, New Jersey (1958).

[71] F. Abe *et al.*, *Phys. Rev. Lett.* **72**, 3456 (1994).